UNIVERSITY OF BIRMINGHAM

DEVELOPMENT OF A BIO-INSPIRED MEMS BASED TACTILE SENSOR ARRAY FOR AN ARTIFICIAL FINGER

By

Haseena Bashir Muhammad

A thesis submitted to
The University of Birmingham
For the degree of
Doctor of Philosophy

SCHOOL OF MECHANICAL ENGINEERING
THE UNIVERSITY OF BIRMINGHAM
DECEMBER 2011

Abstract

In this thesis, the design, fabrication and characterisation of a bio-inspired microelectromechanical systems (MEMS) based tactile sensor array is presented. A vast amount of research has been carried out in the area of tactile sensing and various transduction methods have been explored. However, currently no device exists with a performance comparable to that of the biological tactile sensors of the human fingertip in terms of robustness, sensitivity, spatial resolution and dynamic performance. The sensors developed in this work employ the principles of electrical capacitance and are fabricated from commercially available silicon-on-oxide wafers using simple process steps. Each sensor is formed from two plates of highly conductive silicon separated by an air-gap formed from sacrificial etching of the oxide layer. Deflection of the 2 μm thick upper plate of the sensor as a result of applied mechanical stimulus, causes a change in capacitance which is the output of the sensor. Within the array, the individual sensors are spaced 150 μm apart (centre-centre pitch of 570 μm) and therefore offer the potential for high spatial resolution. To protect the sensor array from mechanical shock and provide skin like compliance, the use of suitable packaging materials was explored. The use of poly dimethyl siloxane (PDMS) as a suitable skin-like material was demonstrated. Modification of the surface topography of the packaging layer to include 'fingerprint' like features was explored and its benefits highlighted. Sensor characterisation experiments revealed that the sensing device was sufficiently sensitive to allow the discrimination of different textures (with feature spacing down to 0.2 mm) through tests conducted using gratings varying in spatial periodicity and fabrics. Based on the results, the sensors can be used as an analogue of the slowly adapting tactile receptors (Merkel disks) for robotic finger applications.

I dedicate this thesis to my beloved late father Dr. Bashir Mohammed, whose hard work and dedication to lifelong learning has been a source of inspiration to me. His unwavering support and encouragement through the course of my studies has been invaluable.

Acknowledgments

This thesis would not have been possible without the incredible support and help I have received from a number of people. I would therefore like to express my deepest gratitude to the following people.

Firstly I wish to thank my supervisor Dr. Mike Ward for having given me the opportunity to be part of this very interesting project, for the guidance, financial and personal support throughout the course of my research. I would also like to thank Prof. David Hukins and Prof. Mike Adams for their advice and guidance. I wish to thank Dr. Carl Anthony who lent his kind support throughout the course of my work and specifically provided me with invaluable guidance with his knowledge and experience in microfabrication.

I wish to thank the numerous people of the ARTS Laboratory, SSSA, Italy for their assistance and contributions to the course of this work. Among those, I am specially grateful to Lucia Beccai for having given me the opportunity to collaborate and use the experimental testing facilities in the ARTS Lab. Further, I thank Carmine Recchiuto and Calogero Oddo for the development of the electronic interface and for their contribution to the device characterisation experiments and joint publications.

I would like to thank Satoshi Endo for his assistance with manufacturing gratings and James Bowen for his assistance with the use of the mechanical testing devices.

A big thank you to all the present and former colleagues from the MEMS group. I would particularly like to thank my wonderful office colleagues Sahand, Aydin, Ali Kubba, Rob and Ali Sadeghioon for the lively discussions, for making light of every situation and from whom I have learnt a great deal. I would also like to thank Ayda who made my time at work enjoyable.

I would like to thank Thomas Kiefer for his endless help with Latex, thesis corrections

and for always providing me lots of motivation. I would also like to thank Cristina for her kind help with the corrections of my thesis.

This acknowledgement would be incomplete without mentioning my heartfelt gratitude to my beautiful friends Shelan, Sandibell, Ladan, Ania, Deshne, Lynne and Kieren who have provided me with lots of support and love.

No words can convey my gratitude to my late father Dr. Bashir for his ever present support, encouragement and love. And to my mother and sisters Rehana, Zeena and Hannah for having encouraged me during the course of my studies and for their heartfelt support.

Haseena Muhammad

Birmingham

February 24, 2012

Publications

During the course of this project, the following Journal Papers and Conference Proceedings have been published:

Journal Papers

1. H. B. Muhammad, C. M. Oddo, L. Beccai, C. Recchiuto, C. J. Anthony, M. J. Adams, M. C. Carrozza, D. W. L. Hukins, and M. C. L. Ward, Development of a bioinspired MEMS based capacitive tactile sensor for a robotic finger, Sensors and Actuators A: Physical, 165 (2), 221-229 (2011)

2. H.B. Muhammad, C.T. Recchiuto, C.M. Oddo, L. Beccai, C. J. Anthony, M.J. Adams, M.C Carrozza, M.C. Ward, A capacitive tactile sensor array for surface texture discrimination, Microelectronic Engineering, (88), 1811-1813 (2011)

3. H.B. Muhammad, C.M. Oddo, L. Beccai, M.J. Adams, M.C Carrozza, D.W. Hukins, M.C. Ward, Development of a Biomimetic MEMS based Capacitive Tactile Sensor, Procedia Chemistry, Volume 1, Issue 1, Proceedings of the Eurosensors XXIII conference, September 2009, Pages 124-127

Conference Proceedings

1. H.B. Muhammad, C.T. Recchiuto, C.M. Oddo, L. Beccai, M.J. Adams, M.C Carrozza, M.C. Ward, A MEMS tactile sensor array for texture recognition, 36th International Conference on Micro and Nano Engineering (MNE) 2010, 19th - 22nd September 2010

2. H.B. Muhammad, Workshop: Bioinspired tactile sensing. Developing a biomimetic sensor based on nanoscale force transducers to mimic the resolution, sensitivity and

dynamics of spatial touch in the human finger, Eurohaptics 2010, Amsterdam, 8th - 10th July 2010

3. H.B. Muhammad, N.C. Hunt, R.M. Shelton, L.M. Grover, M.C.L Ward, C.M. Oddo, C.T. Recchiuto, L. Beccai, Incorporation of Novel MEMS Tactile Sensors into Tissue Engineered Skin, 4th International Conference on Bioinformatics and Biomedical Engineering (iCBBE) , 18-20 June 2010

4. H.B. Muhammad, C.M. Oddo, L. Beccai, M.J. Adams, M.C Carrozza, D.W. Hukins, M.C. Ward, Development of a Biomimetic MEMS based Capacitive Tactile Sensor, Eurosensors XXIII conference, September 2009

*"Human subtlety will never devise an invention more beautiful, more simple or more direct than does **nature** because in her inventions nothing is lacking, and nothing is superfluous"*

- Leonardo da Vinci

Contents

List of Figures

List of Tables

1

Introduction

Contents

Summary This chapter provides a brief introduction to tactile sensors and offers an overview of some of their major applications. The motivation for the work is given, followed by a presentation of the thesis structure.

1.1 Background and Literature

1.1.1 What are tactile sensors

Tactile sensors are devices or systems that measure a given property of an object or surface through physical contact with it [1]. This includes the detection and measurement of the spatial distribution of forces on a defined area and the subsequent interpretation of the spatial information. They can be used to provide information on parameters such as object shape, texture, temperature, moisture level, pain and other related physical properties [2].

1.1.2 Applications of tactile sensors

Tactile sensors have an extensive range of applications across a number of domains. In the following, some major applications are described.

Medical applications

- **Surgery** Tactile sensors can be used to provide surgeons conducting Minimal Invasive Surgery (MIS) with a "sense of feel" allowing remote assessment of tissue health and its safe manipulation. Reviews of tactile sensing technologies for MIS can be found in the works of Eltaib and Hewitt [3] and Puangmali et al.[4].

- **In-vivo pressure measurement** Tactile sensors can be incorporated at the tip of a catheter to allow in-vivo blood pressure measurement[5–7].

- **Diagnostic screening** By providing information on tissue properties such as elasticity, tactile sensors can be used for cancer screening [8].

- **Prosthetic and orthotic devices** Tactile sensors can be used to restore loss of tactile sensations for people with amputations or sensory neuropathies. Enabling tactile feedback in an artificial limb can greatly enhance the quality of life and provide improved prosthetic acceptance, use and level of control for amputees [9]. To this end, significant efforts are made to develop artificial hands that have all the features of a human hand [10, 11].

Industrial/manufacturing processes In industry, tactile sensors can be used to automate manufacturing processes such as assembly, machining, sorting and stacking [12].

Pharmaceutical Cosmetic and pharmaceutical industries employ tactile sensors to characterise the feel of different surfaces or substances in order to classify their attractiveness [13].

Robotics Tactile sensors are implemented in robots to allow task execution such as object identification, grasping, manipulation and to enable safe interaction in unstructured environments. While grasping objects, feedback from tactile sensors is necessary to optimise grasp forces so as to avoid unnecessary energy expenditure and prevent damage of delicate objects. Reviews of tactile sensors for robotic manipulation can be found in the works of Howe (1994), Tegin and Wikander (2005) and Dargahi and Najarian (2005) [14–16].

1.2 Motivation of this work

The work in this thesis has been carried out in the framework of an EU-funded project titled Nanobiotact (Nano-engineering biomimetic tactile sensors). The main aim of the project is

to develop a biomimetic tactile sensor for incorporation into an artificial finger.

Although there has been significant progress in the development of upper limb prostheses, currently there are no commercially available systems that provide a prosthetic user with the functional capability on par with that of the natural arm. The man-machine interface associated with the use of prosthetic devices is considered unnatural and is a factor that significantly impairs user's acceptance of a prosthetic device. In view of this, there has been a move towards anthropomorphic or human-like designs of devices [17, 18].

The sense of touch is vital in enabling individuals to carry out day to day tasks and to convey feelings and emotions. Inclusion of sensory feedback in upper limb prosthetic devices is hence a well recognised requirement and is known to significantly enhance user acceptance of the device and augment function [9]. Studies have shown that users of myoelectric prostheses (prosthetic devices controlled by signals generated by voluntarily contracting muscles in the residual limb) showed improvements in their regulation of grasping forces when sensory feedback in the form of vibration or electrical stimulus was applied directly to the skin of the residual limb [19–21].

Recent approaches in the implementation of limb prosthetics are hybrid systems that interface the human nervous system with electronic or robotic prostheses, allowing for a more natural intuitive control of the prosthetic devices. For instance, to replace the sensory function of the human hand, signals generated by tactile sensors embedded within a prosthetic hand can be converted into trains of electrical pulses, similar to those emitted by sensory receptors in the human hand. These signals can be then transmitted to intact peripheral nerves in the residual stump of an amputee by means of appropriate electrodes, thus providing the individual with tactile sensation (Fig. 1.1) [22, 23].

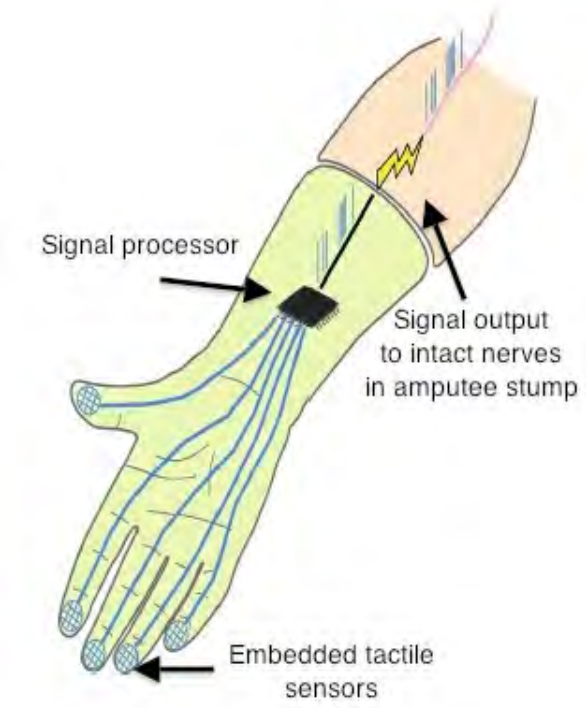

FIGURE 1.1: Diagram of a sensorised prosthetic hand. Here signals from embedded tactile sensors are converted to spike trains that are then transmitted to residual peripheral nerves [22]

Fig. 1.2 shows a schematic of a prosthetic device known as "The Cyberhand" which is being developed by a team led by Carrozza et al. [18]. The device aims to replicate the sensory and motor capabilities of the human hand. Biological signals are harnessed to control the device and sensory feedback is allowed by stimulating specific nerves with signals processed from embedded tactile sensors.

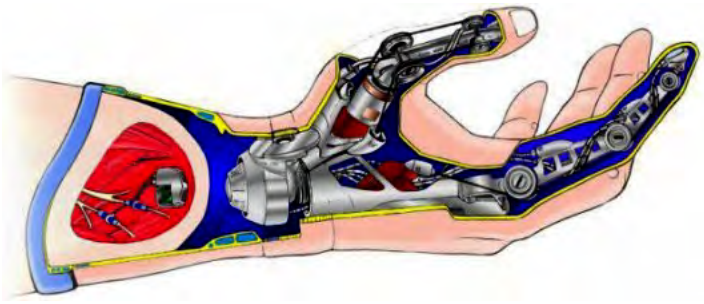

FIGURE 1.2: Schematic of the Cyberhand developed by Carrozza et al. [18] Signals from the central nervous system are used to control the device. Outputs from sensors in the device are used to stimulate intact nerve fibres for providing the user with tactile feedback

1.2.1 Objectives

Considerable scientific and technological efforts are being put forward to further the realms of prosthetic technology towards more natural devices that permit the perception of sensation. With this in view, the main focus of the work in this thesis is to develop tactile sensors that can be incorporated into an artificial finger of a prosthetic device or robotic hand.

The highly sophisticated and efficient system of tactile sensation, as allowed by the human hand which enables the perception and differentiation of a range of textures, serves as an inspiration for the development of such sensors. In order to implement a bio-inspired approach, at first an understanding of the operational characteristics of the human tactile sensors or mechanoreceptors is required. Using the human biological system of touch as a model, the aim of this work is to develop a sensing device that has sufficient force and spatial resolution to provide a surface discrimination capability similar to that of human fingers. As in the human fingertips, a high density of sensors within a small area is desirable to allow acquisition of a rich dataset of tactile information that can be extracted and extrapolated to provide information on spatial features of the surface in contact with the finger. Further, since the device is intended for incorporation into an artificial finger, a requirement is that it is compatible with a skin-like coating layer. In addition to protecting the sensors, this skin-like layer behaves as an information coding layer that transmits surface forces to the underlying sensors.

The application of Micro-Electro-Mechanical Systems (MEMS) technology in the design and development of such a device is explored in this thesis. This technology allows the fabrication of devices and systems with dimensions in the micrometer to millimeter range by adopting established integrated-circuit manufacturing techniques supplemented by its own

processes. Thus, due to its capability of miniaturisation it is possible to implement devices whose dimensions are in the order of magnitude of tactile sensors in the biological system. Such technology enables the incorporation of a high density of sensing structures within a given area and the potential for high attainable spatial resolution.

A key emphasis of the work in this thesis is to design the device using simple fabrication steps.

1.3 Thesis content and structure

This thesis is divided into five main chapters detailing the design and development of the MEMS based tactile sensor array.

In Chapter 2, the biological mechanisms of human tactile sensing are first introduced. The main types of tactile sensors found in the human fingertip and their roles are described. An introduction to artificial tactile sensing with a brief description of the most commonly employed transducer mechanisms is given. Following this the concept of bio-inspired tactile sensors is described with specific examples of work carried out in this area. Finally, the use of MEMS technology in the development of tactile sensors is discussed and a review of devices developed to date is given.

Chapter 3 describes the design concept of the MEMS tactile sensor which is based on the principles of electrical capacitance. Analytical and numerical (Finite Element Analysis) methods are used to study the diaphragm deflection and sensor output characteristics. The implementation of sensor arrays is presented. Finally, the design of the signal acquisition electronics is given.

In Chapter 4, the fabrication of the sensing device using batch fabrication techniques is

outlined.

Chapter 5 deals with the implementation of the fabricated sensor within a skin-like material. Candidate materials that can be used as artificial skin are explored.

In Chapter 6, the experimental characterisation of the fabricated sensors is described. Methods mimicking those used in the evaluation of human tactile sensors are implemented. The results are presented along with a discussion of device performance. Additionally comparisons are made between the performance of the fabricated device and biological tactile sensors.

Finally, a general conclusion is given in chapter 7, along with an outlook for future work.

2

Tactile sensing systems

Contents

Summary In this chapter, firstly an overview of the fundamental mechanisms for touch sensation in humans is given. The motivation for the development of artificial tactile systems that emulate biological systems of touch sensation is explored with references to research carried out to date in bio-inspired tactile sensor development. After a general introduction to microelectromechanical systems (MEMS) and their application in tactile sensing, an overview of the state of the art in MEMS based tactile sensors is finally given.

2.1 Tactile sensing in the human fingertip

Tactile sensing is an essential biological survival tool playing a significant role in the exploration and manipulation of objects in ones environment and enabling suitable responses or reactions to stimuli. For successful object manipulation and perception, accurate information on stimulus parameters such as its shape, its location of contact on skin and magnitude and direction of contact force is required [24]. An efficient and sophisticated tactile sensing system has evolved in humans allowing discrimination of subtle changes in texture and object recognition even in the absence of other sensing modalities such as vision. This is possible through the human somatosensory system; a system that includes a network of specialised sensory receptors embedded within the skin, peripheral nerve fibres for information propagation and a network of neurones within the central nervous system for information processing (Fig. 2.1) [25].

The main categories of sensory receptors mediating human tactile sensations are thermoreceptors (temperature sensors), nociceptors (pain sensors) and mechanoreceptors (sensors that respond to mechanical stimuli). Thus, touch takes many forms and manifests itself in the detection of shape, texture, friction, force, pain, temperature and many other physical related properties. The focus in this thesis is on mechanical aspects of touch. Therefore, the following sections will focus on the neurophysiology of touch and specifically the functioning of the mechanoreceptors.

2.1.1 Biological touch receptors: Mechanoreceptors

Human skin is a viscoelastic material consisting of two main layers: the outer epidermis (having a thickness of approximately 0.06 - 0.12 mm) and the dermis (having a thickness

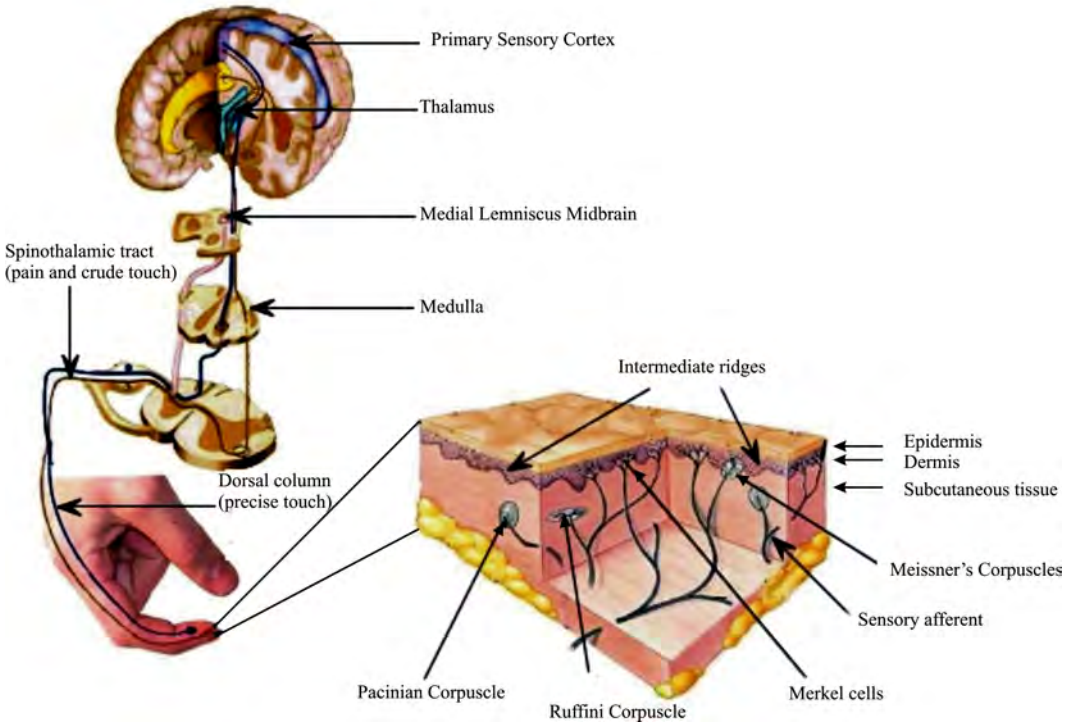

FIGURE 2.1: Organisation of the somatosensory system showing tactile signal transmission from fingertips to somatosensory area of brain (Adapted from [25])

of approximately 1 - 4 mm) [26], which is supported below by a layer of subcutaneous tissue. The skin surface of the human fingerpad consists of epidermal (papillary) ridges or fingerprints that are approximately 0.1 mm in height and 0.4 mm in width. At the junction between the epidermal and dermal layers there are undulations, known as the intermediate ridges, which consist of irregular, wavy epidermal tissue that extends into and interlocks with the dermis [27]. Each papillary ridge is positioned directly above its corresponding intermediate ridge.

When mechanical stress is applied to skin via touch, the stress is transmitted through the skin to the embedded mechanoreceptors, which act as transducers, converting the mechanical stimulus into neural signals. There are approximately 17,000 mechanoreceptors innervating the glabrous or hairless skin of the human hand, with the highest density present in the

fingertips, the preferred site for haptic exploration [28]. They can be classified into four main types, varying in their structure, function and distribution within skin (Fig. 2.2) [29]:

- Merkel cell complexes, located at the epidermal dermal junction (accounting for about 25% of the mechanoreceptors of the human hand), thought to be responsible for coding of surface form and texture.

- Meissners corpuscles, located in the dermis (accounting for about 40% of the mechanoreceptors), thought to be responsible for coding of low frequency vibrations.

- Pacinian corpuscles, located deep in the dermal and subcutaneous layers (accounting for $10 - 15\%$ of the mechanoreceptors), thought to be responsible for coding of high frequency vibrations.

- Ruffini endings, located in the mid dermal layers (accounting for about 20% of the mechanoreceptors), thought to be responsible for the coding of skin stretch.

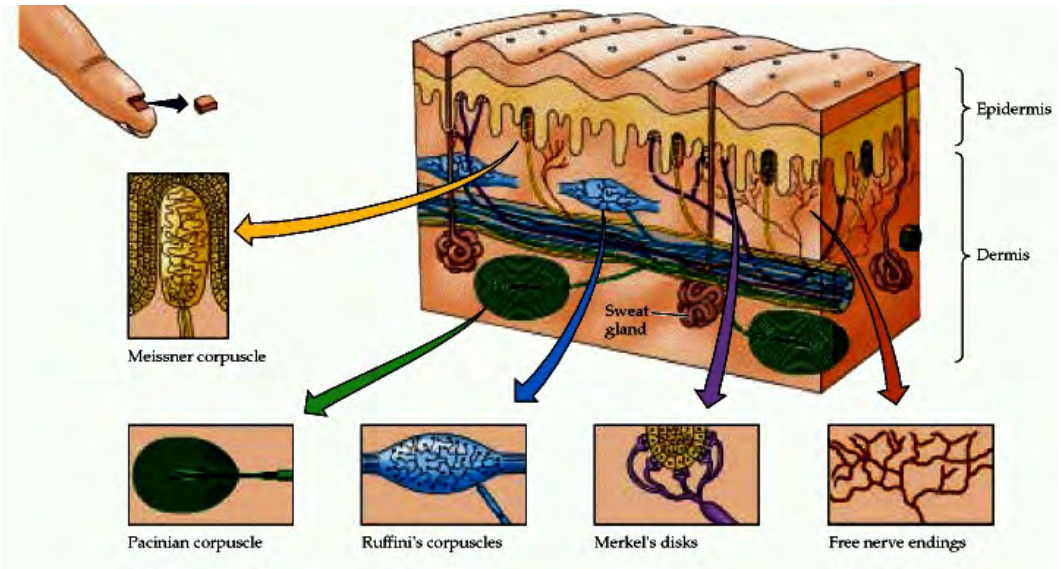

FIGURE 2.2: Mechanoreceptors in glabrous skin of the human hand [29]

The mechanoreceptors are innervated by afferent nerve fibres which are nerve fibres that carry impulses from a sensory receptor to the central nervous system. Afferent fibres that innervate mechanoreceptors have conduction velocities between 35 - 70 m/s [30]. The tactile afferent neuron together with its specialised endings (mechanoreceptors) is termed a tactile unit [31].

Tactile units are classified based on their ability to adapt to a constant mechanical stimulus and the size of their receptive field [29], which is the two-dimensional sensitivity profile of an individual tactile unit [31]. Thus tactile units that respond to a changing stimulus (during application or withdrawal of the stimulus) but not to a static stimulus are termed rapidly adapting (RA) or fast adapting (FA), and tactile units that generate a sustained response for as long as a stimulus is present are termed slow adapting (SA) units. These are further classified into type I units for receptors with small receptive fields and well defined borders, and type II for receptors with large receptive fields and obscure borders. The end organs of FA I and SA I afferent units are the superficially located Meissners corpuscles and Merkel cell complex, respectively. The end organs of FA II and SA II units are the deeply located Pacinian corpuscles and Ruffini endings, respectively [32].

Each of the four mechanoreceptive afferent systems respond to different aspects of a stimulus and serve a distinctly different perceptual function. The selective response of each unit is thought to be a result of the following factors [31, 32]:

- the morphology of the mechanoreceptors
- the location of the mechanoreceptors within the skin
- the number and distribution of mechanoreceptors for a single tactile afferent

Various studies have been conducted to assess functional properties and to identify relevant stimuli for each type of unit. Contributions from the fields of psychophysics and neurophysiology have been important in providing an insight into the nature of human tactile perception. Psychophysical measures define the relationship between varying textures presented to the finger and their associated behavioural responses or interpretations. Neurophysiological techniques involve recording of neural activity in peripheral nerves and the brain in response to various stimuli. A procedure called microneurography, introduced by Vallbo and Hagbarth in 1967 is commonly employed in the study of afferent fibres [33]. It involves the insertion of a tungsten electrode (with a tip diameter of 5-15 μm) through the skin of awake human subjects to facilitate electrophysiological recordings of neural signals transmitted by single sensory afferent nerve fibres (Fig.2.3). Thus, the assessment of responses of each type of mechanoreceptor unit to known stimuli has been possible.

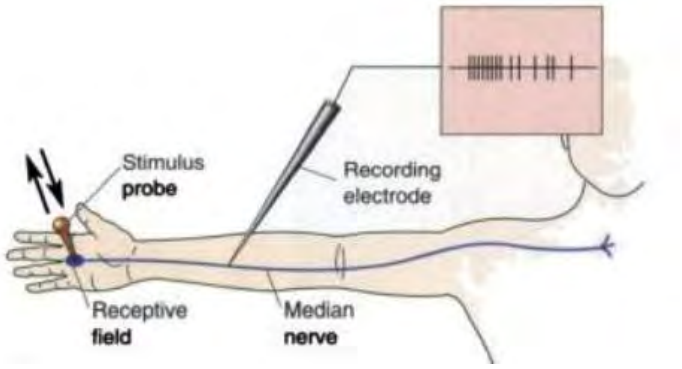

FIGURE 2.3: Microneurography technique involving the insertion of a microelectrode to access a single primary afferent nerve and record its emitted action potentials [34]

Fig. 2.4 shows a schematic of the response characteristics of the four different tactile units to a ramp and hold stimulus via indentation of the fingerpad [35]. While the slowly adapting SA I units respond during the entire duration of the applied stimulus, the fast adapting FA I and FA II units only fire impulses during transient phases of the stimulus.

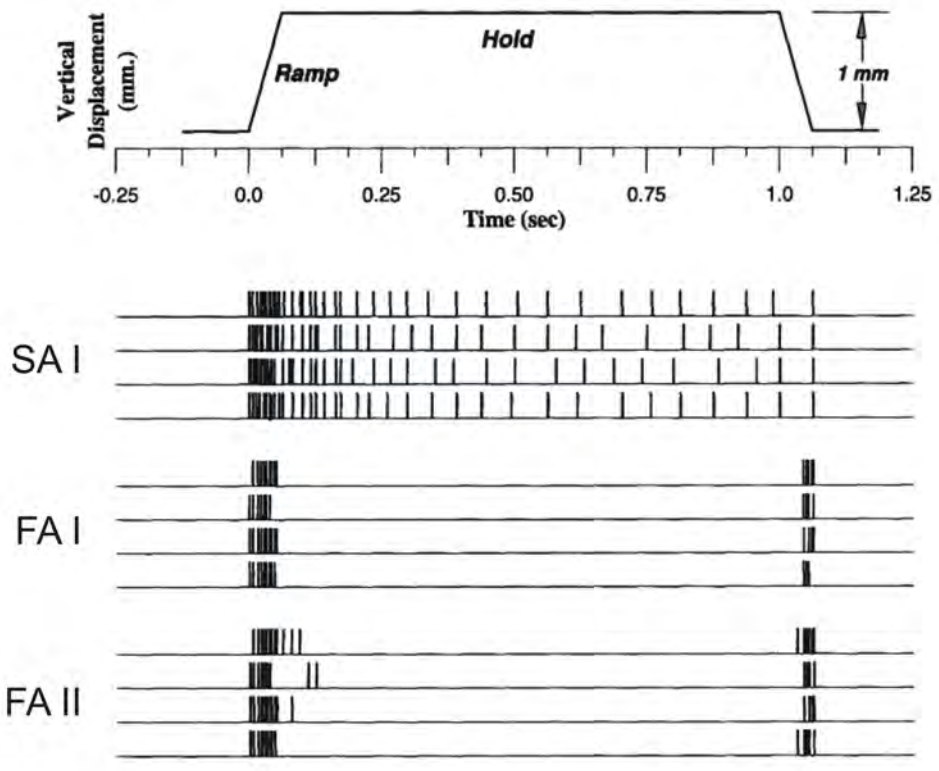

FIGURE 2.4: Schematic image of impulse discharge of different mechanoreceptors in the human fingerpad to indentation [35]

A brief summary of the main features of each mechanoreceptor can be found in Table 2.1.

TABLE 2.1: Response characteristics of glabrous skin mechanoreceptors [32, 36]

Mechanoreceptor type	Receptive field	Afferent type	Stimuli	Frequency sensitivity (Hz)
Merkel cells	small well defined	SA I	sustained pressure	0 - 30
Meissners corpuscles	small well defined	FA I	velocity, flutter	10 - 60
Pacinian corpuscles	large obscure	FA II	vibration	60 - 400
Ruffini endings	large obscure	SA II	skin stretch	0 - 15

Slowly adapting type I (SA I) afferent units

SA I afferents innervate the human fingertip at an estimated density of 70 afferents/ cm^2 [28]. They respond to sustained indentations with a sustained discharge of nerve impulses. As previously mentioned, the end organs of the SAI afferent are assumed to be the Merkel cell complexes. These units code constant or low frequency pressure and provide the information on which form and texture perceptions are based [32, 37]. They are located about 700 - 1000 μm below the skin surface in the epidermis at the tip of intermediate epidermal ridges (Fig. 2.5) and are concentrated in touch sensitive areas such as the fingerpads and feet [38]. They have an oval shape and measure 10 μm - 15 μm along their long axis [35]. They are present in clusters with one SA I unit branching to upto ten Merkel cell receptors [39]. Inter-receptor spacings are of the order of 1 mm [32]. The high density of SA I afferents in the human hand and their small receptive field sizes are suggestive of their role in high spatial resolution of the human hand and in coding of fine spatial features.

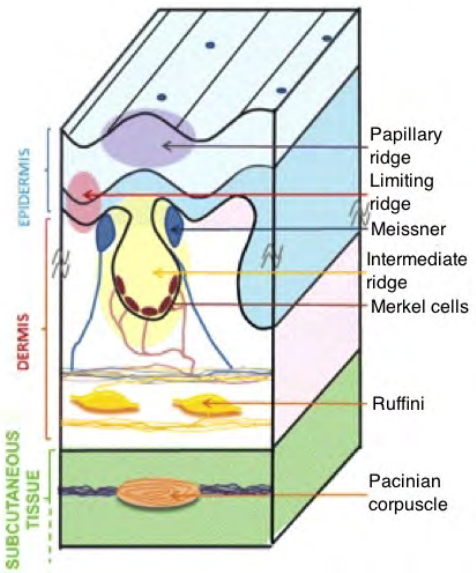

FIGURE 2.5: Skin structure showing papillary and intermediate ridges and the location of mechanoreceptors relative to these structures [25]

To understand the roles of tactile afferent units in tactile spatial coding, their responses to scanned braille patterns (a digital code system based on six cells in a 3 $\times$ 2 pattern in which the cells are placed 2 - 3 mm apart) were assessed by Philips et al. in 1990 [40]. They found that SA I afferent responses provided the most acute representation of the Braille dot patterns, denoting their significance in the coding of spatial features of a stimulus.

The local stimulus for SA units is hypothesised to be maximum compressive strain or strain energy density at the receptor location [41]. An increase in indentation depth leads to a proportional increase in their discharge rate [42]. They are sensitive to spatial and temporal components of a stimulus and have a range of thresholds/ sensitivity with the least sensitive afferents having thresholds ten times that of most sensitive fibres. Receptive field diameters of these units are approximately 2 - 3 mm [32]. Within their receptive fields, the SA I afferents are known to have hotspots, which are locations of increased sensitivities [32].

Fast-adapting type I (FA I) afferent units

FA I afferents innervate the human fingertip at an estimated density of 141 afferents/cm^2 [28]. The end organs of these units are the Meissner corpuscles, which are located in the dermal papillae at a depth beneath the epidermal surface varying between 100 μm and 500 μm (Fig. 2.5). The dimensions of these corpuscles are in the order of 100 μm $\times$ 50 μm [35]. They comprise cell layers, each that cushion and enfold two to six RA afferents. Their rapid adaptation to constant stimulus has been attributed to their structure.

FA I afferents are mainly sensitive to low frequency vibrations (less than 60 Hz) or flutter, slip, and motion across the skin surface giving feedback signals required for grip control [30, 37, 43]. When the finger is dragged over a surface, the fingertip is loaded laterally and

vibrations are induced due to the undulating geometries of the papillary and intermediate ridges. These vibrations are thought to mechanically stimulate the meissners corpuscles. They are protected from large, low-frequency skin displacements by the fluid-filled Meissner corpuscle within which they reside. Receptive field diameters of these units are approximately 2 - 3 mm and these units respond to stimuli relatively uniformly over their entire receptive field [32]. The RA afferent response begins to saturate at indentations of about 100 μm and is insensitive to the height of surface features above 300 - 400 μm [42], [37].

Fast-adapting type II (FA II) afferent units

The end organs of the FA II afferents are the Pacinian corpuscles (PC). The length of the PC range from 300 - 1500 μm and their diameter varies from 200 - 700 μm [35]. They have an onion like layered structure with as many as 70 lamellae enclosing a single afferent. This structure allows the PC unit to function as a high pass filter, preventing the transduction of slow mechanical events but signalling higher frequency vibrations (60 - 400 Hz) demonstrating maximum sensitivity in the 200 - 300 Hz frequency range [32]. The most sensitive FAII units respond to 10 nm of skin motion at 200 Hz [32].

In 1965 Loewenstein et al. showed that when stripped off their onion like capsule layers leaving the bare axon ending, Pacinian corpuscles became more sensitive to steady pressure and responded like slowly adapting units [44]. Thus they concluded that it was the layered capsule structure that was responsible for the selective sensitivity of these units to vibrating high frequency stimuli. Fig. 2.6 shows the response of a single isolated pacinian corpuscle to an indenting probe. The intact corpuscle generated an action potential at the onset and offset of stimulus and did not respond during steady state indentation phase. On the other

hand, the corpuscle that was stripped off its layers gave a prolonged response to indentation, with a decreased rate of adaptation to steady state stimuli.

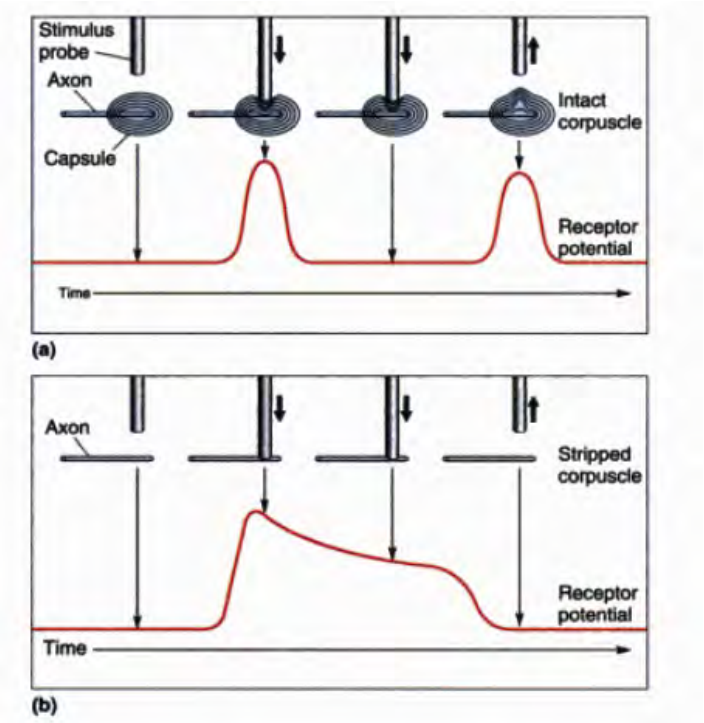

FIGURE 2.6: Adaptation in the response of an (a) intact and (b) stripped Pacinian corpuscle to applied mechanical stimulus [34]

The FA II afferents have large receptive fields (with an area ranging from 4 to 44 cm^2) and are therefore poor at providing information on spatial detail [45]. However they provide information on distant events through vibrations transmitted for example through hand held objects.

Slowly-adapting type II (SA II) afferent units

SA II units are located deeper in the dermis and respond to skin stretch around joints and fingernails [2]. Ruffini corpuscles, the end organs of SA II units, are spindle shaped 500 - 1000 μm long encapsulated structures with a diameter of 200 μm in their central section and

20-40 μm near their poles [35]. Their receptive fields are approximately five times larger than those of SA I afferents.

2.1.2 Tactile information transfer and encoding

The perception of any touch sensation is facilitated by an information flow that comprises a series of events that follow the activation of a mechanoreceptor exposed to a particular stimulus. In response to the stimulus, the receptor generates action potentials or electrical nerve impulses. In the following, the mechanism for generation of action potentials is briefly summarised.

The resting potential of the neuron is approximately -70 mV relative to the membrane exterior. This potential is maintained through the sodium potassium pump, which maintains an excess of K^+ ions in the interior of the membrane and an excess of Na^+ ions exterior to the membrane. In response to stimulation such as mechanical deformation, the Na^+ channels of the neural membrane open which causes an influx of Na^+ ions into the membrane leading to an increase in potential to approximately +30 mV (depolarisation). The opening of Na channels is followed by the opening of K^+ channels that causes K^+ ions to diffuse out of the cell, thereby dropping the potential of the membrane (repolarisation) down to -90 mV. Thus an electrical pulse of about 100 mV is generated. The membrane potential returns to the normal resting phase (-70 mV) through active transport of ions. Once an action potential is initiated, it propagates along the nerve axon automatically. The local reversal of the membrane potential is detected by the surrounding voltage-gated ion channels which subsequently open.

In this manner, action potentials are generated and propagated via peripheral nerve fibres

to the spinal cord and then to regions of the brain where the information is decoded and the sensation relating to touch is perceived. The intensity of the stimulus signal is registered as the number and frequency of pulses generated by the neural activity.

The primary somatosensory cortex (Fig. 2.7(a)) is a part of the brains cerebral cortex that is dedicated to processing information related to touch. Different regions of the somatosensory cortex area are uniquely attributed to specific parts of the body (Fig. 2.7(b)). A representation of the proportion of the somatosensory cortex dedicated to each part of human body is known as the sensory Homunculus. This is essentially a mapping of the body in the somatosensory cortex where its area is dependent on the amount of somatosensory input from that area. Fig. 2.7(a) shows a model of what man would look like if the body were to grow in proportion to the size of their representation in the human brain. There is a disproportionately large area of cortex devoted to processing signals from the hands implying that a significant amount of processing is implemented for sensory information therefrom.

2.1.3 Tactile sensing characteristics of the human fingerpad

As discussed in the previous sections, there is a division of function among the four different tactile units innervating the fingerpad. The response of a population of receptors represents a spatio-temporal code for the applied mechanical stimulus. Thus perception of tactile sensation results from the interpretation of the collective responses of the different mechanoreceptors. The responses of the mechanoreceptors to applied stimuli are known to be highly non-linear [32, 46].

There is a trade-off between the spatial and temporal resolving capabilities of the tactile units. The SA I units, with their small receptive fields, are responsible for the high spatial

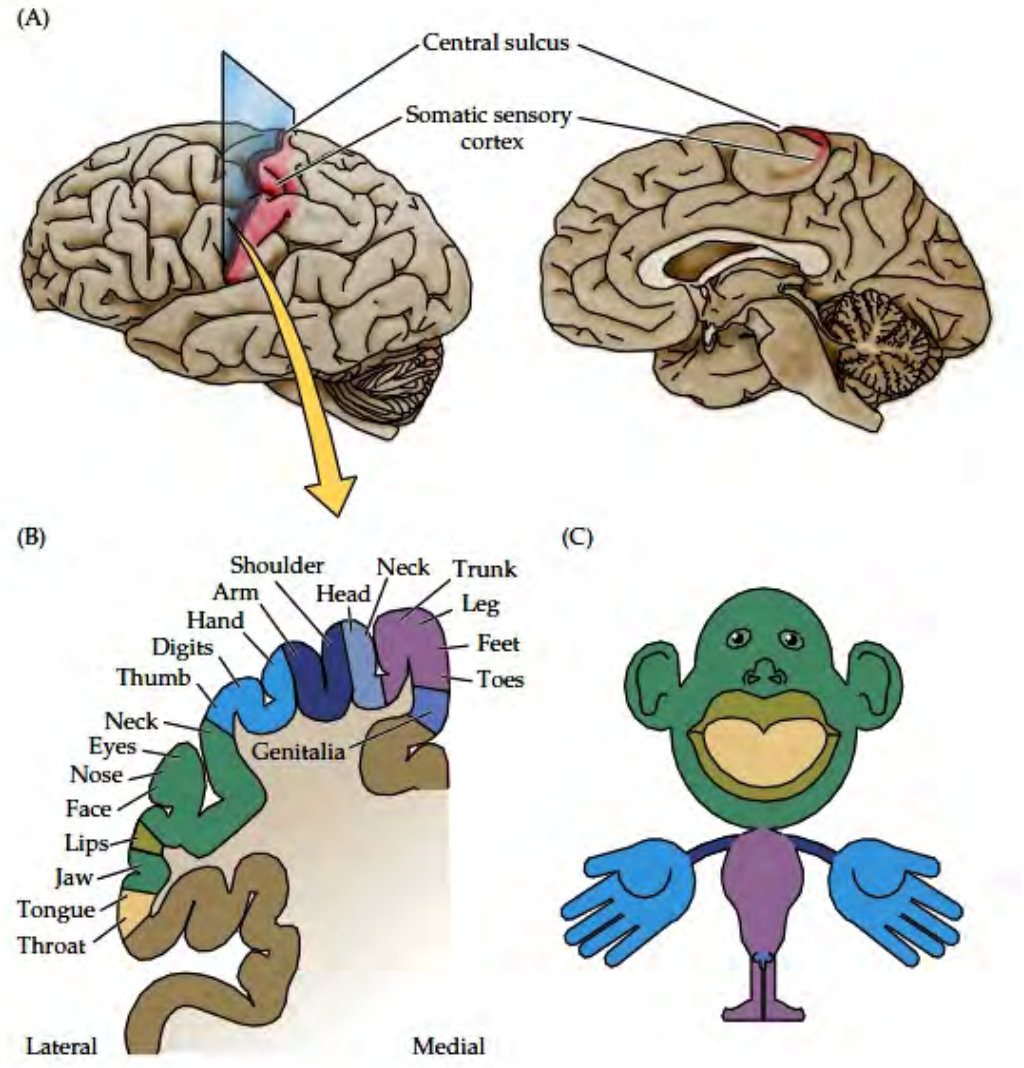

FIGURE 2.7: (a) Location of somatosensory cortex in the human brain, (b) Representation of regions of human body in somatosensory cortex, (c) Model of sensory Homunculus. The amount of somatic sensory cortex devoted to the hands and face is much larger in comparison to the the relative area of body surface in these regions [29]

resolution of the fingertip. They respond mainly to low frequency stimulation showing a peak in sensitivity at around 5 Hz [47]. Conversely, the FA II units are poor at providing spatial details of a stimulus, however they are sensitive to high frequency signals, with peak sensitivities $\geqslant$ 80 Hz [47]. The FA I units have peak sensitivities at 10 - 40 Hz [47].

Spatial resolution

A measure of tactile spatial resolution commonly referred to in the literature is the two point discrimination threshold; the smallest distance at which two simultaneous point stimuli can be perceived as being distinct. It is a function of the innervation density of tactile afferents in the skin [48]. Normal values for two point discrimination threshold in the human finger pad range from 2 - 3 mm [49, 50]. Another method for measuring spatial resolution, where gratings varying in periodicity were used to assess discrimination capability, has shown the spatial resolution on the fingertips is about 1 mm [46, 51].

Force sensitivity

Threshold values of force sensitivity have been investigated by applying a step function mechanical stimulus on the skin using nylon monofilaments. On the fingertips, the force threshold was found to be 1 - 2 mg [31].

Vibration perception

The human skin is sensitive to a range of sinusoidal frequencies from about 2 to $>$ 500 Hz [31]. The FA I system is tuned to lower freqencies (upto about 40 Hz) and the FA II system is tuned to higher frequencies with a greater sensitivity to frequencies in the range of 200 - 300 Hz.

Form and texture perception

Texture refers to distributed small scale surface properties and comprises many perceptually distinct characteristics such as roughness, stickiness, hardness and spatial density [52]. A

textured surface has undulations or protrusions along its surface. Texture perception is subjective. Studies investigating perception of roughness using gratings varying in spatial periodicity have shown that roughness perception increases with an increase in groove widths [53]. It has been shown that roughness perception depends on element height, diameter, shape, compliance and density. Important early observations were that scanning velocity, contact force and friction between the finger and a surface have minor or no effects on roughness magnitude judgments [54]. For judgement of roughness, an average scanning speed of 2 cm/s (range 1 - 25 cm/s) and an average normal force of 1.1 N [54] (range of 0.3 - 4.5 N) is used by the subjects [55].

Katz proposed in 1925 the duplex theory of texture perception, suggesting that texture perception is mediated by vibrational cues in the case of fine textures and by spatial cues in the case of coarse textures [56]. Spatial cues are determined by the size, shape and distribution of surface elements. Temporal cues are determined by the rate of vibration as skin moves across fine textures. Currently there is no consolidated agreement in the literature regarding the neural mechanisms underlying texture perception in humans. Hollins and Risner [57] proposed a duplex mechanism supporting Katz's hypothesis. They showed that elimination of movement resulted in diminished performance of fine texture discrimination but had no effect on discrimination of coarse surfaces. Conversely, Yoshioka and colleagues proposed a unified paradigm via the spatiotemporal modulation of the neural activity of SAI afferents [58]. However, an established finding is the enhanced discrimination sensitivity obtained as a consequence of relative motion between the finger and the surface. It has also been shown that SA I afferents evoke ten times greater impulse rates in response to dynamic vs. static stimuli [46]. With lateral movement, features protruding 0.1 μm above a smooth

background can be detected [59]. While detecting textures, humans tend to slide their finger over the surface of interest; this relative motion, eliciting vibratory mechanical waveforms at finger-object interface, is hypothesised to be a requirement for the perception of fine textures [60], whether the neural encoding mechanism is actually temporal or spatiotemporal.

2.2 Artificial tactile sensors

In the last thirty years there has been tremendous progress in research on the design and development of artificial tactile sensors. Reviews on tactile sensing in the 80s and 90s can be found in works of Jayawant (1989) [61] and Lee and Nicholls (1999) [1]. More recent reviews can be found in Eltaib and Hewitt (2003) [3] as well as Dargahi and Najarian (2005) [16]. While sensor requirements and transduction mechanisms were explored in earlier works, more recently the focus has been on the development of sensor prototypes that are tailored towards specific applications.

2.2.1 Tactile sensor transduction mechanisms

Some of the commonly used transduction mechanisms employed in tactile sensing are summarised below.

Resistive devices

Resistive based tactile devices rely on the change in electrical resistance with applied pressure. Flexible materials such as conductive polymers have been used to implement flexible tactile sensors. Although such devices have the advantage of simplicity, they suffer from

limitations relating to their long time constant, low accuracy, poor long term stability, nonlinear force-resistance characteristics, significant hysteresis and low spatial resolution [62, 63]. Other devices implemented metal strain gauges attached to a flexible membrane. However such devices suffered from limitations due to instability of adhesive layer. Further they require a bridge amplifier with consequent large size and power consumption [64].

Piezoresistance refers to the property of semiconductors (such as germanium, polycrystalline silicon, amorphous silicon, silicon carbide, and single crystal silicon) by which they change their electrical resistance with applied strain. The piezoresistive effects of silicon and germanium were first demonstrated by Smith in 1954 [65]. The piezoresistive effect of semiconductor materials is greater than the geometrical effect in metals and therefore such device have almost two orders of magnitude greater sensitivity compared to strain gauge based devices [66]. This is because the stress dependent effect in piezoresistive materials is due to the mobility of charge carriers which changes as a function of the material volume. Changes in the material volume cause changes in the energy gap between valence and conduction bands, changing the number of carriers and hence causing resistivity change.

Piezoresistive technology is most widely implemented in tactile sensor development. Initially silicon strain gauges were bonded to metal diaphragms. More recently, ion implanted/diffused piezoresistors have been incorporated within high stress regions of silicon sensing diaphragms to form the sensing device [62]. The widespread use of this transduction mechanism is because of advantages in terms of low fabrication costs, high sensitivities and simple electronic interfaces [67]. However the materials exhibit temperature dependence due to the modifications in charge carrier mobility over temperature ranges and therefore some form of temperature compensation mechanism is required.

Piezoelectric devices

Piezoelectric materials develop an electric charge on their surface proportional to the applied pressure. Commonly used piezoelectric materials used to make tactile devices include polyvinylidene fluoride (PVDF) polymers, Zinc oxide (ZnO) and lead zirconate titanate ($PbZrTiO_3$ or PZT) [26, 68]. PVDF polymers have advantages over the ceramic based devices (ZnO and PZT) in terms of their flexibility, chemical resistance, durability, low cost and ease of processing [26, 69]. However, in tactile devices made from such materials the applied stress tends to propagate over the adjacent sensing elements, increasing the cross talk [70]. These devices also tend to be prone to hysteresis [26]

Capacitive devices

Capacitive sensors consist of two conductive plates (one which acts as a sensing diaphragm) separated by a dielectric material. On application of pressure, the diaphragm deforms and changes the distance between the electrodes. This results in a change in capacitance, which can be measured. For a parallel plate capacitor, the capacitance (C) between the plates is given by 3.2:

$$\mathrm{C} = \varepsilon_0 \varepsilon_\mathrm{r} \frac{\mathrm{A}}{\mathrm{d}} \tag{2.1}$$

Where ε_0 is the permittivity of free space (8.854×10^{-12} F/m), ε_r the dielectric constant of the medium between the plates, A is the area of the plates and d is the distance between them.

Advantages of capacitive sensors are their increased sensitivity, low temperature sensitivity, low power consumption and long term stability [71]. However, they require more

complex signal processing in comparison with piezoresistive devices.

Optical

Optical sensors use the properties of optical reflection between media of different refractive indices to sense displacements. In tactile sensing, such devices can be realised by modulating the intensity of light through movement of an obstruction into the light path. Another method uses the photoelasticity phenomenon. Here light is passed through a photoelastic medium (such as polyurethanes, acrylic resins) which on receiving stress alters the polarisation plane. Consequently there is a change in intensity of light (as a function of applied force) which is picked up by a detector. Optical sensors are immune from external electromagnetic interferences [63]. However, construction of dense arrays using such principles is technologically complex.

2.2.2 Bioinspired tactile sensors

Due to the performance characteristics and versatility of the biological system of touch, work on developing artificial tactile sensors is often inspired by their natural antetypes. Inspiration drawn from the biological system is implemented through the incorporation of human skin like design features or functional characteristics. Design features that have been adopted include the use of multiple skin like sensing layers, conformable skin like sensor packaging, fingerprint ridges and curved geometry of finger surface. The sensing capability of the human hand is also used as a tactile model for defining engineering features of a tactile sensing system such as spatial and temporal resolution, bandwidth and force sensitivity. In the following, an overview of some key works in development of bio-inspired tactile sensors is

given.

In 1984, Dario et al. [68] reported one of the earlier works in anthropormorphic tactile sensors for use in prosthetics or robotics. The device was a composite, layered multi-sensor structure, mimicking the dermal and epidermal skin layers. The design included a lower PVDF/ conductive silicone rubber stack layer to measure the pressure exerted by an object on the tactile sensor and an upper thin PVDF membrane-like layer to measure the small pressure variations required for texture analysis (Fig. 2.8). The resulting composite structure was demonstrated to detect contact pressure, hardness, surface textures, thermal properties and tactile images of surfaces.

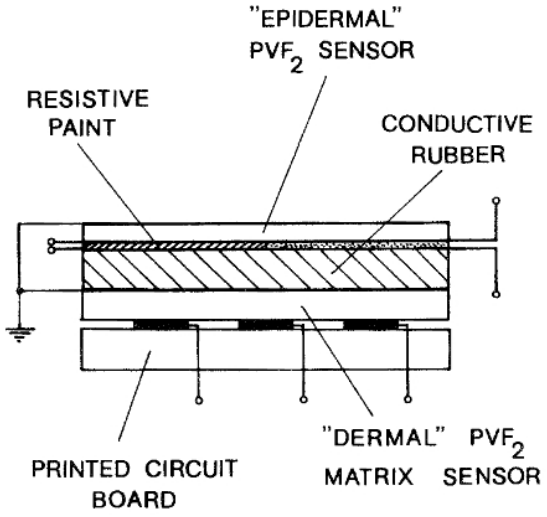

FIGURE 2.8: Schematic of multi layer tactile sensor developed by Dario et al. (1984) [68]

Yamada et al. (2001) [72] proposed an elastic finger skin imitating certain characteristics of the human finger to control the action of grasping an object. The principle sensing elements were strain gauges bonded to 1 μm thick phosphor bronze plate cantilevers. They were embedded within a silicone rubber finger consisting of ridges imitating fingerprint ridges (Fig. 2.9).

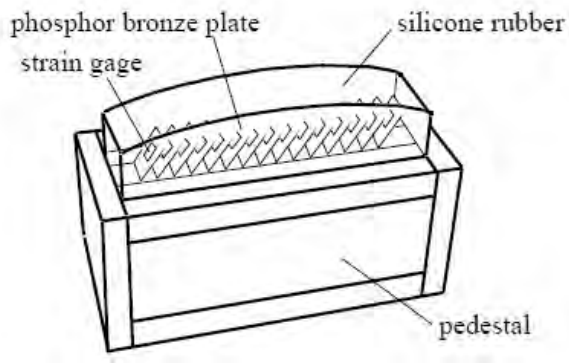

FIGURE 2.9: Artificial skin having fingerprint like ridge structures with strain gauge sensing elements [73]

Mukaibo et al. (2005) [74] described the development of a texture sensor mimicking the tissue structure and perceptual mechanisms of the human finger for identifying the difference in roughness, softness and frictional properties of various materials. Design features incorporated into the device included: two skin layered structure (made from silicone rubber of different stiffnesses) mimicking the dermal and epidermal layers, finger print like features on the skin layer, bone and nail like components and distributed sensor elements (consisting of 5 strain gauges). They demonstrated the use of the device to obtain information on roughness, softness, and friction of a contacting object.

Edin et al. (2006) [11] proposed a bioinspired approach for the design of a tactile sensing system for a prosthetic hand. They developed on-off contact sensor arrays and a tri-axial force sensor (using strain gauges). They demonstrated that their design functionally provided the same information as biological touch receptors for lifting tasks.

Hosoda et al. (2006) [75] proposed the design of an anthropomorphic soft fingertip with distributed strain gauges and PVDF sensors (Fig. 2.10). The structure of the fingertip was designed to be similar to the human finger, including a bone like layer, skin layer and randomly distributed receptors. The strain gauges embedded adjacent to the skin surface were

used to sense the local static strain between the skin and the object surface. Those embedded close to the bone were expected to sense the total force exerted to the finger. The PVDF film was used to sense the strain velocity rather than the static strain. They demonstrated the ability of the device to discriminate between vinyl, cork, paper and wood.

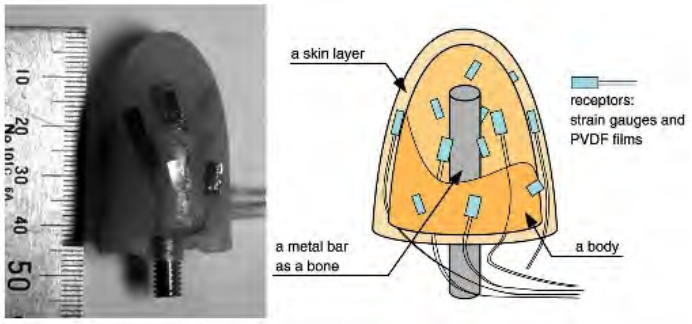

FIGURE 2.10: Anthropomorphic fingertip with distributed sensing elements [75]

Wettels et al. (2008) [76] developed a tactile sensor array aimed at mimicking the mechanical properties and distributed mechanoreceptor arrangement of touch receptors in the human fingertip. The device incorporates a rigid core surrounded by a weakly conductive fluid and a silicone elastomeric skin layer (Fig. 2.11). When an external force is applied to the skin, the fluid path deforms, resulting in an impedance change which is measured through multiple electrodes mounted on the rigid core. The sensing device demonstrated the ability to detect forces ranging from 0.1 to 30 N producing impedances ranging from 5 to 1000 kΩ. By systematically applying indentations of 4.5 mm to the sensor in locations corresponding to increasing distances away from the sensing electrode, the spatial resolution of the device was shown to be less than 2 mm.

The devices described above have significantly contributed towards the development of anthropomorphic tactile devices. However to achieve tactile sensors with attributes similar to the biological sensors in terms of sensor dimensions, density/unit area and spatial resolution,

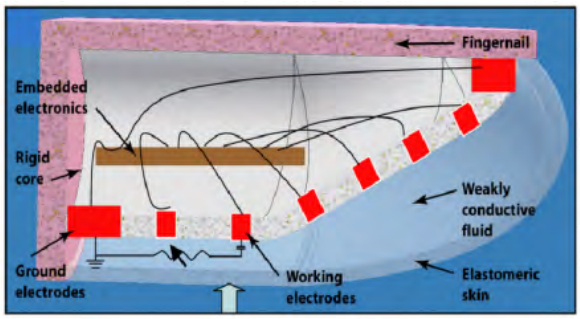

FIGURE 2.11: Tactile sensor array developed by Wettels et al. with an impedance based sensing principle [76]

the use of microelectromechanical systems (MEMS) technology is explored.

2.2.3 MEMS technology in tactile sensing

Microelectromechanical systems (MEMS) or Microsystems technology (MST) refers to devices that have characteristic lengths between 1 μm - 1 mm, that combine electrical and mechanical components, and that are fabricated using integrated circuit batch-processing technologiese [77]. A MEMS system may consist of a micromechanical sensor, actuator and microelectronic circuit in a single device. The techniques and practices involved in the development of devices with micron scale dimensions is termed Microengineering. MEMS devices have applications in a range of industrial and medical sectors. Some popular examples include digital mirror displays, inkjet printheads and nozzles, automotive safety systems (such as integrated accelerometers for airbag deployment), biomedical sensors and drug delivery systems.

Advances in the semiconductor integrated circuit (IC) industry have played a significant role in the growth and progress of the MEMS field [78]. The development of ICs began in 1958 and a trend in this technology has been for the number of transistors in a chip to

double every 18 months. This is referred to as Moore's law and is related to the decrease in device sizes made possible because of advances in silicon processing [79, 80]. MEMS devices and structures are fabricated using techniques borrowed from the IC industry, such as patterning with lithography, deposition, and etching as well as a range of specifically designed micromachining techniques [80].

The influence of the length scale should be taken into account in the design and fabrication of micro-scale devices. With the decrease in the scale of dimensions, there is an increase in the surface to volume ratio of an object. As a result, forces that are related to surface area (such as surface tension) become dominant and are more influential in comparison to forces relating to volume (such as mass) [81, 82]. For example, inertia has greater effect on larger-scale systems, while micro-systems are more influenced by surface effects. Consequently, surface effect induced strong adhesion, friction and wear can cause major problems with respect to fabrication yield and operation lifetime of many MEMS devices [83].

Some advantages of MEMS include [84]:

- Possibility for high volume batch production and low cost
- Reduced size, mass and power consumption
- Improved reliability

As discussed in previous sections, the biological sense of touch allows multimodal comprehensive evaluation of contacted objects through the rich tactile data provided by the mechanoreceptors. The use of MEMS technologies allows the possibility to mimic the functionality of the biological system through integration of a variety of sensing structures within a small area. Additionally, the use of MEMS technologies in the realisation of tactile sensors

is motivated by the following inherent advantages[6]:

- Miniature size allowing high density of elements to be incorporated within a small area
- Integration of electronics and sensing elements on same substrate
- Low cost production through the use of batch fabrication technologies

Review of MEMS tactile sensors

An overview of MEMS tactile sensors to date is given in Table 2.2. As can be noted from Table 2.2, the most commonly sensing technologies employed are piezoresistive and capacitive.

The intended application of the sensors defines their performance requirements in terms of sensitivity, range etc. For instance, a tactile sensors embedded in a cathether for pressure measurement has different specifications compared to a tactile device for a robotic finger. Further, within robotics, there are two different requirements for sensors: Those for enabling the robot to effectively perform lifting and grasping tasks and sensors for giving robots the ability to characterise different surfaces.

TABLE 2.2: Overview of the features of MEMS based tactile sensors developed to date

Author (Year)	Chun and Wise 1985 [85]	Sugiyama 1987	Suzuki 1990 [86]
Description	capacitive Si diaphragm	piezoresistive Si_3N_4 diaphragm	capacitive Si diaphragm
Array	8×8	32×32	32×32
Diaphragm size	$1200 \times 1200 \times 10\ \mu m^3$	$100\ \mu m\ \varnothing$	$132 \times 300 \times 2.5\ \mu m^3$
Pitch	2 mm	0.35 mm	0.5 mm
Sensitivity	10 V/N	100 V/N	27 pf/N
Force range	0.5 N	-	0.01 N
Fabrication	bulk, surface micromachining electrostatic bonding 5 mask steps	surface micromachining	bulk, surface micromachining electrostatic bonding 4 mask steps

Author (Year)	Beebe 1995 [62]	Chu 1996 [87]	Gray 1996 [88]	Mei 2000 [89]
Description	piezoresistive Si diaphragm torlon dome	capacitive Si diaphragm	capacitive polySi diaphragm	piezoresistive Si diaphragm
Array	1	3×3	8×8	4×8
Size	2 mm radius	0.45 mm radius	$< 100 \times 100$ μm^2	4×4 mm^2
Pitch	6 mm	2.2 mm	≈ 100 μm	4 mm
Sensitivity	1.4 mV/N	0.13 pF/g (F_z) 0.32 pF/g (F_y)	0.05 (%ΔC/C$_0$)/μN	13 mV/N
Force range	100 N	0.01 N	0.02 N	50 N
Fabrication	bulk micromachining Si fusion bonding	bulk micromachining glass etching anodic bonding	surface micromachining	bulk micromachining double side photolithography

Author (Year)	Leineweber 2000 [90]	Beccai 2005 [10]	Wisitsoraat 2006 [67]
Description	capacitive polySi diaphragm	piezoresistive Si diaphragm	piezoresistive multi-layer AlN/Al/Cr
Array	8	1	1
Size	0.24×0.24 mm^2	1.5×1.5 mm^2	200×200 μm^2
Pitch	0.24 mm	-	-
Sensitivity	1.35 V/bar	0.026/N (normal) 0.054/N (shear)	0.2 mV/μN
Force range	3 bar	2 N	≈ 270 μN
Fabrication	surface micromachining	bulk micromachining 9 mask steps	1 photolithography sputtering 3 Ni μ-shadow masks

In addition to differences in design and performance, the devices reported in Table 2.2 also vary in terms of the fabrication processes adopted. Microfabrication is mainly grouped into bulk and surface micromachining.

In bulk micromachining, structures are formed from selective etching of a silicon substrate. The dominant material used in bulk micromachining is single crystal silicon; a material that has several advantages in terms of its mechanical properties, namely high strength and stiffness, high gauge factors and no hysteresis.

Surface micromachining involves formation of structural layer through film deposition, patterning and etching on a substrate wafer. In surface micromachining, the most commonly used materials are silicon nitride and polysilicon. However, these materials are inferior with regards to the internal stresses that tend to develop as a result of their deposition process.

Silicon micromachining for fabrication of tactile sensors has gradually evolved with the widespread development of MEMS pressure sensors [91]. A further discussion of MEMS fabrication is explored in Chapter 4.

2.3 Conclusions

In this chapter, the working principle of both the biological touch system and derived artificial approaches of bioinspired tactile systems were introduced and described. The biological system adopts an intelligent combination of many parallel functional processes, which are mutually and dynamically connected to each other in optimised harmony [92]. Four classes of mechanoreceptors supply the glabrous or hairless skin of the human hand. These are the Merkel cell complex, Meissners corpuscle, Pacinian corpuscles and Ruffini endings. Each of these receptors is sensitive to a particular parameter of mechanical stimulus and they function

to convert the mechanical stimulus to nerve action potentials. The four mechanoreceptor types vary in terms of their frequency responses, receptive field sizes and spatial distributions.

The tactile unit associated with the merkel cell complex (i.e. the SA I afferents) provides the information on which form and texture perception are based. The tactile units associated with the Meissners corpuscle (i.e. the FA I afferents) provide information about minute skin motion, thereby playing an important role in grip control. The system associated with the Pacinian corpuscles (i.e. the FA II afferents) is responsible for the detection of distant events through vibrations transmitted through objects or tools held in the hand. The system associated with the ruffini endings (i.e the SA II units) provide information for the perception of hand conformation and for the perception of forces acting on the hand.

Stimulation of each class of sensory afferents results in the perception of the specific sensation relating to them. For example, electrical stimulation of a single afferent associated with the Meissners corpuscle unit with a low frequency train evokes the sensation of intermittent tapping, which becomes flutter or vibration with increasing frequency. Similarly, stimulation of the Pacinian corpuscle units with a train of pulses generates the sensation of vibration which is frequency dependent. Stimulating the afferents associated with Merkel cell units causes a sensation of pressure whose magnitude increases with increasing frequency [93].

The biological tactile receptors offer rich, multi-modal data on tactile sensation which motivates a technical design that strives for mimicking their particular properties. Tactile devices developed to date for robotic applications have addressed aspects of the requirements for incorporation into an artificial finger. However, a device exhibiting a combination of mechanoreceptor like features in terms of design strategy and function is desirable.

In the following chapters, the focus turns to the development of a bio-inspired tactile sensor that facilitates incorporation into a robotic finger. The general requirements in the design of a prosthetic or artificial hand include [94]:

- Anthropomorphic appearance
- Low weight
- Low power consumption
- Modularity for low cost and easy maintenance
- Appropriate size

The design of tactile sensors to be embedded within an artificial finger of a prosthetic hand should take into account the above mentioned requirements in addition to providing its specific functional attributes. To achieve this, it appears reasonable to combine the technological advantages that are allowed by the use of microfabrication technologies, with the performance characteristics of biological tactile sensors.

With regard to the specific characteristics of the biological system, the bio-inspired sensing device needs to fulfil the following specifications:

- Provide rich data set of information on spatial features of a contacting surface and be sufficiently sensitive to code for differences in surface textures.
- Have tactile units with a density corresponding to that of the SA I and FA I mechanoreceptors at the fingertip (approximately 1 unit/mm^2)
- Provide a spatial resolution in the order of 1 mm (similar to human hand) which requires the sensors in an array to be closely spaced

- Have a working range up to several Newtons; as in most natural human manipulations, forces on the digits tend to range up to several Newtons [95].

- Be compatible with a conformable skin like covering layer

Since the SA I tactile units are mainly responsible for providing the function of form and texture recognition in the human fingertip, their performance characteristics serve as a guideline in the design of the sensor.

3

Tactile sensor design

Contents

Summary This chapter describes the design concept of the MEMS tactile sensor. Following an overview of the transduction mechanism employed, diaphragm design analysis is carried out using both analytical and numerical techniques. Finite Element Analysis (FEA)

solutions of the the final sensor designs are presented. Finally, the design of the signal acquisition electronics is described.

3.1 Transduction principle

In Chapter 2, an overview of MEMS tactile sensors to date was given. Piezoelectric, piezoresistive and capacitive technologies have been most commonly used in the implementation of such devices. Among these, capacitive sensors offer advantages in terms of higher sensitivity, long term drift stability, lower temperature drift and reduced power consumption [91, 96–98]; and are therefore capable of meeting the necessary requirements for an artificial finger based device. A capacitive operating principle was thus chosen for the tactile sensing device reported in this work.

3.1.1 Capacitive sensors

Capacitance is the electrical property which exists between two conductors separated by an insulator. It indicates how much charge can be stored in a conductor at a given potential. Capacitors are electrical components that have the ability to store electrical energy. They consist of two conducting surfaces separated by an insulating/dielectric medium. The capacitance can be defined as the ratio between the charge Q stored in the plates and the potential V between the plates. The unit of capacitance is the farad (F).

$$C = \frac{Q}{V} \tag{3.1}$$

The capacitance C between two conducting parallel plates separated by an insulator (neglecting fringing effects) is given by:

$$C = \varepsilon_0 \varepsilon_r \frac{A}{d_0} \tag{3.2}$$

where ε_0 is the permittivity of free space (8.854 $\times$ 10^{-12} F/m), ε_r is the dielectric constant of the medium between the plates (1 for air), *A* is the area of the plates and d_0 is the distance between them.

Thus the magnitude of capacitance is a function of the geometrical dimensions of the conducting plates and the dielectric medium.

In capacitive sensors a change in a physical parameter (such as the distance between the two plates due to applied pressure) causes a change in the capacitance that is monitored and used to provide information on the applied stimulus. A significant amount of work has been carried out on the development of MEMS based capacitive pressure sensors [99, 100]. Most commonly, such devices employ a deformable diaphragm that deflects due to variation in pressure. In a similar manner, capacitive tactile sensors employ a sensing diaphragm which, under applied load, deflects towards a fixed substrate (Fig. 3.1). This results in a change in the capacitance between the two plates that increases as a function of the applied pressure P. The capacitance under applied pressure, *C(P)* is given by [91]:

$$C(P) = \varepsilon_0 \varepsilon_r \int\int_A \frac{dxdy}{d_0 - w(x,y)} \tag{3.3}$$

where *w(x,y)* is the local deflection of the diaphragm.

The total capacitance change is the integral of capacitance change over a small area of the diaphragm. Capacitance change is a function of diaphragm deflection and is given by:

$$\Delta C = C(P) - C_0 = \varepsilon_0 \varepsilon_r \int\int_A \frac{dxdy}{d_0 - w(x,y)} - \varepsilon_0 \varepsilon_r \frac{A}{d_0} \tag{3.4}$$

where C_0 is the zero-pressure capacitance.

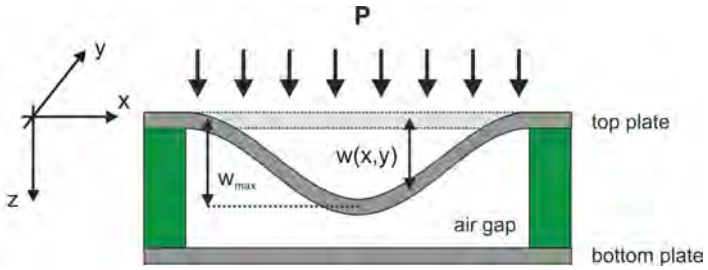

FIGURE 3.1: Pressure P applied to sensing diaphragm causes a deflection w(x) as a function of position, with the maximum deflection w_{max}

3.2 Choice of material

3.2.1 Single crystal silicon

The presented capacitive sensors are fabricated with single crystal silicon diaphragms. Silicon is commonly used in micromechanical sensors because of its well established electrical and excellent mechanical properties. It is an anisotropic crystalline material whose elastic behaviour depends on its orientation relative to the crystal lattice [101]. It is widespread in the IC and MEMS industries for the following reasons [80, 102]:

- The material is cheap and readily available
- It is a semiconductor whose resistivity can be adjusted from sub-mΩ cm to several kΩ cm by the process of doping
- The existence of its stable insulating oxide (silicon dioxide)
- The existence of its various well established processing techniques
- The possibility for integration with signal conditioning electronics

Single crystal silicon has attractive mechanical properties in terms of its high strength which exceeds steel, high fracture strength and reproducible mechanical and electrical properties. The tensile yield strength of silicon is 7 GPa. Its Young's modulus (E) depends on the crystallographic orientation and varies from 130 - 180 GPa [101]. The electrical properties of silicon can be modified by adding impurities (elements from group III and V of the periodic table). By adjusting doping concentrations, a range of material resistivities varying from 0.001 - 10000 Ω cm can be attained [80]. Dopants are introduced into silicon either by using ion implantation (by firing energetic ions directly onto silicon) during epitaxial growth or by diffusion from solid or gaseous sources. Following implantation, thermal annealing processes are carried out to limit any damage caused by ion bombardment, and to move dopant atoms into substitutional sites in the silicon crystal where they become electrically active.

3.3 Diaphragm analysis

3.3.1 Analytical solutions

The design of the deformable diaphragm of a capacitive sensor is important to determine the performance characteristics of the sensor with respect to its range, sensitivity and dynamic range. It is important to consider any induced mechanical stresses as a result of the applied pressure in order to assess if they exceed the yield stress of the diaphragm material; therefore making the device susceptible to failure. When designing sensing diaphragms, analytical calculations are used to provide a relatively quick insight into the diaphragm behaviour and to determine the affects of varying design parameters on sensor performance without the

need for computer intensive tools.

The response of deformable sensing diaphragms to the applied pressure depends on several factors, key among which are material properties, diaphragm shape and edge or boundary conditions. The deflection of a diaphragm is governed by two principle mechanisms: Bending moments/bending stress and tensile forces/membrane stress [103]. A renowned standard work in the analysis of plate deflection is by Timoshenko and Woinowsky-Krieger [104].

To conduct a preliminary analysis of sensor diaphragms, solutions based on small deflection plate theory were used. This is based on the assumption that the deflection of a diaphragms is small in comparison to its thickness. A maximum deflection of 30% of the diaphragm thickness [80] is allowed and the influence of tensile forces in not considered. The following main assumptions hold [80]:

- The diaphragm is flat with uniform thickness
- The material is homogeneous and isotropic
- Pressure is applied normal to the diaphragm plane
- The diaphragm deflection is less than 30% of the diaphragm thickness
- The elastic limit of the diaphragm is not exceeded
- There is no deformation in the middle plane
- Deflection is due to bending and no stress is experienced by the neutral axis

The relationship between the applied pressure P and the corresponding deflection w at any point (x,y) of a plate for small deflections is given by the fourth order partial differential

equation [104]:

$$\frac{\partial^4 w}{\partial x^4} + \frac{\partial^4 w}{\partial x^2 \partial y^2} + \frac{\partial^4 w}{\partial y^4} = \frac{P}{D} \tag{3.5}$$

Where *D* is the flexural rigidity of the plate, which is a measure of its stiffness.

The above equation can be solved using appropriate boundary conditions along the edge of the plate. In the following sections, the characteristic behaviour of different designs of silicon diaphragms to the applied pressure are investigated by using analytical simulations based on small deflection theory for thin plates. Diaphragms with circular, square and rectangular geometries were simulated. A Young's modulus of 170 GPa and a Poisson's ratio of 0.28 were assumed in all cases.

Circular clamped diaphragm

For a uniformly loaded clamped circular diaphragm of radius *a*, assuming small deflections, the deflection *w(r)* is given by [104]:

$$w(r) = \frac{P(a^2 - r^2)^2}{64D} \tag{3.6}$$

where *P* is the applied pressure, *a* is the radius of the diaphragm, *r* is the distance from the centre of the diaphragm and *D* is its flexural rigidity which is given by:

$$D = \frac{Eh^3}{12(1 - \nu^2)} \tag{3.7}$$

where *E* is Young's modulus, ν is the Poisson's ratio and *h* is the diaphragm thickness.

Thus, equation 3.6 can be rewritten as:

$$w(r) = \frac{3P(1-\nu^2)(a^2-r^2)^2}{16Eh^3} \tag{3.8}$$

The maximum deflection w_0 occurs at the centre of the diaphragm and is given by:

$$w_0 = \frac{Pa^4}{64D} \tag{3.9}$$

From Equation 3.8, it is apparent that the displacement is proportional to the fourth power of the radius and inversely proportional to the cubic power of the thickness. For a clamped circular diaphragm, the effect of the variation in the diaphragm radius and thickness on the diaphragm displacement are shown in Figs. 3.2 and 3.3.

Fig. 3.2 shows the displacements of circular silicon diaphragms with a radius of R, 2R and 3R (where R = 50 μm). For all the diaphragms, a constant thickness of 2 μm was considered. An applied uniformly distributed pressure of 9 kPa was assumed in order to allow the maximum deflection to lie within the range allowed by small deflection theory. As illustrated in the figure, it can be seen that with the increase in radius, for the same applied pressure, there is an increase in deflection proportional to the fourth power of the radius.

Fig. 3.3 shows the variation in displacements of circular silicon diaphragms of varying thickness H, 2H and 3H (where H = 1 μm). A radius of 100 μm was assumed for all cases. An uniformly distributed pressure of 1 kPa was assumed in order to allow the the maximum deflection to lie within the range allowed by small deflection theory. As illustrated in the figure, with an increase in applied pressure, there is a decrease in diaphragm deflection

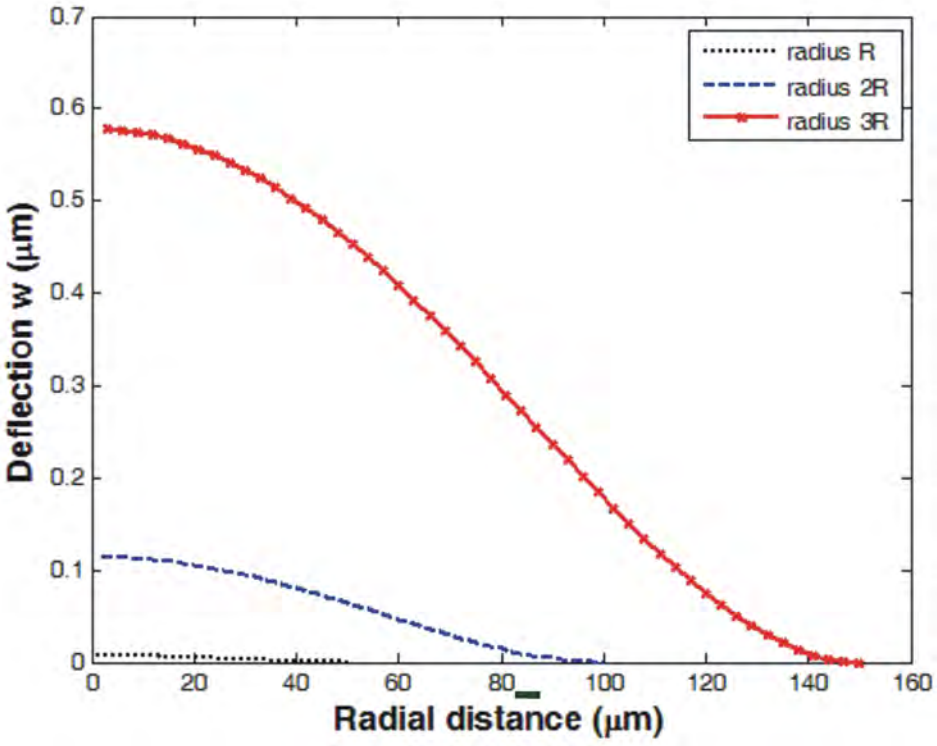

FIGURE 3.2: Analytical simulation results showing displacement of clamped circular silicon diaphragms having radii R, 2R and 3R (where R = 50 μm) each having a thickness of 2 μm under an applied uniform pressure of 9 kPa

inversely proportional to the third power of the thickness.

The total capacitance of a sensor with a clamped circular diaphragm subjected to a uniformly distributed pressure P is given by:

$$C = 2\pi\varepsilon_0\varepsilon_r \int_0^a \frac{rdr}{d_0 - w(r)} \tag{3.10}$$

Substituting for *w(r)* (from Equation 3.8), the capacitance as a function of pressure for a clamped circular diaphragm is given by:

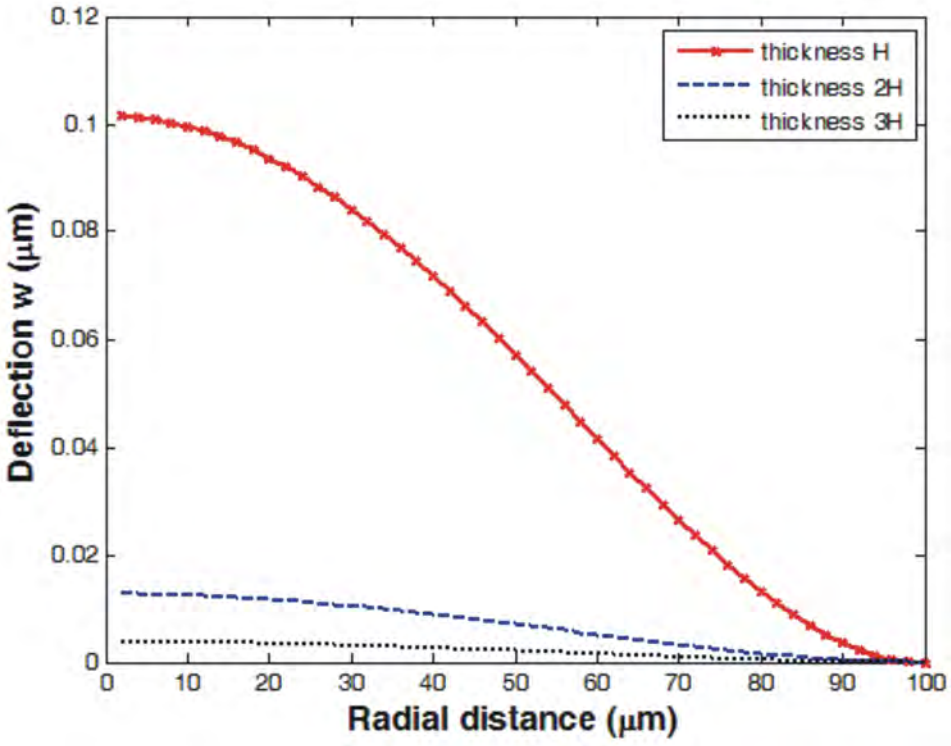

FIGURE 3.3: Analytical simulation results showing displacement of a clamped circular silicon diaphragms (with radius 100 μm) having thickness H, 2H and 3H (where H = 1 μm) under an applied uniform pressure of 1 kPa)

$$C(P) = 2\pi\varepsilon_0\varepsilon_r \int_0^a \frac{r\,dr}{d_0 - \frac{P}{64D}(a^2 - r^2)^2} \tag{3.11}$$

This can be simplified to:

$$C(P) = 8\pi\varepsilon_0\varepsilon_r \sqrt{\frac{D}{d_0 P}} \tanh^{-1}\left(\frac{a^2}{8}\sqrt{\frac{P}{d_0 D}}\right) \tag{3.12}$$

The capacitance thus varies as a non linear function of applied pressure. This is seen in Fig. 3.4 which shows the calculated capacitance change ΔC for a sensor with a clamped circular silicon diaphragm having a diameter of 200 μm, a thickness of 2 μm, and separated from a bottom electrode by an air gap of 2 μm.

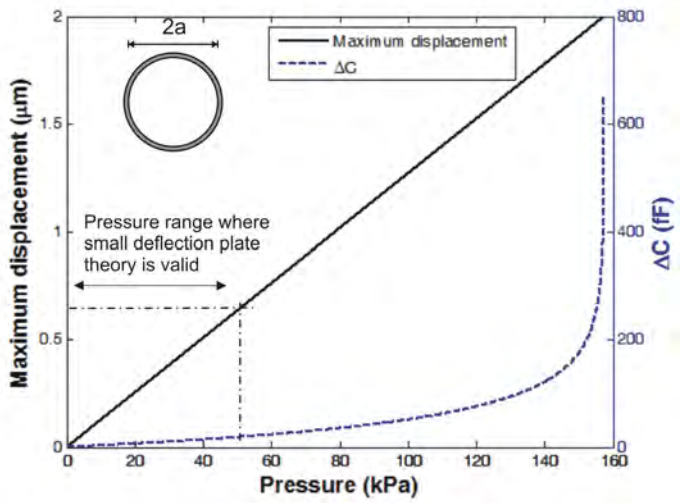

FIGURE 3.4: Capacitance change (ΔC) with applied pressure for a 200 μm ϕ clamped circular silicon diaphragm (assuming small deflection theory)

Thus, by varying the plate thickness, radius and gap between electrodes, the sensitivity and range of a capacitive sensor can be adjusted accordingly to meet the required device specification. The effect of variation in these three parameters on the response of a capacitive sensor can be seen in Fig. 3.5. It is seen that varying each of the parameters causes a change in the sensitivity and range of the sensor with the greatest influence made by radius of the diaphragm.

The working pressure range of capacitive sensors is defined by the pressure at which the diaphragm begins to touch the bottom electrode/substrate (touch-point pressure) or the pressure at which the diaphragm yields, whichever occurs earlier. As previously described, for the case of clamped circular diaphragms, maximum deflection occurs at the centre of the diaphragm. Thus the touch-point pressure P_{max} can be determined by allowing the maximum deflection w_{max} to equal the initial gap between the plates (d_0) in Equation 3.9.

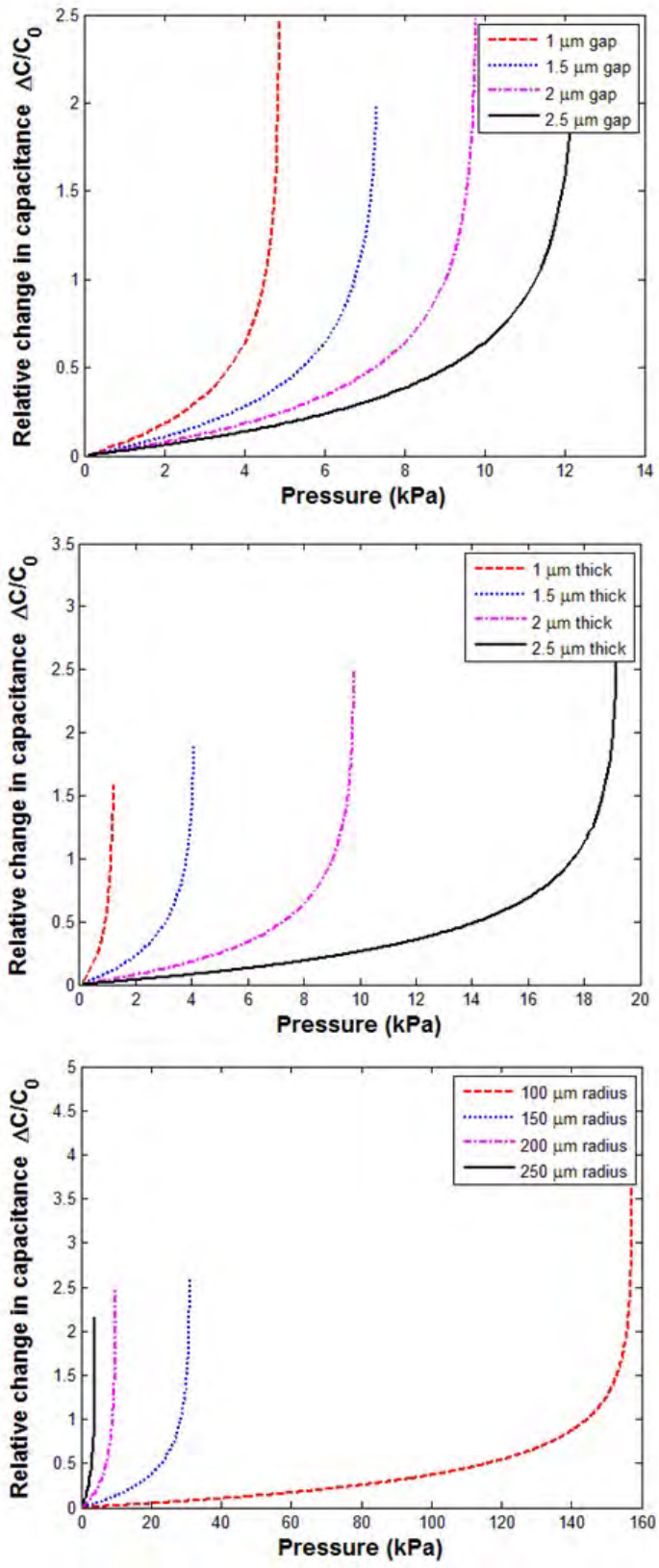

FIGURE 3.5: Effect of varying the gap, thickness and radius on sensor response

Substituting d_0 in Equation 3.9 gives:

$$P_{max} = \frac{64Dd_0}{a^4} \tag{3.13}$$

When designing sensor diaphragms, it is important to ensure that the value P_{max} does not exceed the yield strength of the diaphragm material.

Clamped square diaphragms

Square and rectangular diaphragms are generally easier to fabricate and also show a higher yield in comparison to circular diaphragms [105]. For this reason, such diaphragms have been most commonly employed in the design of MEMS pressure sensors. The analytical calculations for the displacement of square and rectangular clamped diaphragms are complex and rely only on approximate solutions. Numerical methods such as finite element analysis (discussed later) and finite difference techniques are commonly used as they provide more accurate solutions.

The approximate solution for diaphragm deflection for the case of square diaphragms with side length 2a is given by [106]:

$$w(x,y) = \frac{Pa^4}{47D}\left(1 - \frac{x^2}{a^2}\right)^2\left(1 - \frac{y^2}{a^2}\right)^2 \tag{3.14}$$

Thus, maximum deflection reads:

$$w(x,y) = \frac{Pa^4}{47D} \tag{3.15}$$

This is larger than the deflection of a circular diaphragm of diameter 2a (Equation 3.9).

To calculate the total change in capacitance when a uniform load is applied to the sensing diaphragm, Equation 3.14 can be substituted into Equation 3.3:

$$C(P)_{square} = 4\varepsilon_0\varepsilon_r \int_0^a \int_0^a \frac{1}{d_0 - \frac{Pa^4}{47D}\left(1-\frac{x^2}{a^2}\right)^2\left(1-\frac{y^2}{a^2}\right)^2} dxdy \tag{3.16}$$

Using Matlab, Equation 3.16 was solved and the capacitance change as a function of applied pressure for a clamped square Si diaphragm of side length 200 μm and thickness 2 μm was estimated. An electrode gap spacing of 2 μm was assumed. The results of the simulation are shown in Fig. 3.6. They show the non-linear sensor response to applied pressure.

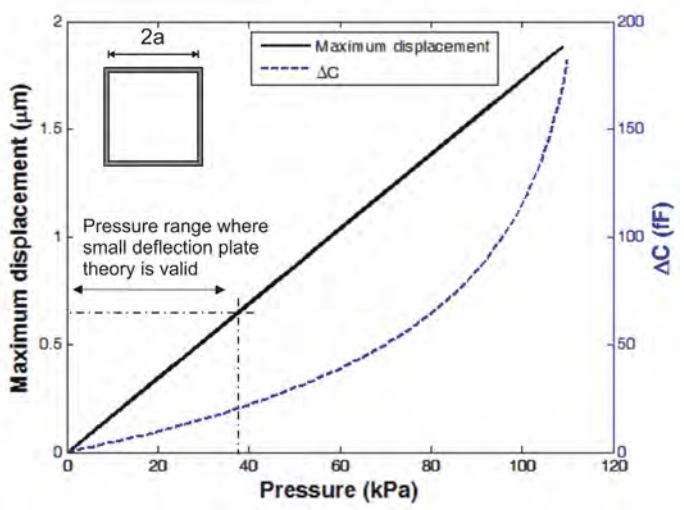

FIGURE 3.6: Capacitance change (ΔC) with applied pressure for a clamped square silicon diaphragm having a side length of 200 μm, thickness of 2 μm and separated from a bottom electrode by a distance of of 2μm (assuming small deflection theory)

Clamped rectangular diaphragm

For rectangular diaphragms with small deflections and rigidly clamped edges, the characteristic equation for diaphragm deflection can be approximated by [106]:

$$w(x,y) = \frac{P}{2Eh^3}\left(1-\nu^2\right)\frac{\left(a^2-x^2\right)^2\left(b^2-y^2\right)^2}{a^4+b^4} \tag{3.17}$$

where 2a is the width and 2b the length of the diaphragm.

Estimation of the capacitance change as a function of pressure is given by substituting Equation 3.17 into Equation 3.3:

$$C(P)_{rectangle} = 4\varepsilon_0\varepsilon_r \int_0^a \int_0^b \frac{1}{d_0 - \frac{P}{2Eh^3}\left(1-\nu^2\right)\frac{\left(a^2-x^2\right)^2\left(b^2-y^2\right)^2}{a^4+b^4}} dxdy \tag{3.18}$$

Using Matlab, Equation 3.18 was solved and the capacitance change as a function of applied pressure for a clamped rectangular Si diaphragm with a width of 200 μm and a length of 300 μm was estimated. As in the previous case, a diaphragm thickness of 2 μm and an electrode spacing of 2μm was assumed. Results are shown in Fig. 3.7.

Fixed-fixed rectangular/square diaphragm

For the case of a plate fixed on two opposite ends, beam equations were used as a preliminary approximation. The equation for deflection *w(x)* of a fixed-fixed beam as a function of the position (x) along its length is derived from Euler-Bernoulli beam theory and is given by [107]:

$$w(x) = \frac{Pl^4}{2Eh^3}\left(\frac{x^2}{l^2} - \frac{2x^3}{l^3} + \frac{x^4}{l^4}\right) \tag{3.19}$$

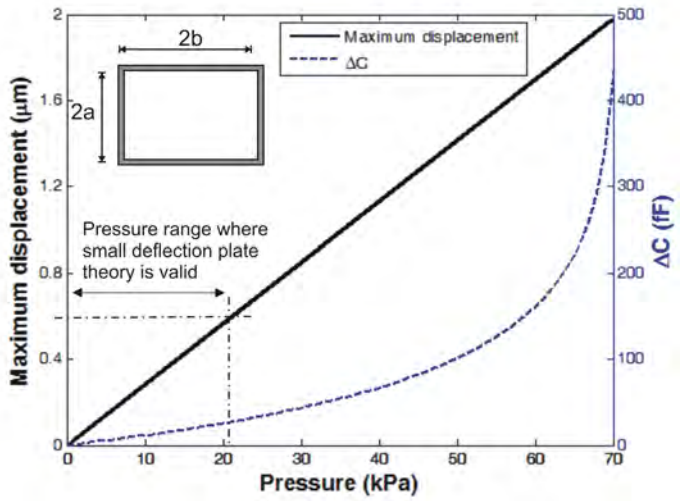

FIGURE 3.7: Capacitance change (ΔC) with applied pressure for a clamped rectangular silicon diaphragm having dimensions 300 $\times$ 200 μm^2, thickness of 2 μm and separated from a bottom electrode by a distance of of 2μm (assuming small deflection theory)

Thus, the capacitance can be calculated from:

$$C(P) = b\varepsilon_0\varepsilon_r \left(\frac{1}{d_0 - \frac{Pl^4}{2Eh^3} \int_0^l \frac{x^2}{l^2} - \frac{2x^3}{l^3} + \frac{x^4}{l^4} dx} \right) \tag{3.20}$$

For the case of a 200 μm long and 2 μm thick beam separated by a distance of 2 μm from a bottom electrode, the capacitance change as a function of applied pressure is shown in Fig. 3.8.

Comparison of diaphragm designs

To summarise the findings from the analytical simulations that have been carried out, a comparison of the predicted behaviours of capacitive sensors incorporating different silicon diaphragm designs is shown in Fig. 3.9. It represents the relative change in capacitance with applied pressure for the following cases:

- clamped circular diaphragm of diameter 200 μm

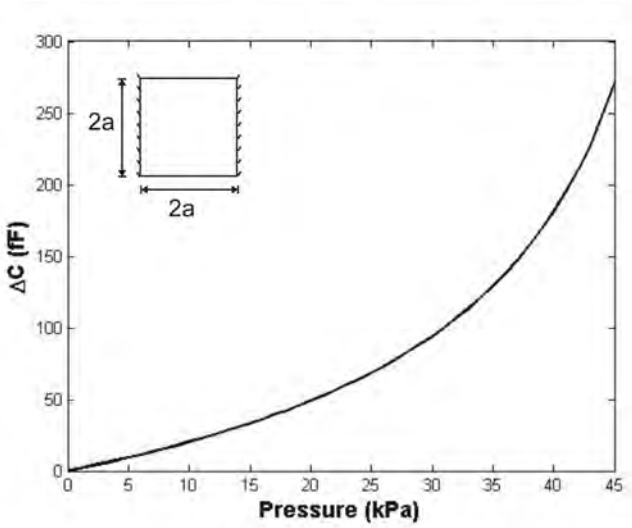

FIGURE 3.8: Capacitance change (ΔC) with applied pressure for a fixed-fixed silicon diaphragm having dimensions $200 \times 200 \times 2$ μm^3, thickness of 2 μm and separated from a bottom electrode by a distance of of 2μm

- clamped square diaphragm of side length 200 μm
- clamped rectangular diaphragm of length 200 μm and width 300 μm
- fixed-fixed rectangular diaphragm of length 200 μm

In all cases, a thickness of 2 μm and an electrode spacing of 2 μm was considered. Only the responses corresponding to the linear regions of response (corresponding to a deflection between 0 and 30% of the diaphragm thickness) are shown.

The sensitivity of a capacitive sensor describes how much its output varies with respect to a given variation in the stimulus (or sensor environment) [108]. Thus it reflects the sensor's capability of transducing the input signal (mechanical stimulus) into an electrical output [109]. For the diaphragms assessed, the fixed-fixed diaphragm has greater sensitivity (i.e. change in capacitance/pressure). However, a compromise exists between sensitivity and the overall pressure range of devices.

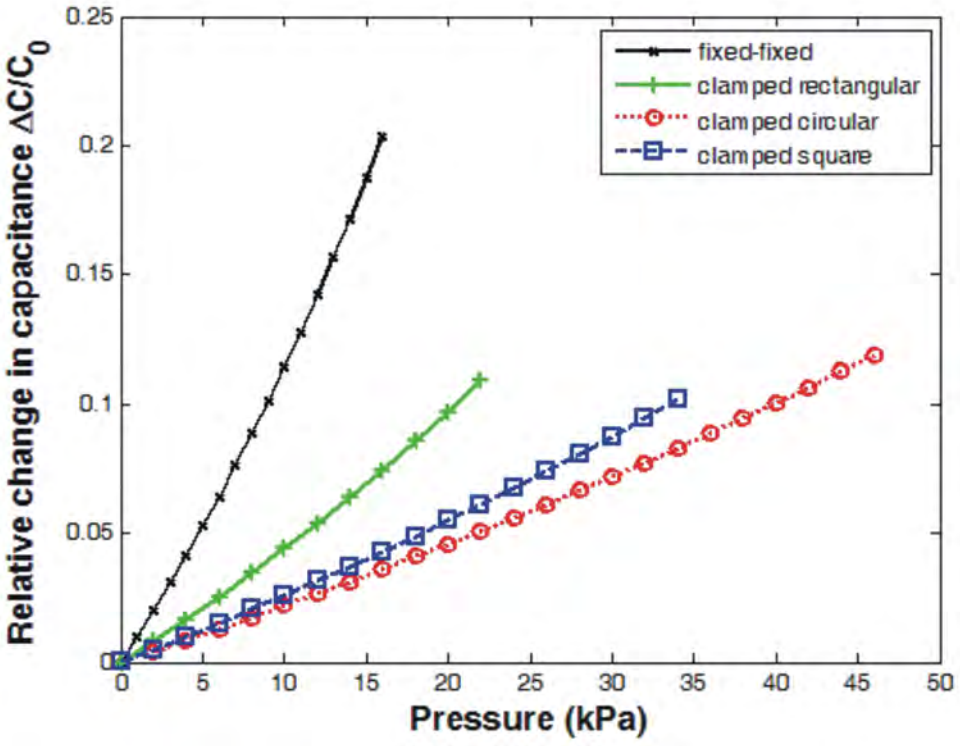

FIGURE 3.9: Capacitance change (ΔC) with applied pressure for a fixed-fixed 200μm diaphragm, clamped rectangular diaphragm having dimensions 300 $\times$ 200 μm^2 , square diaphragm having a side length of 200 μm and a circular diaphragm of diameter 200 μm (assuming small deflection theory). For all cases, a diaphragm thickness of 2 μm and an electrode spacing of 2 μm was used

3.3.2 Finite Element Analysis

In section 3.3.1, diaphragm deflection was assessed using small deflection theory of plates. However in practice, sensor diaphragms deflect by a distance greater than that allowed for by small deflection theory. In such cases, Finite Element Analysis (FEA), a computer based numerical analysis method can be used. FEA serves as a valuable design tool when developing sensor diaphragms since it gives more accurate results compared to analytical solutions, especially when considering complex geometries and boundary conditions such as those encountered in MEMS devices [110].

In FEA, the solid structure under examination is divided into a finite number of subdivisions of special shapes (called elements) that are interconnected at the corners or on the edges of elements (called nodes). The governing physical equations are solved for each of these elements instead of the whole structure. The solutions derived at the element level are then assembled to get the corresponding solution for the whole structure.

In this work, the commercial FEA software package Comsol Multiphysics was used to numerically simulate the electromechanical behaviour of the sensing device. This software includes a dedicated MEMS module which allows the analysis of electro-thermal-chemical-mechanical behaviors of MEMS components. Using this module, the mechanical behaviour of different designs of sensor diaphragms and the relationships between the applied pressure, mechanical deflection and capacitance were analysed.

The simulation process involves the following main steps:

- Generation of a geometrical model of the structure
- Specification of material parameters, initial and boundary conditions
- Creation of a mesh of elements (specifying desirable density of nodes and elements)
- Solving the model
- Post processing the results to analyse desired parameters and present graphic illustrations of the results

In order to assess the validity of the FEA models, results of the analytical solutions (previously described) and FEA solutions for a capacitive sensor incorporating a clamped rectangular diaphragm were compared. The geometry of modelled sensor and the displacement profile as estimated from FEA is shown in Fig. 3.10.

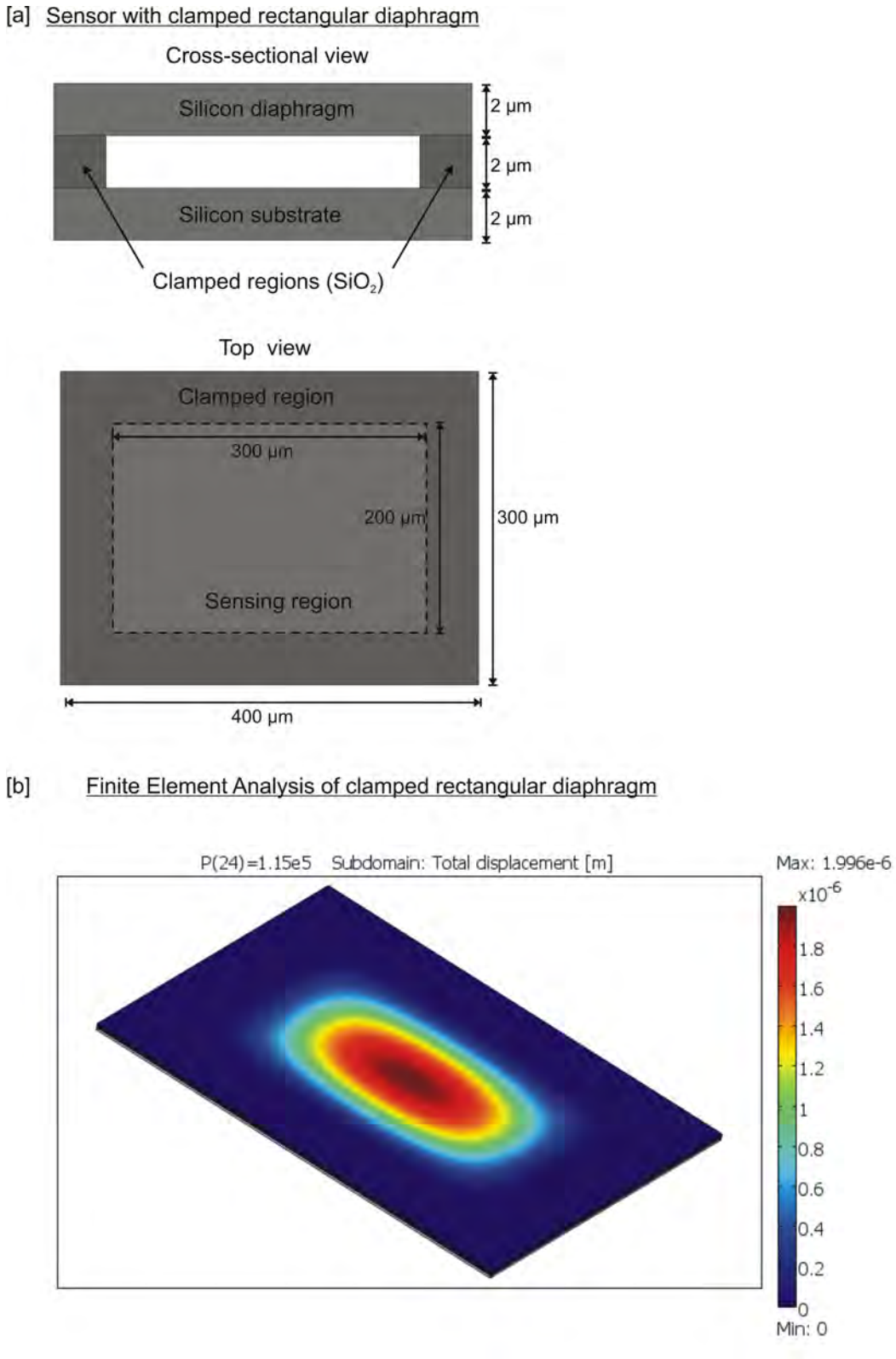

FIGURE 3.10: [a] Cross section and top view schematic of a sensor with a clamped rectangular diaphragm, [b] FEA results showing displacement of the sensor diaphragm to an applied pressure of 115 kPa

Fig. 3.11 shows a comparison of the analytically and numerically estimated values of maximum diaphragm displacement and total capacitance change as a result of uniformly applied pressures of 0 - 115 kPa. The analytical expressions assume small deflection theory which is applicable for maximum deflections up to 30% of the thickness of the plate. The results in Fig. 3.11 show agreement of analytically calculated and numerically predicted values of diaphragm deflection and change in capacitance at lower applied pressures (at a range allowed for by small deflection theory). Beyond this range, the analytical model does not consider tensile forces acting on the diaphragm and therefore overestimates the deflection at a given pressure.

3.4 Sensor conception

The design of the sensors was based on the results from analysis of the performance of various sensing diaphragms and considering their potential fabrication techniques. As discussed in Section 2.3, the main requirements include:

- Decreased sizes of individual sensor units to allow a high density of elements per given area and decreased spacing between units to allow high spatial resolution. The overall device should be sufficiently compact to allow integration into an artificial finger.
- High sensitivity allowing detection of small fluctuations in applied pressures due to differences in surface texture.
- Sufficient operating range (pressure range over which a reliable sensor output can be attained).
- Easy fabrication methods, allowing high yield and low costs.

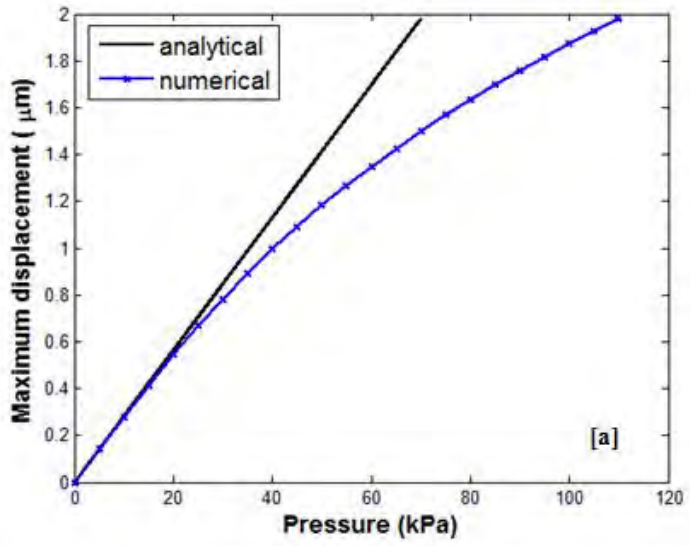

Capacitive sensor design parameters: length (b) = 300 μm, width (a) = 200 μm, thickness (h) = 2 μm, gap (d_0) = 2 μm

FIGURE 3.11: Comparison of numerical (FEA) and analytical solutions for a clamped rectangular beam. [a] Maximum displacement vs. applied pressure [b] Change in capacitance vs. applied pressure

The chosen dimensions of the sensor diaphragm are critical as they influence the performance characteristics of the device. In order to realise a biomimetic device design, the dimensions of each element had to be optimised to allow an innervation density similar to that of the mechanoreceptors of the finger tip. As discussed in Chapter 2, the merkel cells (SA I tactile units) that are responsible for coding surface spatial features have an oval shape measuring 10 - 15 μm in the long axis and are present in clusters with approximately ten merkel cells innervated by a single peripheral nerve fibre. The SA I afferents innervate the finger tip at a density of approximately 70 units/cm^2 and are spaced such that they allow a finger tip spatial resolution of 2 - 3 mm. The requirement for compact sizing of the sensing elements is in conflict with the performance requirements of the device in terms of sensitivity. As discussed in the previous section, trade-offs exist between diaphragm size and sensitivity and between sensitivity and working range. Devices with larger diaphragms have greater sensitivities but smaller working ranges. Conversely devices with smaller diaphragms have higher working ranges but lower sensitivities.

With the aforementioned considerations in mind, two diaphragm designs were selected for fabrication:

1. Design 1: Fixed-fixed square plate

2. Design 2: Fully clamped rectangular diaphragm

The characteristic features of each sensor design are given in Table 3.1. Square and rectangular diaphragms are relatively easier to fabricate compared with circular diaphragms. Further they have greater sensitivities compared to circular diaphragms with equivalent diameter and side length dimensions.

Design 1 (fixed-fixed plate) offers a greater sensitivity compared to other designs of comparable dimensions. In addition to the requirements mentioned previously, the chosen dimensions of the sensing diaphragm of Design 1 took into consideration mechanical stability related issues during the planned fabrication process (see Chapter 4). Preliminary fabrication experiments showed fixed-fixed plate devices to have a susceptibility to release related stiction. To prevent such occurrences and maximise fabrication yield, diaphragms with a square plate geometry (and therefore stiffer structures compared to fixed-fixed rectangular structures) having dimensions of 200 μm $\times$ 200 μm were designed.

The use of fully clamped diaphragms allows for devices with high sensitivity and larger operating range compared to the fixed-fixed plate configuration with comparable dimensions. Diaphragm dimensions of 300 μm $\times$ 200 μm were used in Design 2.

TABLE 3.1: Sensor design features

Property	Design 1	Design 2
Diaphragm material	silicon	silicon
Diaphragm dimensions	200 μm $\times$ 200 μm	300 μm $\times$ 200 μm
Overall plate dimensions	500 μm $\times$ 200 μm	500 μm $\times$ 400 μm
Diaphragm thickness	2 μm	2 μm
Capacitor plate separation	2 μm	2 μm
Edge conditions	fixed-fixed	clamped

The design of a single sensor unit for each design is shown in Fig. 3.12. Each unit consists of a sensing region, a wire bonding region and an interconnecting wire. The overall dimensions of the sensing region are extended to allow edge clamping regions (which are further detailed in Chapter 4). Etch holes with a radius of 5 μm were included within the sensing region and spaced 50 μm apart from each other. These are sacrificial etch holes that are incorporated into the sensor design to allow formation of the air gap during the fabrication

process, as discussed in Chapter 4. The size and spacing of these holes were selected based on preliminary wet etching experiments. The bond pads for wirebonding have dimensions of 300 μm $\times$ 300 μm. The sensing region and wire bond pads are separated by 140 μm $\times$ 1 mm long wires.

3.5 FEA simulation of sensor

3.5.1 Simulation of electromechanical behaviour

A 3D model of the sensor was constructed within the Comsol Multiphysics user interface. The model incorporated the following three principal subdomains:

- A 2 μm thick top Si plate that contained a pressure sensitive region consisting of a clamped rectangular Si diaphragm, dimensioned as given in Table 3.1. The diaphragm forms the top electrode of the capacitive sensor. Within the sensing area, an array of etch holes of radius 5 μm were incorporated.

- 2 μm thick supportive SiO_2 structures that provide the fixed edge boundary conditions for the sensing diaphragm

- Si substrate that acts as a lower electrode for the capacitive sensor.

The model assumed Si to be an isotropic material. Material properties used in the simulation are given in Table 3.2:

Fixed constraints or boundary conditions were applied to the $Si0_2$ and Si substrate as no deformation is assumed to occur in these support structures. A uniformly distributed pressure was applied to the top Si plate. The meshing of the geometries was carried out using

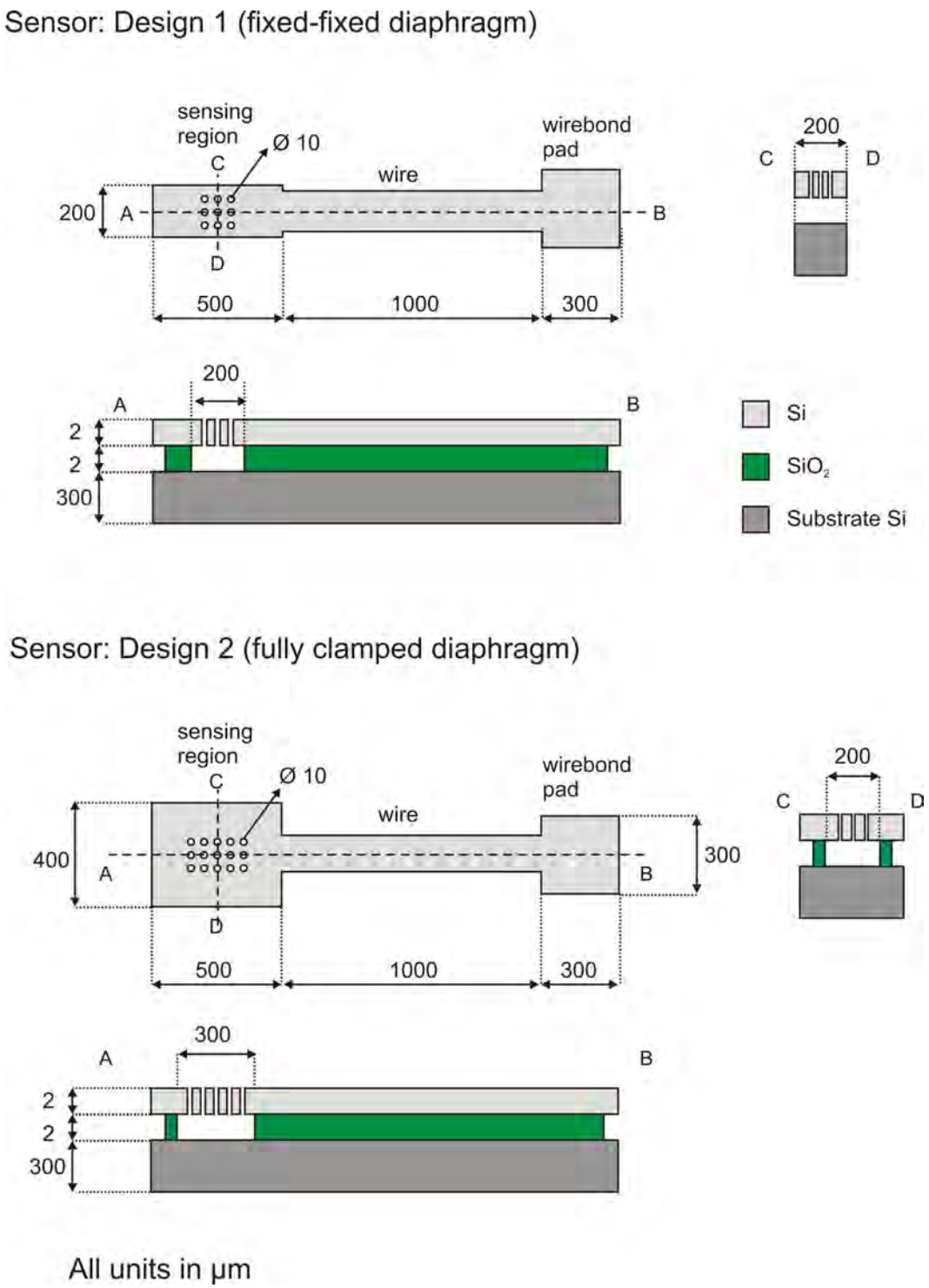

FIGURE 3.12: Schematic of sensor designs 1 and 2

TABLE 3.2: Material properties used in FEA simulation

Material	Young's modulus (E) (GPa)	Poisson's ratio (ν)	Density (kg/m^3)
Silicon	170 GPa	0.28	2329
Silicon dioxide	70 GPa	0.17	2200

tetrahedral elements. A higher density of elements was used for the top Si plate (19083) in comparison to the SiO_2 and substrate subdomains (1970 and 1912 respectively). To ensure the use of the correct mesh density, a mesh convergence study was carried out. Results of the mesh convergence study for Design 1 are shown in Fig. 3.13. Here, a uniformly applied pressure of 10 kPa was assumed and maximum displacement of the diaphragm was predicted under the various mesh conditions. Fig. 3.13 shows convergence of results with increasing mesh density.

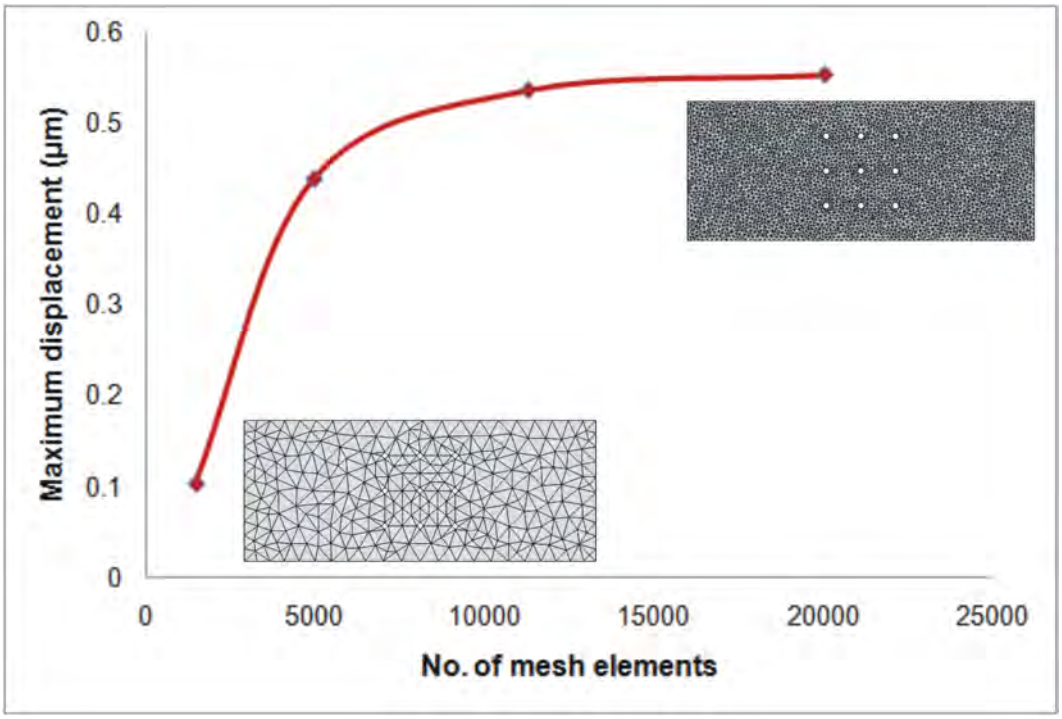

FIGURE 3.13: Mesh density vs. FEA simulated results for maximum displacement (for the case of a uniformly applied pressure of 10 kPa

A parametric analysis was carried out to assess the mechanical response over a range of pressures. Fig. 3.14 shows the displacement profiles of both sensor designs and illustrates the effect of different boundary conditions on the shape of diaphragm deformation. Fig. 3.15 shows the von Mises stress distribution on the top plate of the sensor subjected to a uniformly distributed pressure corresponding to the touch-point pressure. The von Mises stress is generally used as the representative stress in multiaxial stress situations. Its values are compared with the yield stress for plastic yielding and to ultimate tensile stress for the prediction of rupture of the structure [111]. The regions of maximum stress are found to be at the corners of clamping regions for Design 1 and at the centres of clamped ends (along the diaphragm length) for Design 2.

The von Mises stress is calculated from the following equation:

$$\sigma = \frac{1}{\sqrt{2}}\sqrt{(\sigma_{xx} - \sigma_{yy})^2 + (\sigma_{xx} - \sigma_{zz})^2 + (\sigma_{yy} - \sigma_{zz})^2 + 6(\sigma_{xy}^2 + \sigma_{yz}^2 + \sigma_{xz}^2)} \qquad (3.21)$$

where σ_{xx}, σ_{yy}, σ_{zz} are respective stress components along the x, y and z axis and σ_{xy}, σ_{yz}, σ_{xz} are the shear stress components in the element.

A summary of the main results from the numerical simulations are given in Table 3.3. The maximum stress (generated at a pressure corresponding to the upper limit of the sensor operating range) for both sensor designs was found to be well within the limits of yield strength for Si, which is 7 GPa [102].

To calculate the total capacitance of the sensor, the program integrates infinitesimal capacitance contributions over the surface of the electrode boundary according to the following equation:

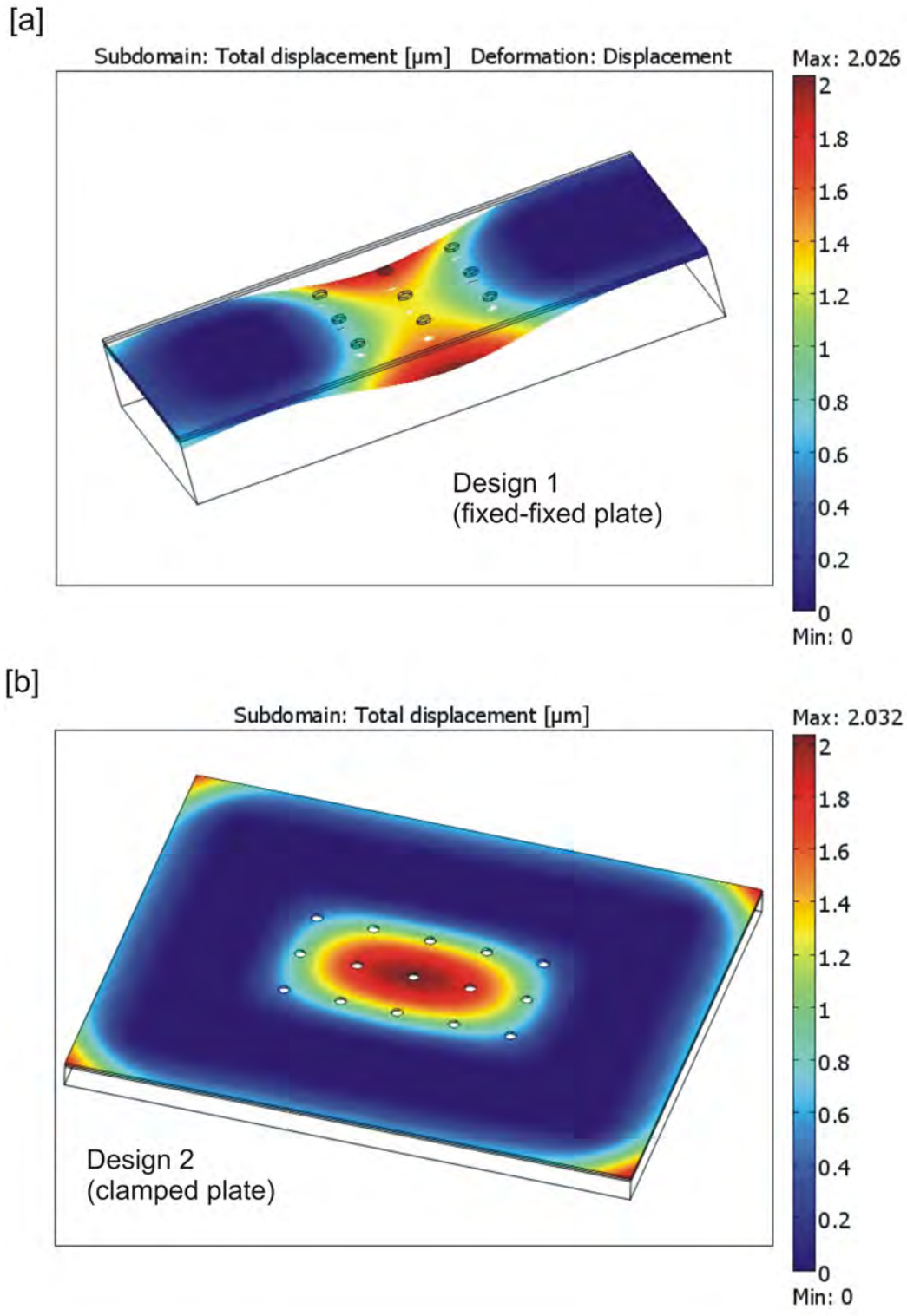

FIGURE 3.14: Results of the FEA simulation showing the displacement profile of sensing diaphragms subjected to uniformly distributed pressures corresponding to their touch-point pressures (48 kPa for Design 1 and 120 kPa for Design 2)

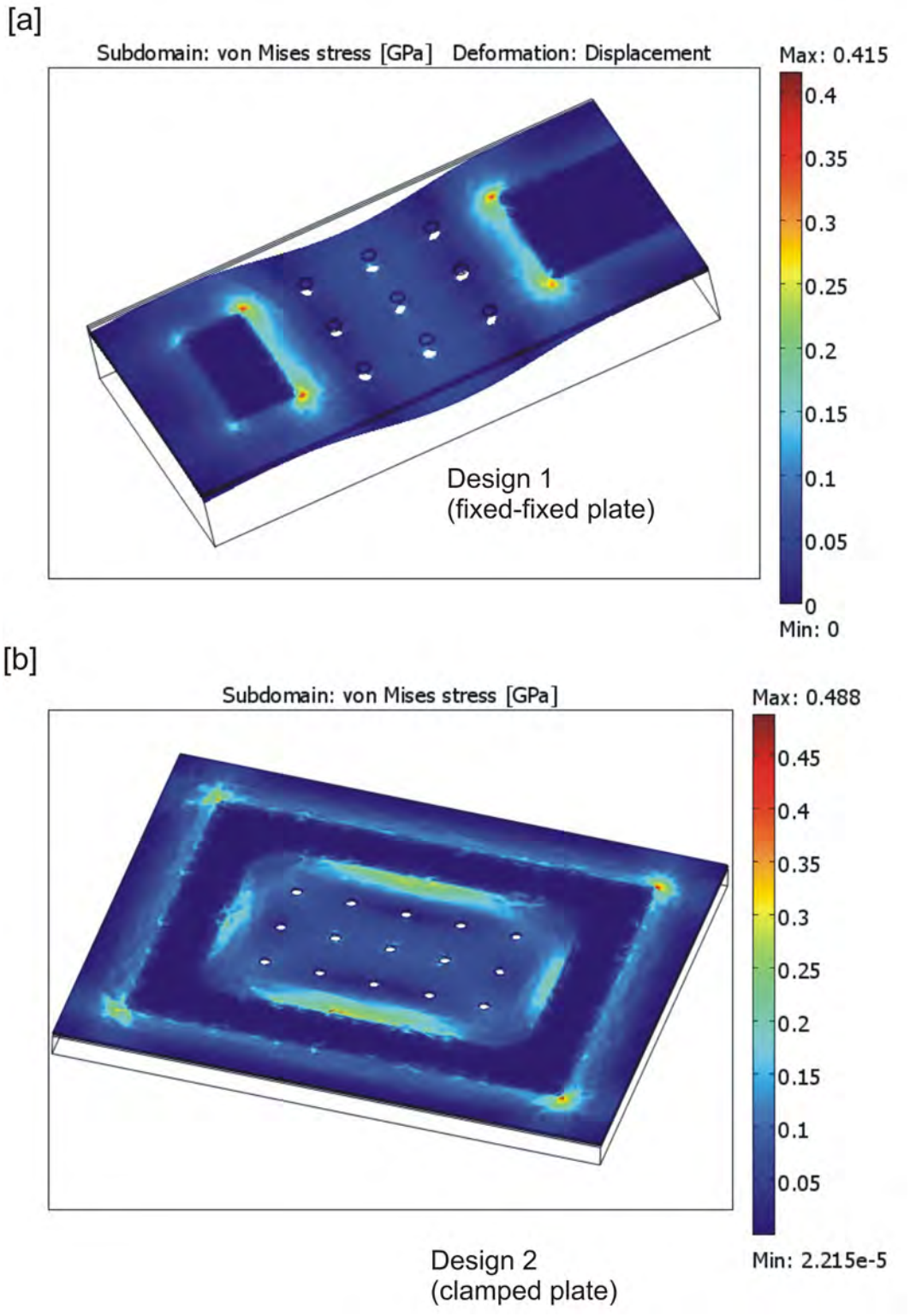

FIGURE 3.15: Results of the FEA simulation showing the von Mises stress generated on application of uniformly distributed pressure corresponding to their touch-point pressures (48 kPa for Design 1 and 120 kPa for Design 2)

TABLE 3.3: Summary of FEA simulation results

Property	Design 1 fixed-fixed	Design 2 fully clamped
Δ C at deflection *w*= 1 μm (50% d_0) (fF)	125	60
Δ C at deflection *w*= 1.98 μm (98% d_0) (fF)	300	350
Touch point pressure (kPa)	48	120
Stress at touch point pressure (σ_{max})	0.43 GPa	0.49 GPa
Resonant frequency	587 kHz	418.7 kHz

$$C = \varepsilon_0 \varepsilon_r \int \frac{1}{h} dA \tag{3.22}$$

where *h* is the local distance across the capacitor.

Therewith the expected change in capacitance with applied pressure was numerically estimated. The results for both sensor designs are shown in Fig. 3.16. Design 1 (fixed-fixed plate) is seen to have a greater sensitivity compared to Design 2 (clamped plate) with the latter having greater than twice the operating range. Touch point pressures of 48 kPa and 120 kPa equating to forces of 4.8 mN and 24 mN were estimated for Design 1 and Design 2 respectively. Assuming a force damping factor of 100 by subsequently applied packaging material (further discussed in Chapter 5), the devices should be able to cope with the range of forces used during surface exploration tasks.

3.5.2 Effect of sacrificial etch holes

As previously mentioned, sacrificial etch holes were introduced into the sensing diaphragm. To investigate the influence of these holes on sensor performance, FE models of the sensor comprising diaphragms with and without holes were compared. The results depicted in Fig. 3.17 show that the presence of the etch holes affects the absolute change in capacitance by 7

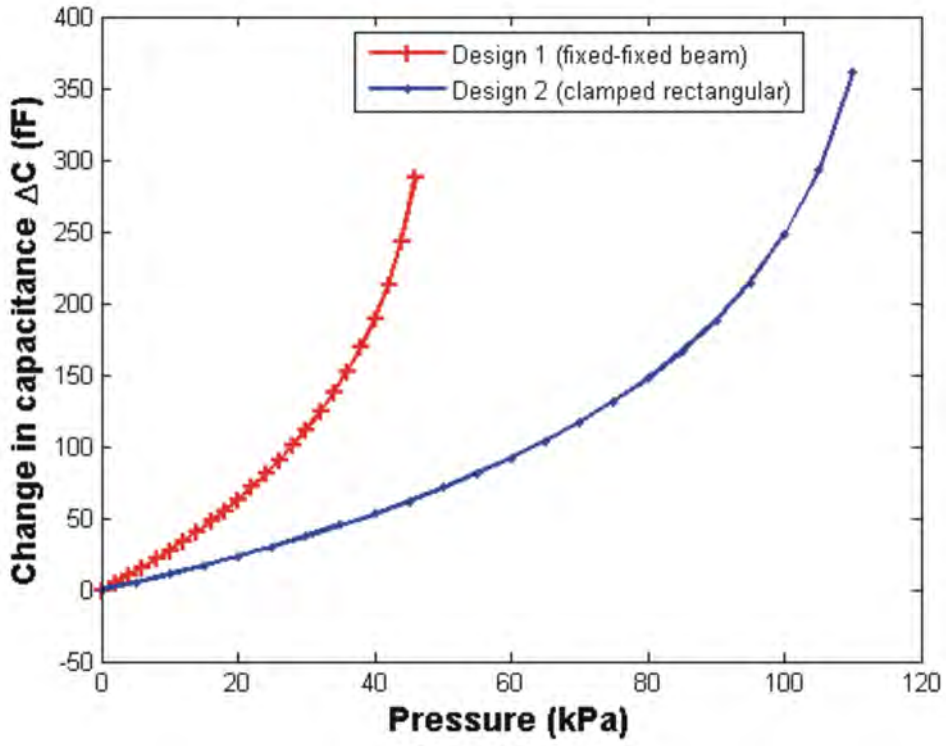

FIGURE 3.16: Results of FEA showing capacitance change as a function of applied pressure

to 17% over the entire pressure range. The sensitivity, however, is not significantly affected by this change.

3.5.3 Electrostatic pull-in forces

In order to measure the output from a capacitive sensor, a sensing voltage is applied. This leads to the presence of electrostatic forces that tend to pull the two plates of the sensor together [109]. Diaphragm collapse can occur when above a threshold voltage, known as the pull-in voltage, restoring spring forces suspending the sensor diaphragm are unable to sustain the attractive electrostatic forces.

The electrostatic pull-in forces thus introduce an offset error. When interpreting outputs from the sensor, it is important to distinguish between the response that is caused due to an

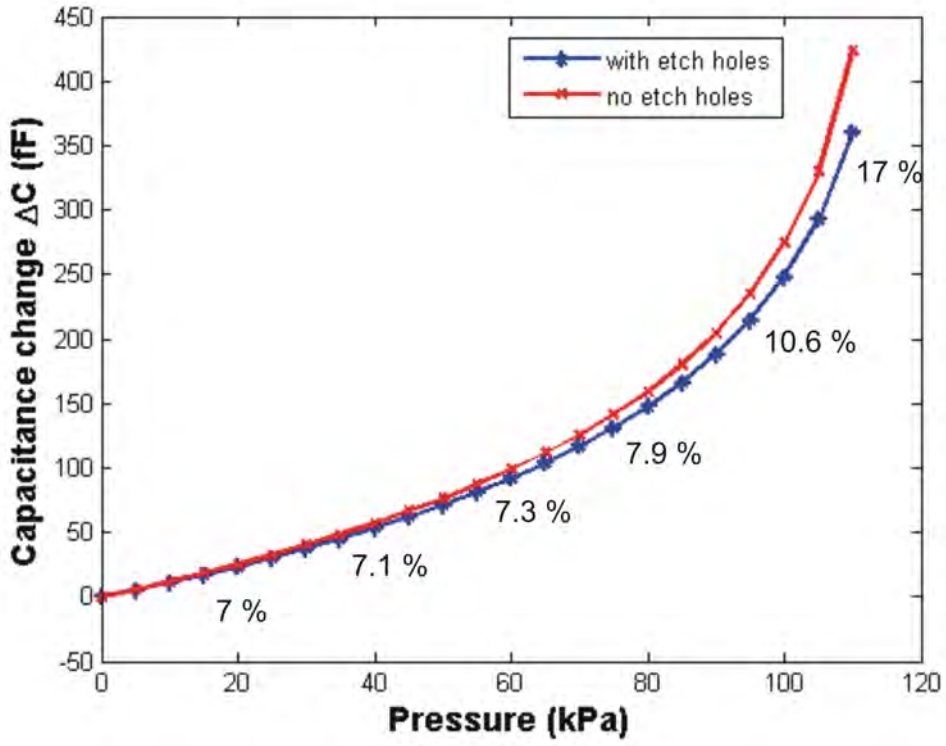

FIGURE 3.17: FEA simulation results showing the responses of a fully clamped rectangular diaphragm with and without etch holes and the the relative percentage change (values quoted) in sensor response due to presence of etch holes

applied pressure and that as a result of influence from the measurement circuit.

Hence, during the sensor design process, the influence of applied voltages on diaphragm deflection was predicted using FEA. Design 2 (fixed-fixed plate) was simulated to estimate a worst case scenario, as this diaphragm has a lower stiffness as compared to the two presented sensor designs and is therefore influenced by the electrostatic forces to a greater extent. Simulations were carried out using the Electrostatic (AC/DC) and moving mesh (ALE) modules. Fig. 3.18 shows the results of the numerical simulation of the sensor for applied voltages from 1 - 5 V and no applied pressure. The upper value of 5 V was chosen as it was the highest possible operating voltage of the measurement circuit that was used. Maximum deflection under these conditions are in the range of nanometers and therewith negligibly small

and well below the resolution of the measurement system (Section 3.6.3).

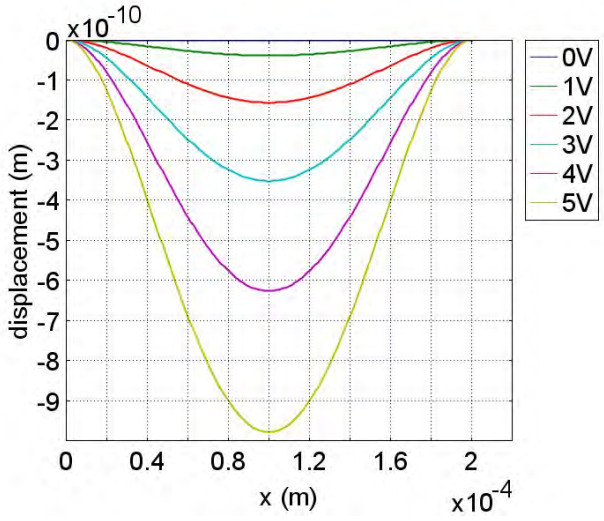

FIGURE 3.18: Displacement of the fixed-fixed plate as a function of position along the plate length and applied voltage

Simulations were also carried out to assess the combined influence of applied pressure and an applied voltage of 5 V. The results, showing the effect of applied voltage on the maximum diaphragm displacement under the influence of uniformly distributed pressures (10 - 50 kPa) are presented in Fig. 3.19. The influence of electrostatic forces on the diaphragm displacement increases as a function of applied pressure. At a pressure corresponding to 98% d_0, a predicted additional displacement is introduced, caused by the effects of electrostatic forces.

3.6 Implementation of sensor arrays

On contact with a surface, mechanical stimuli are applied to tactile sensors through surface features that are present at the contact interface of the sensor and surface. Tactile information on the area of contact can be obtained by the implementation of a number of sensor units in

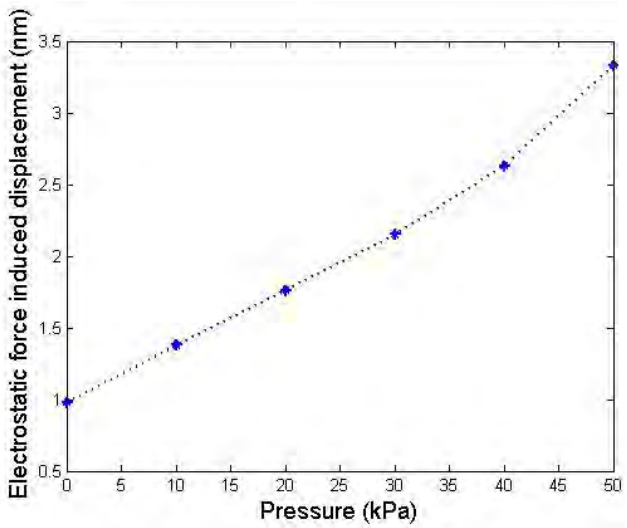

FIGURE 3.19: Influence of the application of 5 V across the sensor plates of design 2, subjected to varying magnitudes of uniformly distributed pressures

the form of arrays so that combined data from the units can be used to estimate the profile of features of the contacting body/surface. The responses of single sensors to mechanical stimulus are expected to vary based on stimulus magnitude and location. Two modes of operation are suggested for determined surface characteristics; these are static and dynamic touch. Where the spacings of surface features is greater than the pitch between sensing elements in an array, detection of surface profile is possible using 'static touch'. However, when surface features are spaced at distances lower than the pitch (as in the case of fine textures), a dynamic touch protocol can be employed. This involves lateral displacement of the sensor array across the surface to be evaluated and assessing the frequency components of sensor outputs. Thus, a combined spatio-temporal coding mechanism can be employed to characterise a contacting surface.

The above approach bears resemblance to texture perception mechanisms employed by humans where the responses of a population of mechanoreceptors are used for making judgements on the perception of texture [112, 113]. Some authors propose a duplex mechanism

of neural coding for texture perception; i.e. a vibrotactile mechanism accounting for the perceived roughness of fine textures and a spatial coding mechanism for perception of coarse textures [57]. Other authors suggest a unified paradigm via the spatiotemporal modulation of the neural activity of SAI afferents [58]. However, an established finding is the enhanced discrimination sensitivity obtained as a consequence of relative motion between the finger and the surface for which reason, when detecting textures, humans tend to slide their finger over the surface of interest. This relative motion, is hypothesised to be a requirement for the perception of fine textures [60].

3.6.1 Layout of sensor array

A linear array of 4 sensors was implemented to demonstrate proof of principle for use of the array for coding of surface features. In principle, a two dimensional array can be easily expanded with no significant demands on fabrication processing techniques.

Four sensor units were placed 150 μm apart from each other to form a linear array. Although a closest possible arrangement of the units is favourable to form high density arrays, consideration was also given to undercutting of the oxide supportive structures in the fabrication process. Fig.3.20 shows the layout of the sensor array. The pitch between elements depends on the width of the sensing plate region and is therefore 370 μm for arrays implementing Design 1 sensors and 570 μm for arrays implementing Design 2 sensors.

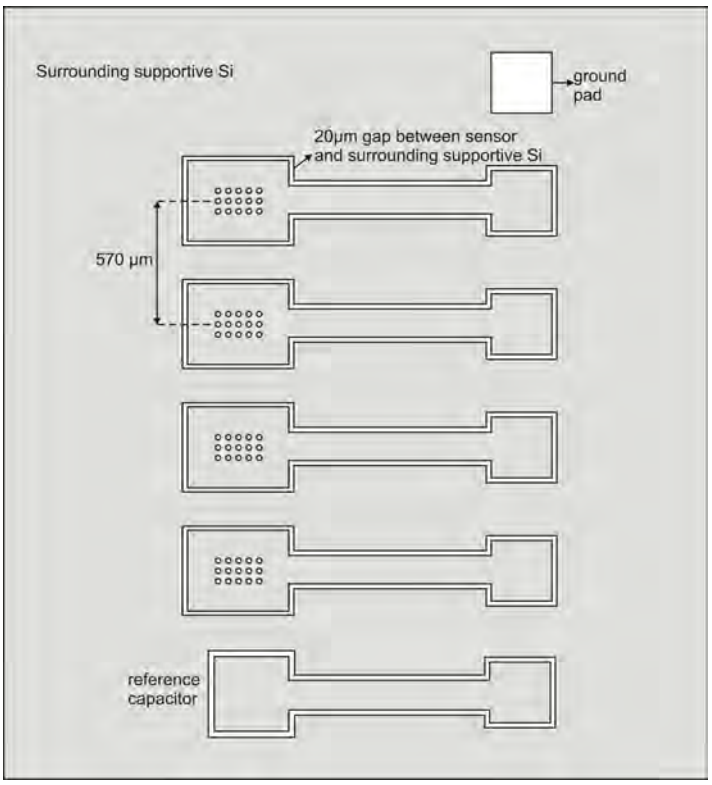

FIGURE 3.20: Schematic of sensor array showing 1 x 4 linear array of sensor units and a reference capacitor (see Section 3.6.2)

3.6.2 Reference capacitors

Fig. 3.20 shows the inclusion of reference capacitors in the sensing device. These were included in close proximity to the individual sensors and designed to be insensitive to applied pressure. The designs of reference capacitors for both sensor designs are shown in Fig. 3.21. They consist of two silicon plates that are separated by an oxide dielectric. The dimensions of these devices were calculated so that their capacitance would equal that of the corresponding sensor at zero applied pressure. The presence of reference capacitors allowed the measurement of a differential response and therefore eliminating the effects of parasitic capacitance.

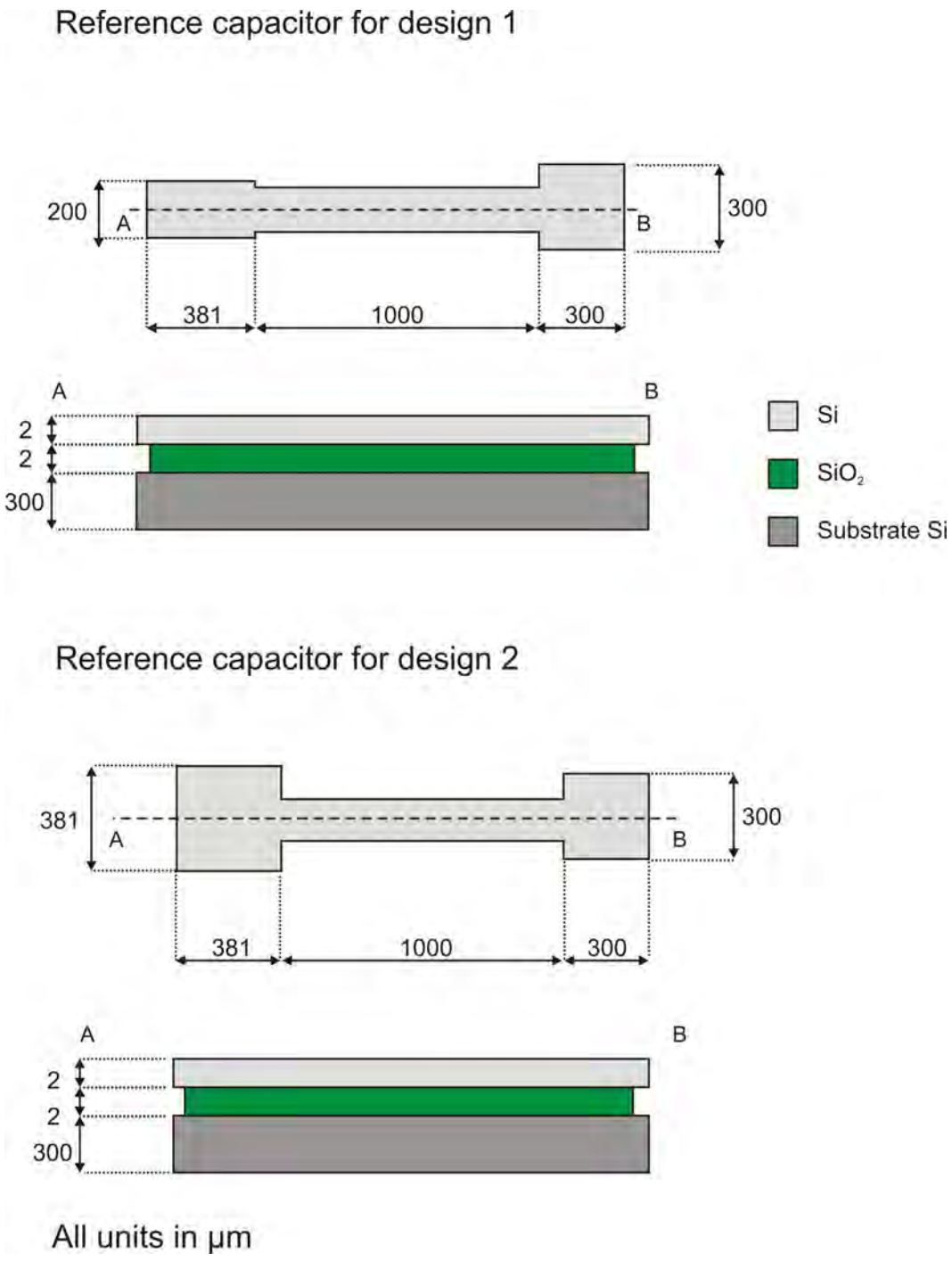

FIGURE 3.21: Design of reference capacitors for sensor designs 1 and 2

3.6.3 Design of signal acquisition electronics

The results from FEA simulation were used to plan the design of the capacitance acquisition electronics system. The readout electronics for the tactile sensor array was developed by the ARTS Lab, Superiore Sant'Anna, Pontedera, PI 56025 Italy.

The circuit encompassed high resolution capacitance-to-digital converters (AD7747, Analog Devices) and was implemented on a Printed Circuit Board (PCB) (Fig. 3.22). The circuit diagram is included in Appendix A. The chosen converters have a nominal resolution down to 20 aF and an accuracy of 10 fF. The converter generates a square-wave excitation signal on the sensor capacitance during the conversion and continuously samples the charge going through the capacitor. As reference capacitors were implemented in the device, a differential capacitive readout was used. This allowed elimination of drift and common mode variations due to proximity and parasitic capacitance coupling between the sensor and probe. Data from the converters was acquired with a soft-core processor (NiosII, Altera) instantiated onboard a FPGA (CycloneII, Altera) by means of I2C communication and then transmitted to a PC (running a Graphical User Interface implemented in Labwindows/CVI) by means of Ethernet communication. The devices were configured to work at an update rate of 45 Hz (11.25 Hz each channel). A schematic of the signal acquisition system is shown in Fig. 3.23.

3.7 Conclusions

For the design of the MEMS tactile sensor, a capacitive principle was chosen because of its potential for high sensitivity, low power consumption and low temperature effects. Limitations of using capacitive sensors that have been reported in previous research are their

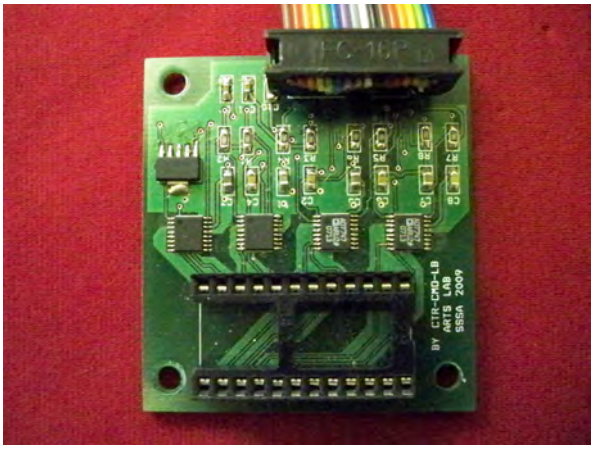

FIGURE 3.22: Signal acquisition electronics

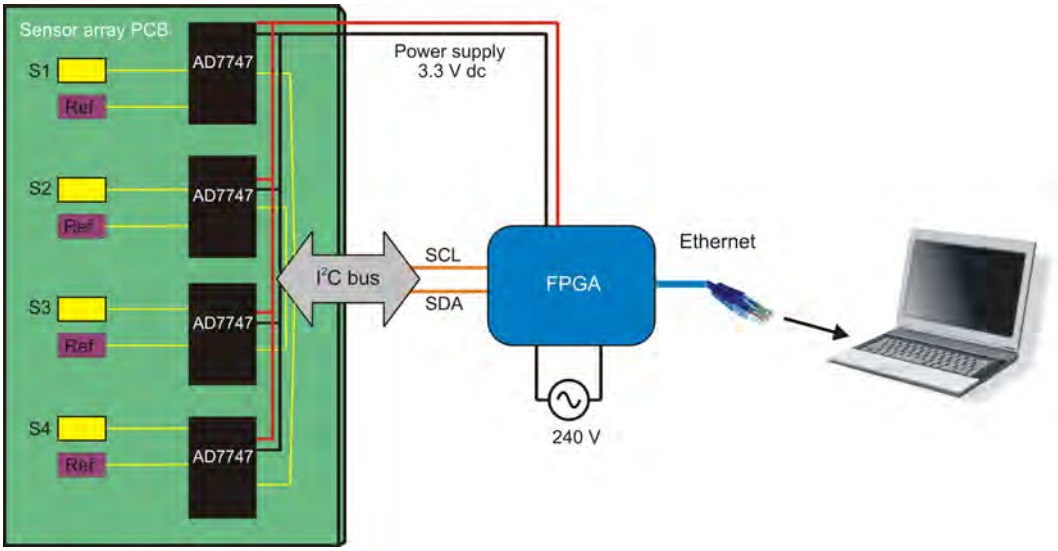

FIGURE 3.23: Schematic of sensor array signal acquisition electronics system

susceptibility to parasitic capacitance and their non-linear response characteristics. In this work, reference capacitors were included in the device to allow a differential measurement reading. Thus, the effects of parasitic capacitance were limited. Non linearity of the output signal is not considered an issue for the purpose of this device as a linear response over the applied range is not imperative as long as the device response to varying textures and loading conditions is established. Further, as mentioned in Chapter 2, the biological mechanoreceptors that the sensors in this work are designed to mimic also display non-linear responses to

applied stimuli.

Analytical techniques based on small deflection plate theory were used to conduct preliminary analyses of sensing diaphragms. Based on this, two sensor diaphragm designs were pursued: a fixed - fixed diaphragm and fully clamped diaphragm. Following this, Finite Element Analysis was used to conduct a more detailed analysis of the sensor behaviour. The final designs took into consideration the trade-offs between device size and sensitivity, both imposing contradictory demands. Further, fabrication induced requirements were also considered at this stage.

The implementation of sensors into a linear array of 4 sensors was described. The designed sensors had a total length of 1800 μm (including the sensing element and connection pad) and a centre to centre distance of 570 μm. This allows a density of about 95 channels/cm^2 to be achieved which is comparable with the innervation density of SA I units in the distal part of the finger pad which is estimated to be about 70/cm^2 [28].

Finally, the design of the signal acquisition electronics for converting the capacitance signal from the sensors to a digital output was described.

4

Fabrication of the tactile sensor array

Contents

Summary This chapter describes the microfabrication processes used to fabricate the tactile sensor array.

4.1 Process overview

Standard microfabrication techniques were employed to fabricate the tactile sensor array. The process flow is shown in Fig. 4.1. Further details on each technique are discussed in the following sections.

4.1.1 Silicon-on-insulator (SOI) substrates

Silicon-on-insulator wafers (SOI) are laminar structures which consist of three main layers: a thin top layer of silicon in which functional structures are patterned, an embedded middle insulating silicon oxide layer (buried oxide) and below this a thick bulk silicon layer (handle wafer). SOI wafers are widely used commercially in IC semiconductor device fabrication as they provide a way to increase the speed performance of CMOS circuits while also reducing the power requirements [114]. The use of SOI wafers in the fabrication of MEMS devices allows for a straightforward creation of free standing structures by simple processes. This is done by using the oxide as a sacrificial layer, so that structures in the device layer can be released using hydrofluoric acid (HF) wet etching techniques.

The most commonly referred techniques in the literature for producing SOI wafers are the Synthesis by Implanted Oxygen (SIMOX) and Bonded and etched back SOI (BESOI) techniques. In the SIMOX technique, an oxygen implantation step is carried out followed by a high temperature (> 1300 °C) annealing step. For wafers manufactured using this method, the buried oxide thickness is limited to 800 - 1000 Å[115].

The fabrication of Bonded and etched Silicon on oxide wafers (BESOI) is schematically shown in Fig. 4.2. Two wafers, one of which is covered with a thick oxide layer, are

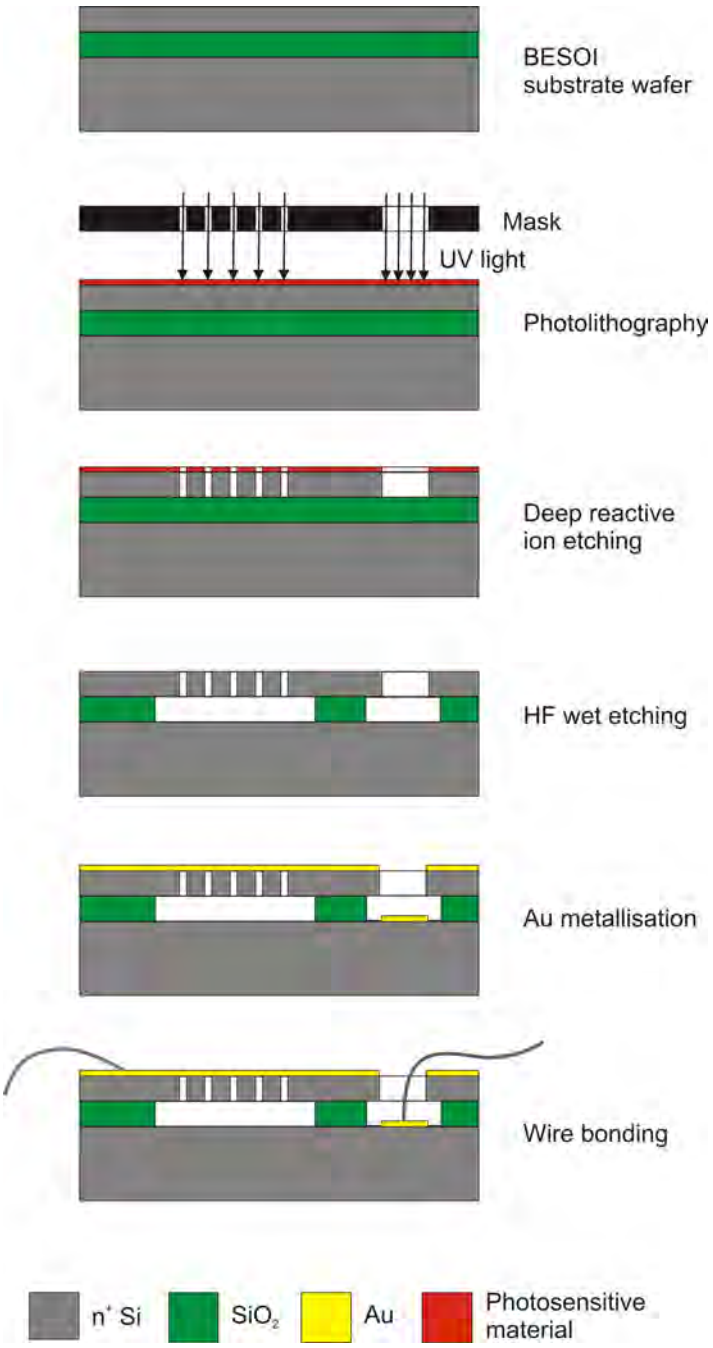

FIGURE 4.1: Sensor fabrication process flow

bonded using Van der Waals forces and then annealed at approximately 1100°C. This causes a chemical reaction that bonds the interface between the two wafers. One of the wafers is then thinned down to the required thickness by the mechanical grinding and polishing. This forms the device layer; a thickness uniformity of 10 - 30% is usually attainable [115].

BESOI wafers have been used as substrates in the development of micromachined accelerometers [116] and pressure sensors [117]. The advantages of the use of BESOI substrates for the fabrication of micro-sensors include the ease with which free standing structures can be manufactured and the possibility for the incorporation of signal processing electronics on the same substrate [118].

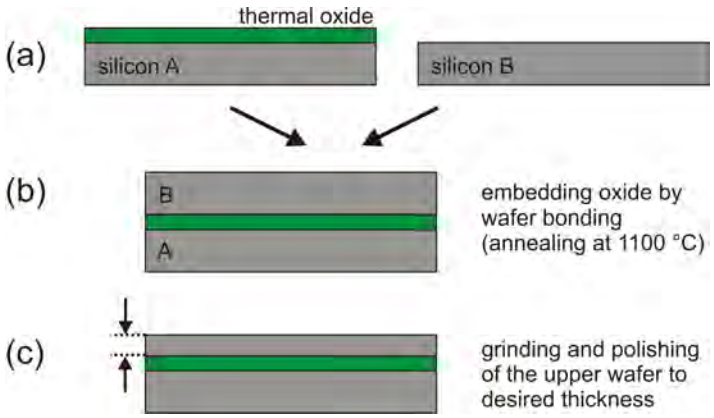

FIGURE 4.2: Fabrication of BESOI wafer

To fabricate the sensors presented in this work, 100 mm Bonded and Etched-Back Silicon-On-Insulator (BESOI) wafers with the following specifications were used as substrates:

Device Layer

- Type of dopant: n/arsenic
- Orientation: $<100> \pm 0.5\ ^{o}$
- Thickness: $2 \pm 0.5\ \mu$m

- Resistivity: $<.006\ \Omega$cm
- Particles: <10 @ 0.2 μm
- Finish: polished

Buried Thermal Oxide Thickness: 2 μm $\pm$ 5 %

Handle Wafers
- Type of dopant: n/arsenic
- Orientation: $<100> \pm 0.5$
- Resistivity: $<.006\ \Omega$cm
- Thickness: 300 $\pm$ 5 μm
- TTV: <2 μm

4.2 Photolithographic Mask design

Photolithographic masks are templates that are used to optically transfer a design pattern (e.g. the sensor layout) onto a substrate wafer. They are made from film or glass substrates. Glass masks consists of a patterned opaque chromium layer on a transparent quartz or soda-lime glass substrate. For fabricating the sensors in this work, a single glass mask was used, the patterns of which were designed using AutoCad software and then printed by a mask writer (JD Photo Tools).

The mask layout is shown in Fig. 4.3, a close-up of a single chip is shown in Fig. 4.4.

The design was structured to fit as many sensing chips as possible onto a single wafer. Thus, the fabrication of different designs of sensors is possible in a single wafer fabrication process. 165 square chips were included in the mask, each with a side length of 5.8 mm.

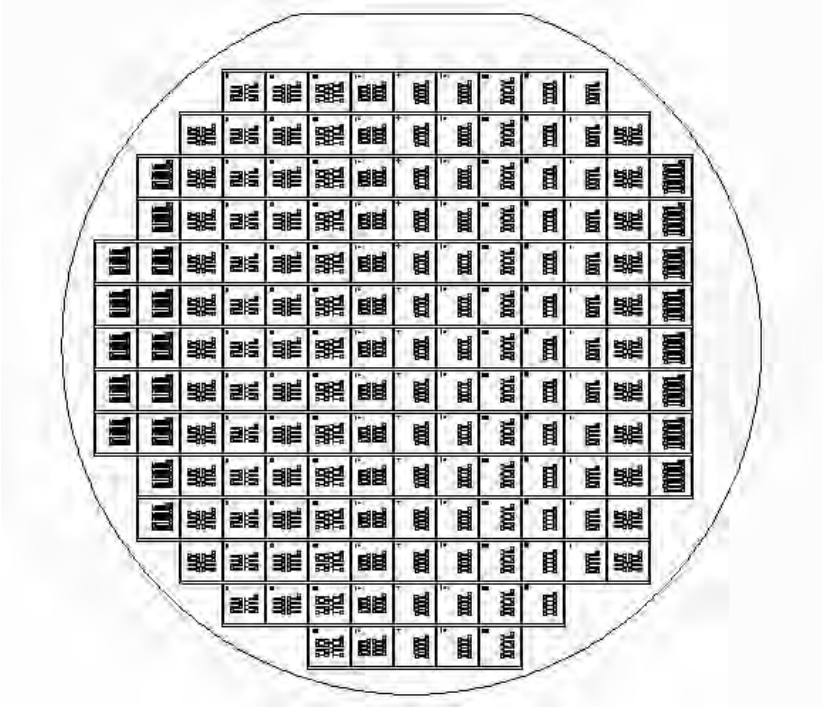

FIGURE 4.3: Full wafer mask showing the implementation of 165 chips on a single wafer

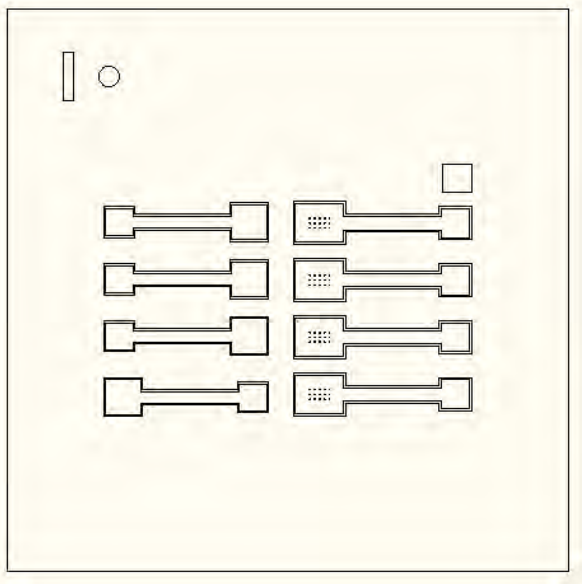

FIGURE 4.4: Close-up view of the mask design showing patterns on a single chip

The distance between adjacent chips was set to 0.3 mm. This was done to take into account the thickness of the blade used in the wafer dicing process for cutting out individual chips. Further, a number of factors were taken into consideration based on the planned use of a HF sacrificial etching processes for the creation of the sensor diaphragms. Fig. 4.5 shows a cross-section of the sensor depicting features that need to be considered during the design of the mask. In the following, the implementation of these features into the design of the mask are given:

- Inclusion of circles of 5 μm in radius, each 50 μm apart within the central section of the sensing diaphragm serving as sacrificial etching access holes. This allows the release of the oxide layer in the central section leaving a free standing plate.
- An isolation gap of 20 μm was left surrounding each sensor and adjacent supportive bulk silicon, to electrically isolate each sensing region from the surrounding silicon.
- An overall increase of 200 μm in width and length of the sensor diaphragm was implemented to take into account the undercutting (u) of oxide that occurs through the isolation gap surrounding each sensor. Sufficient regions of supportive oxide are required to provide adequate clamping of the sensor diaphragm.
- The sensors in an array were spaced 150 μm apart to allow sufficient supportive oxide between adjacent sensors.

4.3 Photolithography

Photolithography is the process that uses optical techniques to transfer geometric patterns from a photomask into a polymer resist. This pattern can subsequently be transferred into

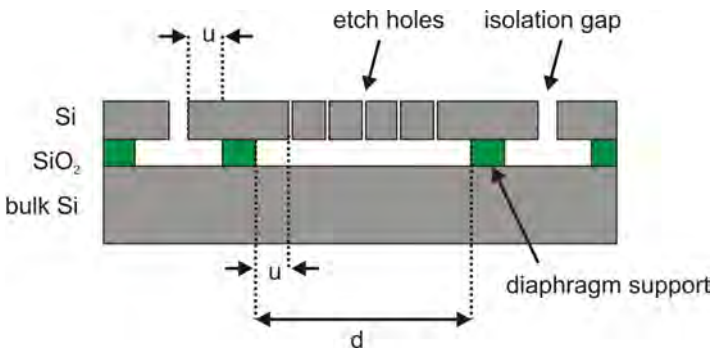

FIGURE 4.5: Cross sectional schematic diagram showing undercutting of the oxide during the sacrificial HF etch process. The dimensions of the sensing diaphragm are increased to allow sufficient area of oxide supports in spite of the undercutting (u)

the substrate wafer by an etching process. The main steps involved are given in the following sections and illustrated in Fig. 4.6.

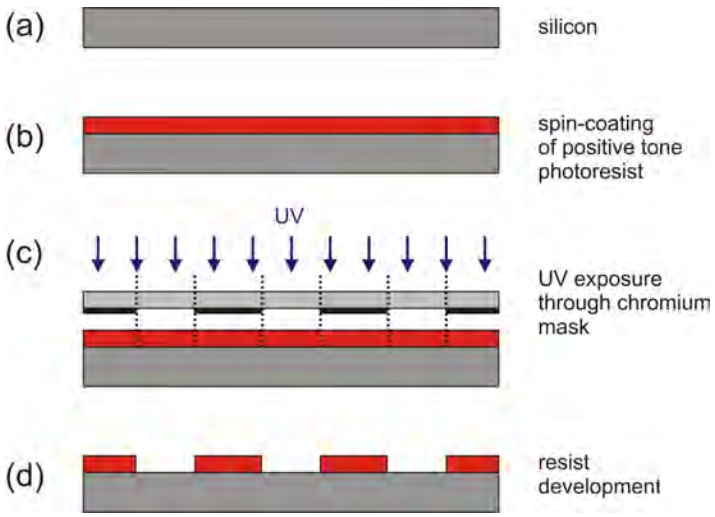

FIGURE 4.6: Photolithography process using a positive photoresist

4.3.1 Wafer cleaning

A wafer cleaning process was carried out using organic solvents to eliminate surface contaminants. The wafer was mounted in a spinner and Acetone was dispensed onto it ensuring

the whole surface of the wafer was covered. The spinning process was then initiated and Isopropyl Alcohol (IPA) were dispensed onto the wafer. Spinning was continued until all the liquid evaporated from the surface. The wafer was then placed on a hotplate at a temperature of 110 °C for at least 50 s to eliminate moisture that could adversely impair the adhesion of the resist to the substrate.

4.3.2 Spin-coating

A positive photoresist (photosensitive polymer), Shipleys S1813 was applied to the surface of the wafer by a spin-coating process. Here, a small amount of resist (approximately 5 - 10 ml) is centrally dispensed on the wafer following which, a 3 step spin process is carried out (500 rpm, 10s; 3000 rpm, 30s; 500 rpm, 10s). This results in a photoresist thickness of approximately 2 μm. The wafer is then soft baked on a hotplate at 115 °C for 90 s. Soft baking was carried out to decrease solvent levels in the photoresist and improve adhesion to the wafer. A high solvent level leaves the photoresist tacky and susceptible to particulate contamination at subsequent handling stages [119]. Further, a high solvent content negatively affects the dissolution discrimination between exposed and unexposed regions of photoresist.

4.3.3 Exposure to ultra violet (UV) light

The photoresist was exposed to UV light (260 mJ/cm^2) using a Canon Mask Alligner (PLA-501 FN, Fig. 4.7) in hard contact mode for 10 s. Photoresists contain a base resin that determines their mechanical and thermal properties, a photoactive compound (PAC) determining their sensitivity to radiation exposure and an organic solvent that determines their viscocity [120]. In positive photoresists such as S1813, exposure to UV radiation causes

decomposition of the PAC which then renders these regions soluble to an alkaline developer.

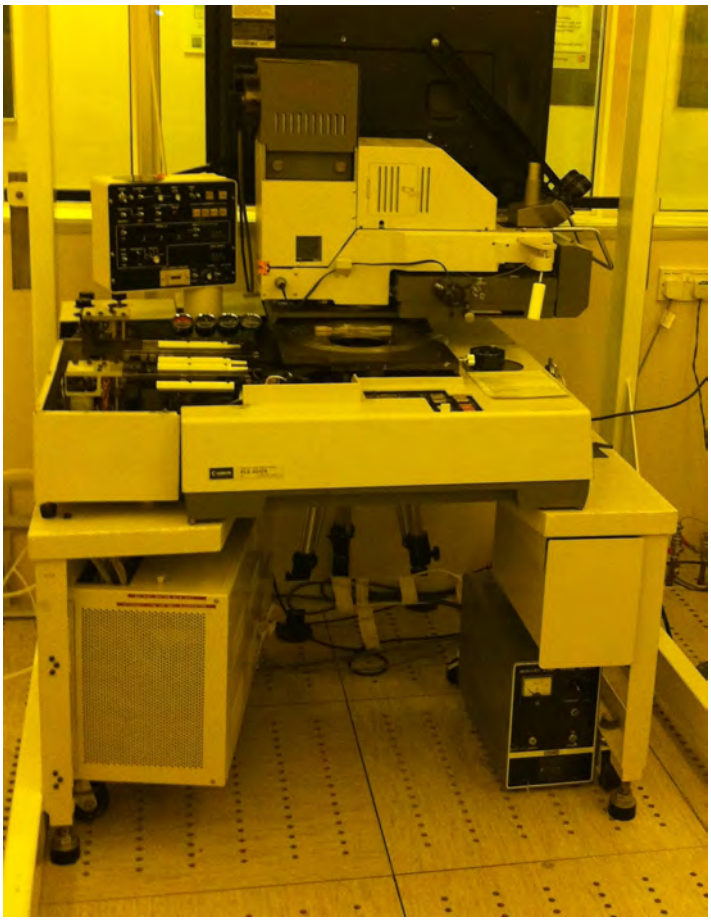

FIGURE 4.7: Mask aligner (PLA-501 FN) used during photolithography process

4.3.4 Resist development

To develop the exposed wafer, it was immersed in a solution of MF319 (an alkaline solution) which was gently agitated for 2 minutes. Following this, the wafer was rinsed with distilled water.

4.4 Reactive Ion Etching (RIE)

Reactive Ion Etching is a dry etching technique where external energy in the form of radio frequency (RF) power is used to drive chemical etching reactions in low pressure chambers [121]. Stray electrons are accelerated and collide with molecules of a reactant gas (such as SF_6) to form excited and ionised species. Thus, a combination of chemical and physical processes are used to etch the silicon surface. Halogens such as fluorine and chlorine etch silicon because the Si - halogen bond is much stronger than the Si - Si bond [120]. While excited molecules formed from dissociation of the reactant gas are involved in the chemical etching of silicon, the purpose of ion bombardment is to introduce directionality and enhance the physical removal of material. Thus high etch rates and anisotropy can be achieved.

Deep Reactive ion etching (DRIE), also known as the Bosch process or time multiplexed deep etching process (developed by Robert Bosch in 1992), is an anisotropic RIE etching technique used to form very high aspect ratio structures (such as that shown in Fig.4.8) in a silicon substrate [120, 122]. This process was used to define the sensing structures of the MEMS tactile sensor array of this work. The etcher used was Surface Technology Systems (STS) ICP DRIE System (Fig. 4.9) which is an inductively coupled plasma (ICP) etcher that generates high density etching species at low pressures and low DC bias [123]. The process involves a cyclic mechanism with the use of alternating etch and sidewall passivation steps. During the etch phase, ions generated from sulphur hexafluoride (SF_6) plasma are accelerated towards the silicon substrate (which has a bias of - 5 to - 30 V). In the passivation phase, octafluorocyclobutane (C_4F_8) is used to deposit a teflon like polymer all over the substrate. Thus, in the subsequent etch step the directional ion bombardment allows the removal of material from the horizontal surfaces of the substrate, leaving the sidewalls protected by the

chemically inert polymer layer.

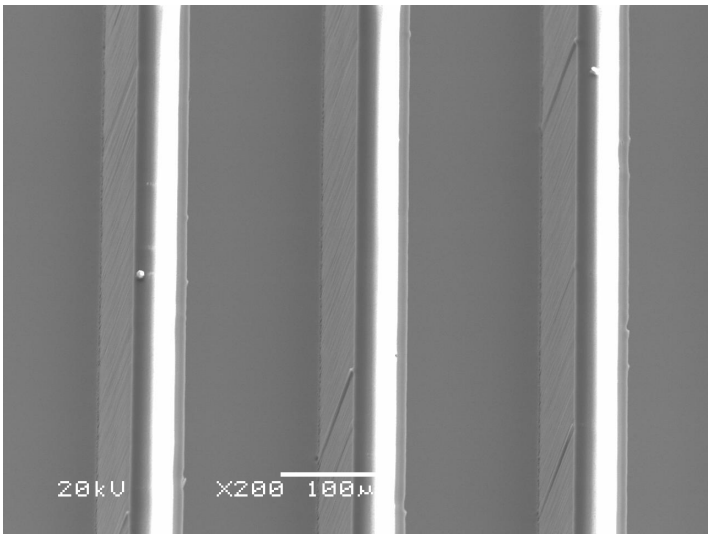

FIGURE 4.8: Gratings manufactured using DRIE (Bosch) process

The parameters used for the etching process are given in Table 4.1.

TABLE 4.1: The parameters used for the etching process with the STS ICP DRIE Etcher

	Etch cycle	Passivate cycle
SF_6 Flow rate	130 sccm	0 sccm
C4F8 Flow rate	0 sccm	100 sccm
Duration	8 s	5 s
13.56 MHz Platen power	600 W	600 W

4.5 Wafer dicing

Following the DRIE process, the wafer containing the sensor array chips (still coated with photoresist), was diced into individual chips with dimensions of 5.8 mm x 5.8 mm using a Disco DAD320 wafer dicing saw machine.

FIGURE 4.9: Surface Technology Systems (STS) DRIE system

4.6 Oxygen plasma cleaning

In order to eliminate any debris resulting from the dicing process (see Fig.4.10) and other possible contaminants on the chip and to strip of the photoresist, a cleaning step is necessary. The chips were rinsed in acetone followed by IPA and then dried using Nitrogen gas. A 20 minute long oxygen (O_2) plasma cleaning process was carried out using the STS etcher. This is a commonly used MEMS process where a plasma generated in subatmospheric pressures of oxygen creates highly reactive ions which bombard a surface and react with organics forming volatile species [124].

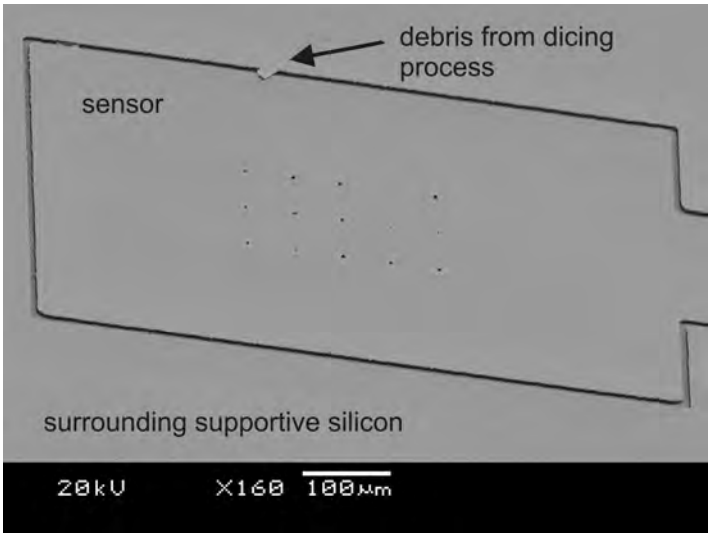

FIGURE 4.10: SEM image showing debris generated during the dicing process can cause unwanted interconnections between the sensor and surrounding supportive Si

The parameters used for the O_2 plasma cleaning process are given in Table 4.2.

TABLE 4.2: Parameters used for the O_2 plasma cleaning process with the STS Etcher

O_2 Flow rate	100 sccm
Duration	20 minutes
13.56 MHz Platen power	800 W

4.7 Wet etching

The etching of the buried SiO_2 layer was carried out to form the air gap between the two electrodes of the capacitive sensor. This was done using the hydrofluoric acid (HF) wet etching process. Among acids, only solutions containing hydrofluoric species are able to break the strong Si-O bond because of the high electronegativity of fluorine [125]. Etch holes (having a radius of 5 μm), that were patterned on the device layer, allow access of HF to the buried oxide layer. The process was carried out using 40% liquid HF which is diluted in distilled water. The dissolution of the SiO_2 layer by liquid HF is based on the following

chemical reaction [125]:

$$SiO_2 + 6HF \rightleftharpoons 2H^+ + SiF_6^{2-} + 2H_2O \tag{4.1}$$

Etch rates of approximately 1 - 1.25 μm/min were achieved. The chips were immersed in the liquid HF solution for approximately 40 minutes. The timing of the etch process is critical in defining the geometrical dimensions of the sensing diaphragm. Hence, prior to the etching process, the etch rate was determined by monitoring the geometric profile formed after a specified etch time period (Fig. 4.11). This is possible as 2 micron thin silicon is optically transparent and therefore the oxide profile clearly visible using an optical microscope. Thus the chips were etched until the area defined as the sensing diaphragm had fully released.

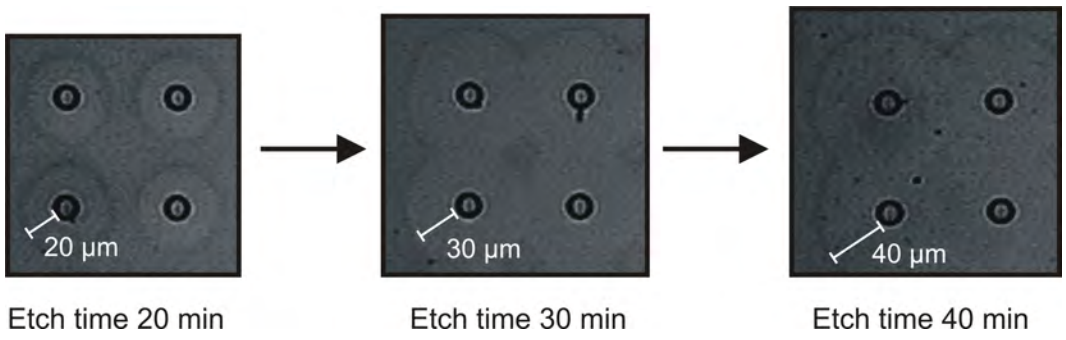

FIGURE 4.11: Etch profile resulting from sacrificial etching

Following this the chips were rinsed in isopropyl alcohol (IPA) and distilled water and then directly transferred into beakers containing IPA solution. To dry the chips, they were removed from IPA solution and directly transferred onto a hotplate at 115 °C. This allowed the rapid evaporation of the IPA, which encourages the lift of the sensor diaphragm thereby avoiding stiction, a commonly encountered issue during sacrificial wet etching processes.

The term stiction describes the unintentional collapse and adhesion of compliant microstructure surfaces to the substrate below; it occurs when restoring forces are unable to

overcome interfacial forces [82]. During the HF sacrificial etching process, release-related stiction may occur primarily due to capillary forces [126]. Such forces are generated because of surface tension of the liquid - vapour interface when the thin liquid layer between the two plates evaporates (Fig. 4.12).

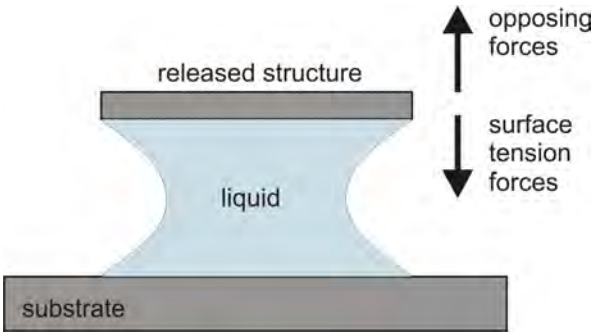

FIGURE 4.12: Forces on the released structure following HF wet etching [122]

Figure 4.13 shows the stiction following HF release of a clamped circular diaphragm and a fixed-fixed beam. Special drying processes such as supercritical drying and freeze drying can be used to avoid stiction by eliminating the formation of the liquid-vapour interface and therefore any associated capillary forces [127]. Another method that is used to avoid stiction during HF etching is to use HF vapour-phase etching [128]. With the drying technique applied in this work, through the rapid evaporation of IPA on a hotplate, no stiction occurred in Design 2 sensors. In some Design 1 sensors stiction was observed and therefore the yield of these sensors was lower. The resulting sensor diaphragm profiles formed following wet etching are shown in Fig. 4.14.

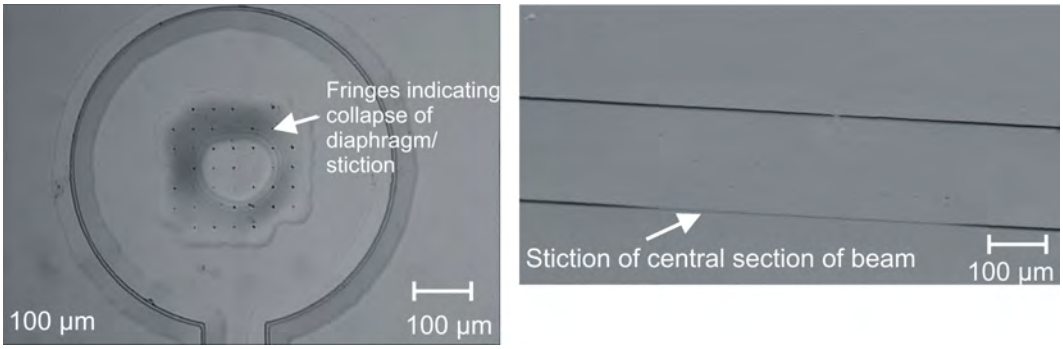

FIGURE 4.13: Optical microscopy images showing (left) Stiction of circular diaphragm following HF wet etching as seen through optical microscopy, (right) SEM image showing collapse at the central section of a long beam structure

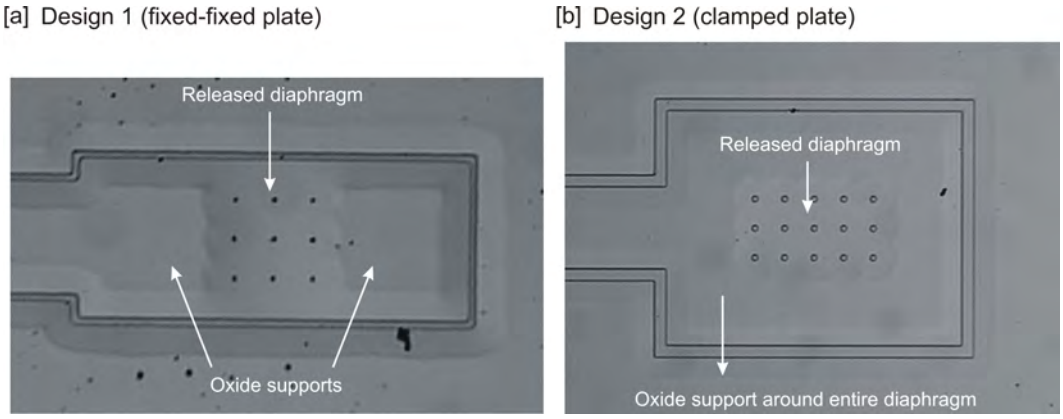

FIGURE 4.14: Diaphragms formed following HF release etch

4.8 Metal deposition

In order to make electrical contacts to the sensor chips, a gold metallisation process was carried out using the process of evaporation. This is a physical vapor deposition (PVD) method, where a material is heated above its boiling point, transported through a high vacuum [1] and condensates on a cooler substrate [78]. The heating of the target material is facilitated either by an electrical current (thermal evaporation) or a guided electron beam (e-beam evaporation).

In thermal evaporation, the desired source metal is placed in a metal crucible typically

[1] typical chamber pressures are around 10^{-6} mbar

made of tungsten which is electrically heated. Metal atoms in the generated vapour then condense on the substrate material. The limiting process in this method is the maximum temperature of the crucible typically used which is approximately 1400°C [121]. In e-beam evaporation, an electron beam generated using a high intensity electron gun (5 keV) is magnetically focused on the target material which then generates the vapour for deposition. This enables higher temperatures to be attained in comparison to those in the thermal evaporation process [121].

Metals with low electron deficiency such as titanium and chromium can be used to promote adhesion between the silicon substrate and gold [129]. Because of the high melting point of titanium (1667 ^{o}C), e-beam evaporation was used to deposit it on the sensor chips; with an approximate thickness of 20 nm. Following this, a 200 nm thick layer of gold (melting point 1064 ^{o}C) was deposited using thermal evaporation. The metallisation was carried out using the Auto 500 Electron Beam - Filament Evaporation System.

4.8.1 Fabricated devices

Fig. 4.15 shows a Scanning Electron Micrograph (SEM) image of the fabricated sensor array. Fig. 4.16 is a close up of a single sensor. A cross-section of the device showing the two plates of the capacitive sensor and the enclosed airgap are seen in Fig.4.17.

The dimensions of the sensing diaphragm are determined during the HF wet etching stage of the fabrication process. This is because the amount of undercutting of oxide is affected by factors such as etchant concentration and timing of the etch process. As 2 μm thick silicon diaphragm is optically transparent, it was possible to view the diaphragm profile

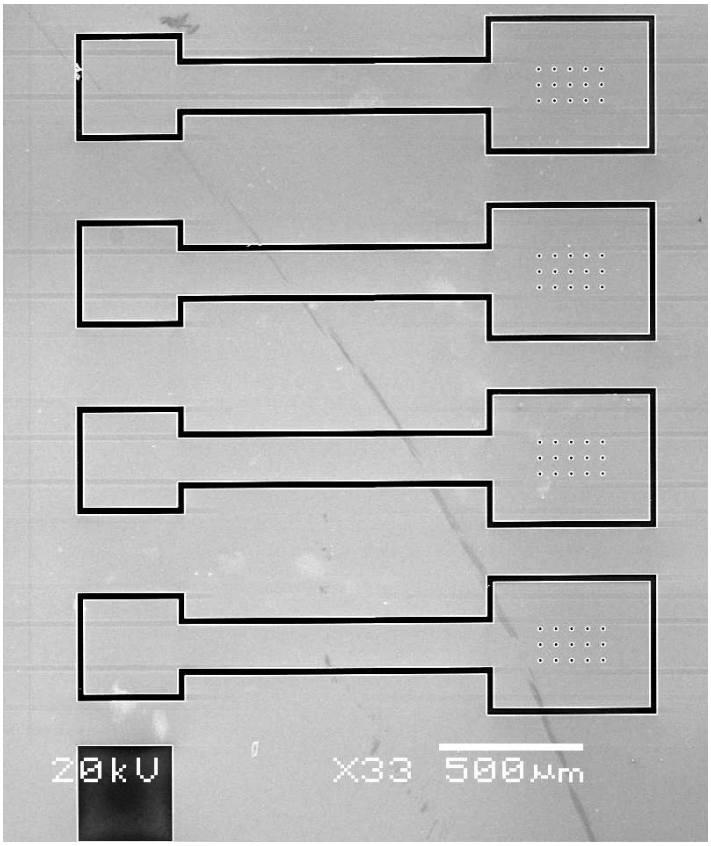

FIGURE 4.15: SEM image of sensor array

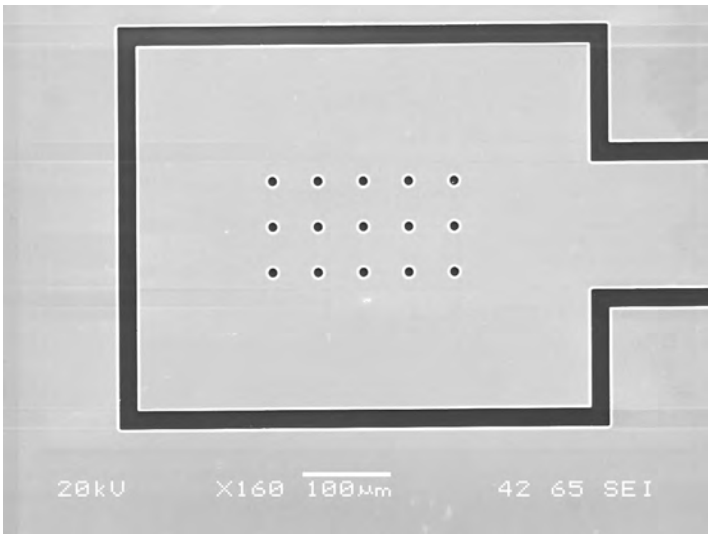

FIGURE 4.16: SEM image of single sensor

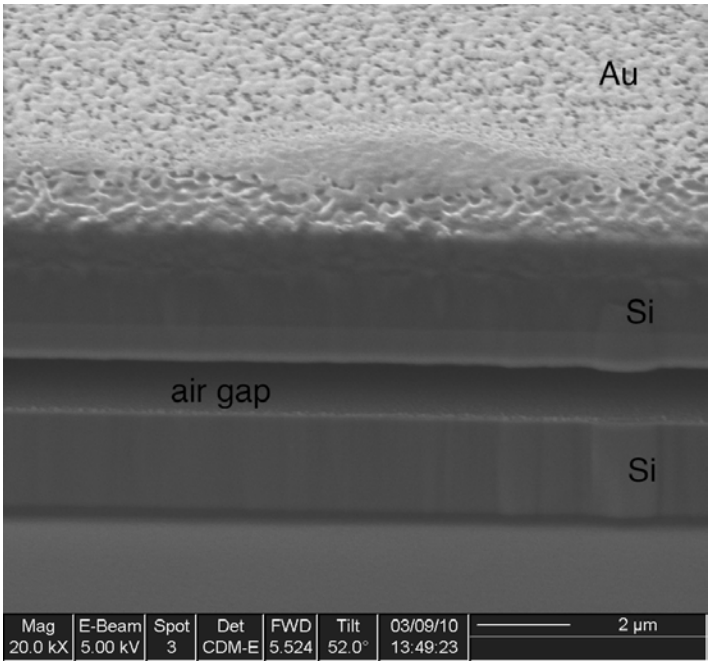

FIGURE 4.17: Cross-section of capacitive sensor

using optical microscopy and measure the resulting diaphragm dimensions. Measurements made from samples taken from three different chips for both sensor designs 1 and 2 are given in Table 4.3.

TABLE 4.3: Dimensions of sensor diaphragms

	Design 1 (fixed-fixed)	Design 2 (clamped)
Planned dimensions	200×200	300×200
Measured dimensions	182×200 171×200 195×200	277×180 278×182 322×224

4.9 Wire bonding

The sensors were mounted onto standard dual-in-line ceramic packages (Spectrum Semiconductor Materials, INC., 24-DIP) (see Fig. 4.18). Wiring to the bonding pads of each sensor

and reference capacitor was performed by means of a wire bonder using 25 μm thick aluminum wires. To protect the wires from damage during subsequent sensor testing, they were coated with a UV curable epoxy (Epo-Tek OG142).

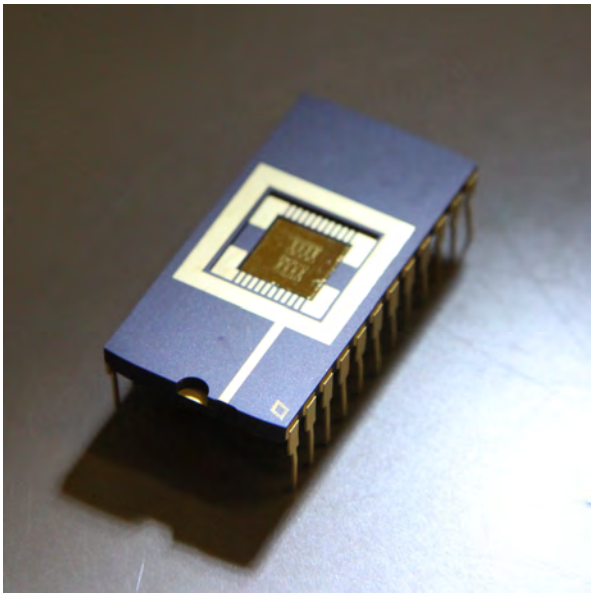

FIGURE 4.18: Fabricated sensor die mounted on DIP chip carrier

4.10 Conclusions

In this chapter, the processes that were used to fabricate the sensor array were described. Fabrication of the sensors was optimised towards a minimum number of processing steps and the sole use of simple standard microfabrication techniques to reduce costs. In comparison to previously reported MEMS based capacitive devices ([87, 90]), the use of BESOI wafers as a substrates allowed for fewer and less complex process steps. Some specific advantages of the proposed fabrication methods are:

- The use of a single mask in realisation of the device
- The use of single sided wafer processing

- Potential difficulties associated with the use of anodic bonding processes (a commonly used process in capacitive sensor fabrication [130] were avoided. These include "snap-down" or sticking of suspended diaphragms due to the presence of electrostatic forces [109, 131], introduction of residual stresses in the sensing diaphragm as a result of a mismatch in thermal coefficients of bonding substrates and complexities in accessing electrical connections from the sealed cavity [99, 132].

Design 2 (clamped diaphragm) sensors showed higher yield in comparison to Design 1 (fixed-fixed diaphragm) sensors.

Limitations with the proposed fabrication method include the relatively high costs of BESOI wafers. Further, as discussed in Section 4.2, sensors are made larger than required by the design, to take into account undercutting of the sacrificial oxide. In the fabricated devices, the silicon dioxide support regions were made larger than required to ensure that a sufficiently large supportive area is maintained following the HF sacrificial etch. However, once the required etch rates have been established, the devices can be made smaller.

In the following chapter, the coating of the sensors with artificial skin is covered.

5

Sensor implementation into artificial skin

Contents

Summary In this chapter, the requirements of artificial skin within which the fabricated MEMS tactile sensors can be embedded are discussed. Following a description of human skin properties, an overview of materials that can be used as human skin like substitutes for artificial finger applications is given. Material testing of candidate materials is presented. Finally, the process used to package the sensors within suitable skin like materials is described.

5.1 Objectives

Artificial skin provides a human skin like covering to protect the fabricated MEMS based tactile sensors and transmit mechanical surface forces in the form of distributed mechanical stress, strain or deformation to the embedded sensing structures. The skin thus forms a packaging layer for the devices and furthermore effects its overall performance. The main functions of the artificial skin packaging are [80]:

- To protect the sensor from external influences and environmental effects such as moisture and particle contamination.
- To attenuate rapid impact or peak forces that are encountered during exploration and thus protect the sensors from mechanical shock.
- To provide a controlled (reliable and repeatable) mechanical and electrical interface between the sensor and its environment.

The MEMS tactile sensors designed in this work are based on a capacitive principle which makes them prone to electrical interferences or noise. In order to provide robustness against noise, the chosen packaging material should be electrically non-conducting.

5.1.1 Material requirements for tactile sensor packaging

As the tactile sensors developed in this work are to be incorporated into an artificial finger, the skin enclosing them should provide human skin like compliance and cosmetic appearance in addition to allowing the successful integration with MEMS devices [133].

Thus the main requirements for materials that can be used to form the skin of artificial fingers are [134]:

- Skin like mechanical properties such as compliance and conformance
- Adequate friction under a range of expected grasping conditions
- Abrasion and chemical resistance
- Compatibility with embedded tactile sensors

In brief, a material is required that emulates the functionality of biological skin to a maximum extent. To gain deeper insight into these requirements, the next section gives an overview of the structure and function of human skin. This will provide a basis for the selection of a suitable artificial skin material.

5.2 Human skin characteristics

5.2.1 Structure

Macroscopically, the human finger pad is composed of layers of skin, subcutaneous fat, bone and nail. The skin is a multilayer structure consisting of epidermis, dermis and underlying subcutaneous fat tissue (Fig. 5.1).

The superficial layer, the epidermis has a higher stiffness compared to the underlying dermis (Young's modulus E of 130 kPa and 80 kPa respectively) [137]. It has a thickness of approximately 0.06 to 0.12 mm [136] and consists largely of keratinocytes that are formed by division of cells in the basal layer of the epidermis. The uppermost layer of the epidermis is the stratum corneum, which is composed of dead, flat skin cells that are shed approximately every two weeks. This layer gives skin a very high electrical resistivity [138]. The dermal

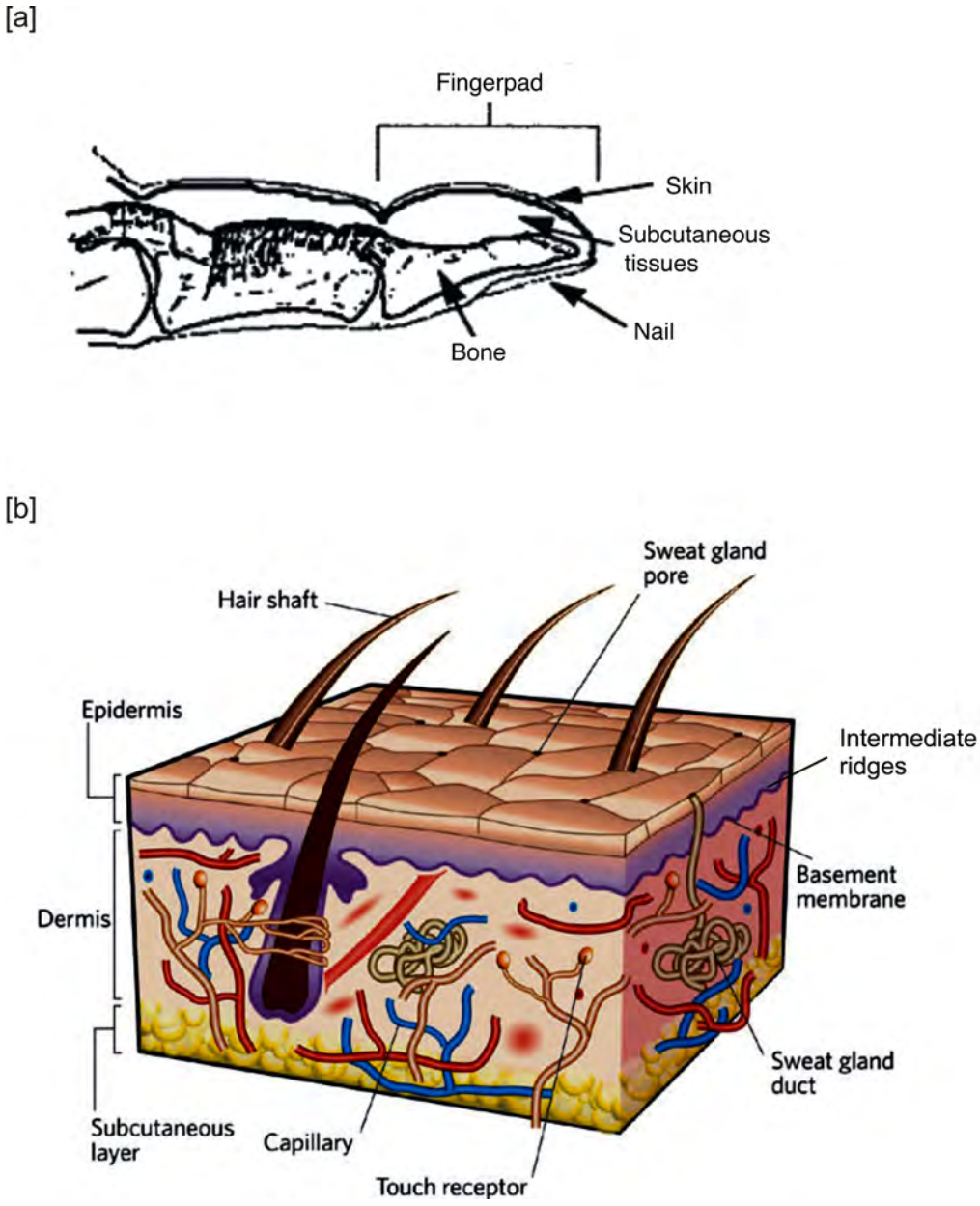

FIGURE 5.1: [a] Macroscopic features of finger [135] [b] Diagram of human skin showing the upper epidermal barrier skin layer (0.1 to 0.2 mm thick) and the lower dermal layer (1 to 4 mm thick) [136]

layer is 1 to 4 mm thick and is composed mainly of dermal fibrous proteins, collagen and elastin embedded in an amorphous ground substance [139].

The contribution of the epidermis to the mechanical properties of skin is usually neglected. Dermal collagen is suggested to be the main contributor of the mechanical properties of skin, which has been confirmed by the similarities found in their responses to mechanical testing with that of full thickness skin [140]. The mechanical properties of the dermal components of human skin are summarised below [141]:

- Collagen fibres are the main constituents of the dermis accounting for 77% of its fat-free dry weight. They form an irregular network of wavy coiled fibres that run almost parallel to the skin surface. They exhibit high stiffness with a Young's modulus range of approximately 0.1 GPa to 1 GPa (in the linear region) and low extensibility, rupturing at strains of 5 - 6%.

- Elastin fibres are the second main component of the dermis making up 4% of the fat-free dry weight. They have a lower stiffness compared to collagen ($\sim$ 0.6 MPa) and exhibit reversible strains of more than 100%.

- Reticulin is found in much smaller amounts in the dermis (0.4% of the fat-free dry weight). Its mechanical properties are unknown but similarities in its molecular structure and morphology to collagen indicate similarities in their properties.

- Ground substance is responsible for the viscoelastic behaviour of the dermis

5.2.2 Function

The skin has mainly protective, perceptive, and regulatory functions. It forms a water, electrolyte and bacteria-proof barrier to the outside world and also protects against mechanical, chemical, thermal and photic damage [142, 143]. The skin has an important function in touch sensation as the source of tactile information is the distribution of spatio-temporal mechanical loads on the human skin at the contact interface [41]. The stress and strain fields generated at the mechanoreceptor nerve terminals are responsible for the transduction of mechanical tactile stimuli into neural responses. Their signal output frequency depends on the local intensity of the stimulus at the receptor location [41]. Skin mechanics is important in determining the relationship between surface indentation of the finger pad and stress/strain fields at the location of mechanoreceptors [112].

5.2.3 Role of microstructures

The epidermal ridges (fingerprints) provide a texture to the fingerpad surface, which is believed to create optimal friction and adhesion characteristics that allow humans to securely grip objects. A very smooth surface would result in a large coefficient of friction causing large scale slip-stick motion when the sensor slides over a smooth surface, making control of sliding and manipulation difficult [52].

Various authors have suggested that fingerprints have a role in tactile sensation [73, 144, 145]; although the mechanisms behind this are not fully understood. In 1954, Cauna proposed the signal enhancement at mechanoreceptor terminals through a 'lever arm mechanism'; where the epidermal ridge and underlying intermediate ridge operate as a single unit,

with the intermediate ridge acting as a lever that magnifies indentation imposed at the epidermal ridge [144]. Maeno et al. explored the role of finger tip microstructures by including fingerprints and intermediate ridge like structures in a mechanical model of the finger pad. They showed that the presence of such microstructures led to concentrations in normal forces, tangential forces and strain energy density at locations coinciding with that of the SA I receptors (found in the tips of intermediate ridges) [73].

Scheibert et al. suggested a different mechanism whereby fingerprints contribute to fine texture perception through vibrations induced when humans actively slide their finger over a surface of interest [145]. They compared the responses of a biomimetic force sensor incorporating a smooth coating and one whose surface was patterned with parallel ridges imitating the fingerprints, to textured surfaces. They showed that the fingerprinted sensor amplified the pressure modulations (measured by the force sensor) generated by a texture. Their findings were indicative of the role of fingerprints on the spectral filtering properties of skin in dynamic tactile exploration.

5.2.4 Mechanical properties

The human skin has heterogeneous, anisotropic and non-linear viscoelastic characteristics and its properties vary with age, body location and between people. It exhibits non-linear and time dependent responses to mechanical loading. The skin is a soft, compliant and conformable material. Compliance is the property of skin where large displacements occur under the application of very small forces [42]. Studies have shown that a normal force of 2 N on the finger pad produces a skin displacement of about 2 mm [146]. Conformance is the ability of skin to follow the contours of surface features of an object. The inability of

skin to deflect would prevent information regarding spatial features of a surface from being transmitted to underlying sensors.

Experimental data from Serina et al. (1997) on human fingertip loading and unloading using fingertip tapping experiments is shown in Fig. 5.2 [147]. The behaviour represents characteristics of fingerpad tissue of which the skin is one component. The fingerpad was seen to be more compliant at forces less than 1 N, but increased in stiffness at higher forces.

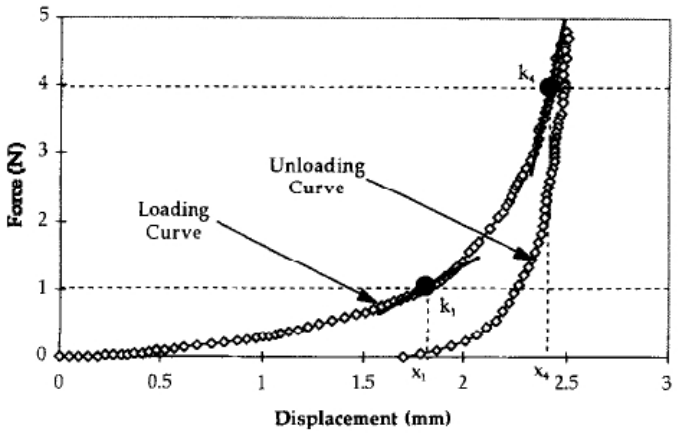

FIGURE 5.2: Typical fingertip pulp force-displacement curve from experimental data on human subjects [147]

Skin exhibits viscoelasticity which means that its mechanical response to loading consists of viscous components associated with energy dissipation and elastic components associated with energy storage [148]. The main elastic components of skin are proteins (collagen and elastin), while the viscous components are water and other highly hydrated macromolecules [149]. Skin exhibits hysteresis (differences in the stress-strain relationship during loading and unloading), creep (increasing displacement during constant force) and stress relaxation (decreasing force during constant displacement) characteristics. The elastic modulus of skin increases with an increase in strain rate [140].

Because of the viscoelastic properties of biological skin, the mechanical stimulus transmitted to the embedded mechanoreceptor neurons is dependent on the magnitude of the external stress and its rate of change. Skin has been mechanically modelled by using combinations of springs (representing elastic components) and dashpots (representing viscous components). The standard solid linear model is commonly used to describe the behaviour of skin and skin substitutes (Fig. 5.3) [149]. It constitutes a combination of a spring (stiffness E_2) in parallel with a spring (stiffness E_1) and dashpot (η) in series. The time-dependent behavior of a viscoelastic material in the stress relaxation process can be described by a summation of the exponential terms as given in Equation 5.1:

$$Y(t) = Y_e + \sum_{i=1}^{n} a_i exp(-b_i t) \tag{5.1}$$

where *Y(t)* is the decaying parameter (such as stress), *t* is time, Y_e is the residual value of *Y(t)* when *t* is ∞, a_i and b_i are constants characteristic of the material.

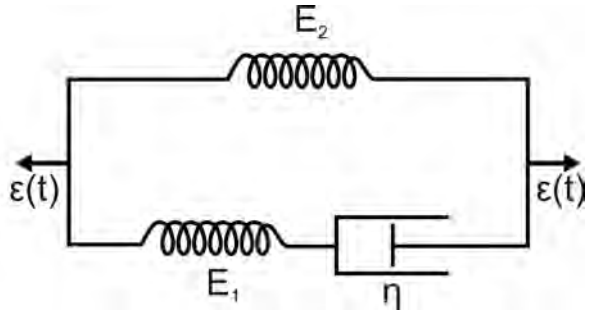

FIGURE 5.3: Standard solid linear model: A parallel combination of a spring (elastic element) and a dashpot (viscous element) in series with a spring. Figure adapted from [149]

5.2.5 Mechanical testing

To determine the mechanical properties of skin, tensile, indentation and suction techniques are most frequently used [150]. Tests involving the application of controlled amplitude indentations via punctate probes to the human finger pad have been well documented for assessment of the performance of mechanoreceptors [51]. Indentation tests are also known to be an effective and relatively simple way to conduct biomechanical assessments of the skin in compression, with the test itself resembling the situation of palpation [151].

With this in consideration, indentation testing was used to analyse the behaviour of skin and the other candidate skin substitute materials that are described in the following sections. A mechanical testing machine, ELF 3200, (Bose, Electro-Force Systems Group, MN with a 225 N load cell and nominal precision of $\pm$ 0.005 N) was used to conduct indentation testing of samples by applying known forces or displacements. A rigid spherical probe with a radius of 10 mm was used to apply the stimulus. As relatively small forces of approximately 0.3 - 4.5 N are used during typical tactile explorations [55, 152], applied forces of up to 5 N were implemented in this study. Each of the samples tested had a thickness of approximately 2 mm.

To investigate the mechanical response characteristics of biological skin, indentation tests were conducted on excised rat skin samples (supplied by Nicola Hunt, Chemical Engineering Department, University of Birmingham). The use of excised animal skin as a replacement for human skin is common in the study of in-vitro skin properties [153] and hence rat skin was used in this study.

Fig. 5.4 shows a typical force-displacement behaviour of skin for five load-unload cycles of compression indentation testing (maximum force of 5 N, frequency 0.1 Hz). A non-linear

relationship between force and displacement is observed. In the first phase of loading, the load - displacement relationship is approximately linear. In this stage, the mechanical behaviour is mainly dominated by the elastin fibres [141]. Following this, there is an increase in the stiffness of skin which can be attributed to the physical structure of the collagen fibres. As previously described, in a relaxed state, collagen fibres are known to have a wavy appearance. During stretching of skin, there is a gradual straightening of an increasing fraction of the fibres which tend to align themselves along the stress direction. Eventually, after all the collagen fibres are stretched, the stress-strain relationship becomes linear again. After unloading, the fibres return to their wavy configuration [139]. The area bound within the loading and unloading curves represents the energy loss per cycle (hysteresis) which decreases with each cycle and tends to reach a steady state value after a number of cycles.

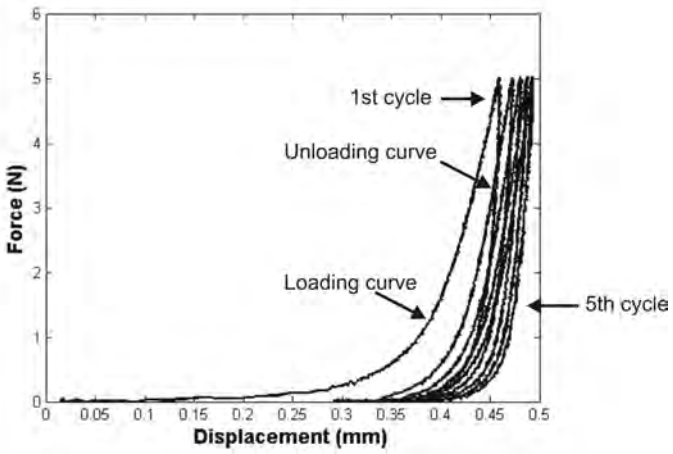

FIGURE 5.4: Typical force-displacement curves for rat skin under 5 loading cycles

The stress relaxation of rat skin is shown in Fig. 5.5[a]. Here, the force required to maintain a constant displacement of 0.2 mm decreases with time. Matlab curve fitting toolbox was used to determine a suitable mathematical fit to the the experimental relaxation data.

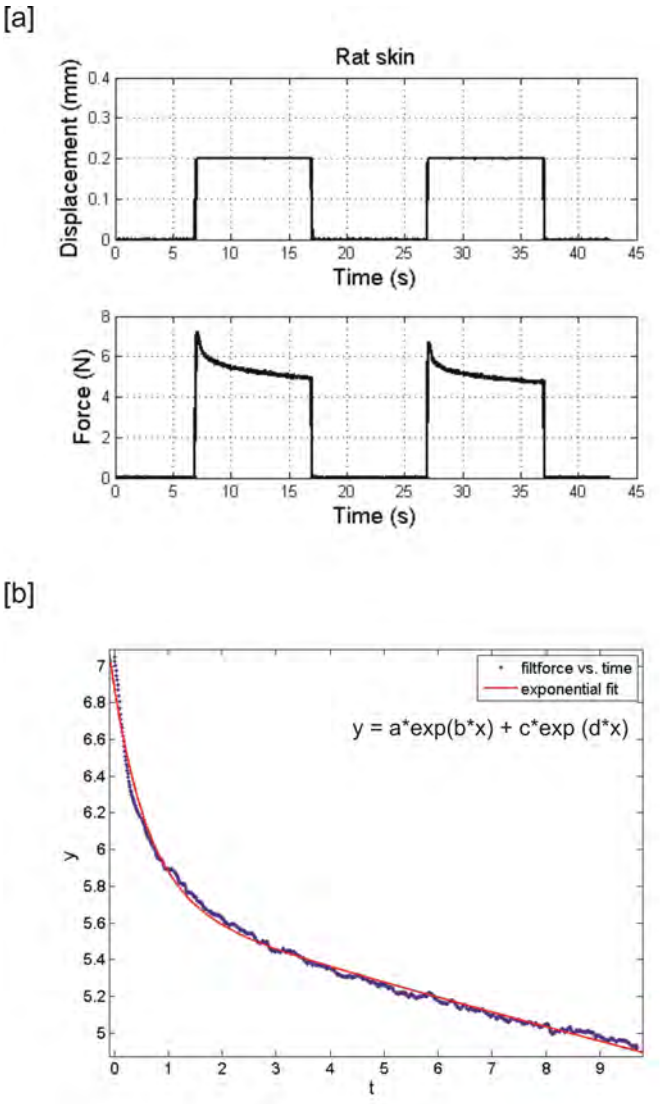

FIGURE 5.5: [a] Stress relaxation of rat skin under constant displacement of 0.2 mm [b] Exponential curve fit of relaxation data a = 1.17, b = -1.5, c = 5.71, d = -0.016

Fig. 5.5[b] shows a double exponential fit applied to the data.

The effect of varying strain rates on the response characteristics of rat skin were also explored. Results, showing the response of rat skin to an applied force of 5 N at different frequencies (or strain rates) is shown in Fig. 5.6. The stiffness of rat skin was found to increase with the strain rate. With increasing frequency, there is a decrease in the resultant maximum displacement and % of recovered displacement in the unloading phase. Table 5.1

summarises the maximum displacement and % of recovered displacement in the unloading phase, obtained under an applied force of 5 N (using a triangular waveform) under varying strain rates.

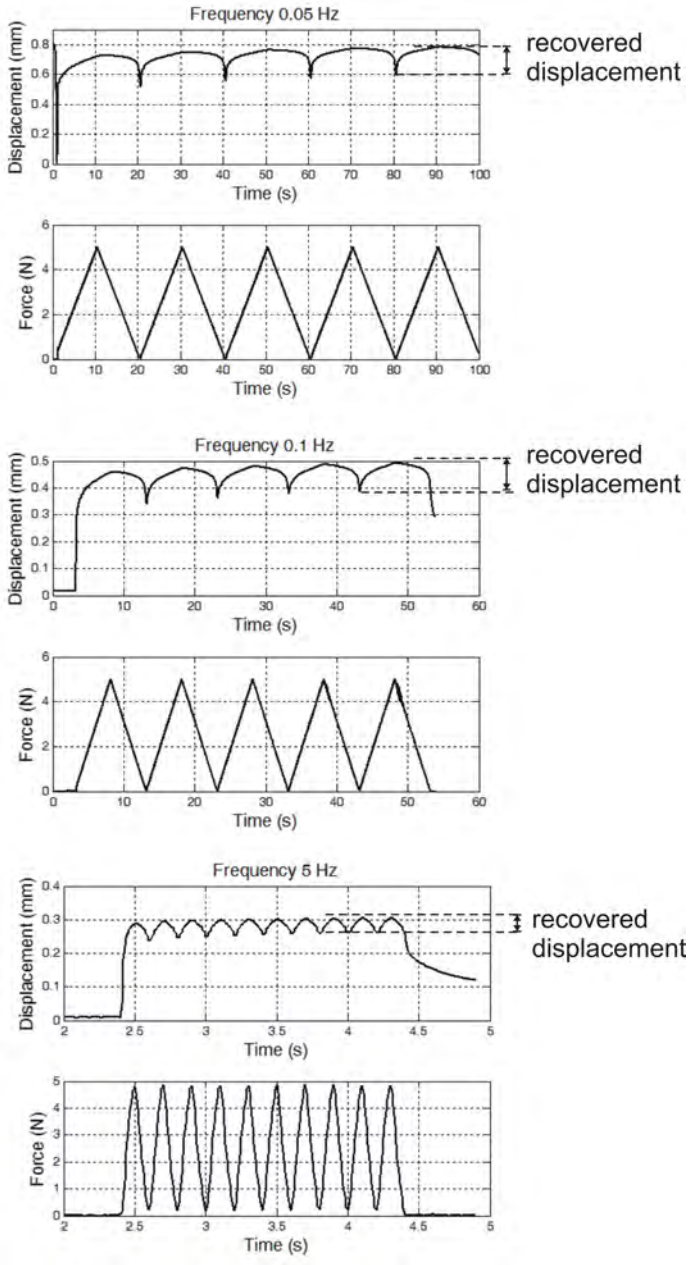

FIGURE 5.6: Change in response of rat skin for applied loading of 5 N under varying applied frequencies of 0.05, 0.1 and 5 Hz

TABLE 5.1: Frequency/ strain rate dependent behaviour of rat skin

Frequency (Hz)	Maximum displacement (mm)	% of recovered displacement
0.05	0.725	28
0.1	0.46	22
5	0.29	19

5.3 Sensor skin candidate materials

5.3.1 Synthetic skin

For the selection of skin like materials for an artificial finger, properties such as viscoelasticity, wear resistance, tactile sensor compatibility, suitable friction and adhesion during surface exploration are important [134]. In addition to this, the material should be conformable to optimise grasping stability, durable, stable and possess good manufacturability [154].

Silicone elastomers and polyurethanes are classes of materials that are most commonly employed as mechanical skin equivalents because of the similarities in their friction properties with those of the human finger skin [10, 137, 155–157]. Polyurethanes possess excellent tensile strength, high abrasion and chemical resistance [158]. However, they have a greater relative rigidity than human skin. Cabibihan et al. assessed the conformance of silicones and polyurethanes, and compared responses of these materials to that of surface deformation of the human fingerpad [159]. Their results showed that silicone materials conform closest to the human fingertip. Like human skin, silicone elastomers are viscoelastic materials [160].

The widespread use of silicone elastomers for finger replacements and for packaging of tactile sensors [68, 74, 154] can be attributed to their following characteristics:

- Low cost
- Simplicity of fabrication

- Ease of patterning/moulding
- Tunable mechanical properties
- Similarity of compliance and conformance with human skin

Polymethyldisiloxane (PDMS) ($CH_3[Si(CH_3)_2O]_nSi(CH_3)_3$) is a silicone elastomer commonly used in MEMS systems for embedding electronic components, protecting them from mechanical shock and environmental influences and thus prolonging their lifespan [161]. PDMS has also been used in the packaging of tactile sensors [162, 163]. The Young's modulus of PDMS is reported to be close to that of physiological skin [145]. It finds widespread application in the MEMS field because of its following properties [164]:

- Provision of dielectric isolation
- Chemical inertness
- Thermally stability
- Permeability to gases
- Handling and preparation simplicity

The material properties of Sylgard® 184 (Dow Corning Corporation), a commercially available brand of PDMS Silicone Elastomer, are given in Table 5.2 [165].

Dragon Skin® (Smooth-On Inc.) is another commercially available silicone elastomer that has been used in the implementation of artificial fingers [76]. Its properties are given in Table 5.3.

TABLE 5.2: Material properties of Sylgard® 184 [165]

Colour	Transparent
Viscosity (mPa s)	3900
Shore-A hardness	50
Elastic modulus (MPa)	1.8
Thermal conductivity (W/m/K)	0.18
Dielectric constant	2.7
Resistivity (Ωcm)	1.2×10^{14}

TABLE 5.3: Material properties of Dragon Skin® (http://www.smooth-on.com)

Colour	Off-white
Viscosity (mPa s)	23000
Shore-A hardness	10
100% Modulus (MPa)	0.15

Mechanical testing

A sample of PDMS was fabricated using the following process:

- Liquid components Part A and B were mixed in a 10:1 ratio by weight and poured into a cylindrical mould
- The mixture was degassed using an applied vacuum of (29 inches of mercury) for 2-3 minutes
- The material was cured in an oven at a temperature of 100^{o}C for 45 minutes

Fig. 5.7 shows a typical force-displacement behaviour of PDMS for ten load-unload cycles of force controlled (8 N) compression testing (using periodic triangular wave). Like human skin, PDMS exhibited viscoelastic behaviour. Creep and stress relaxation were also observed with an exponential curve fit was applied to the relaxation data (using Matlab Curve Fitting toolbox) as shown in Fig. 5.8.

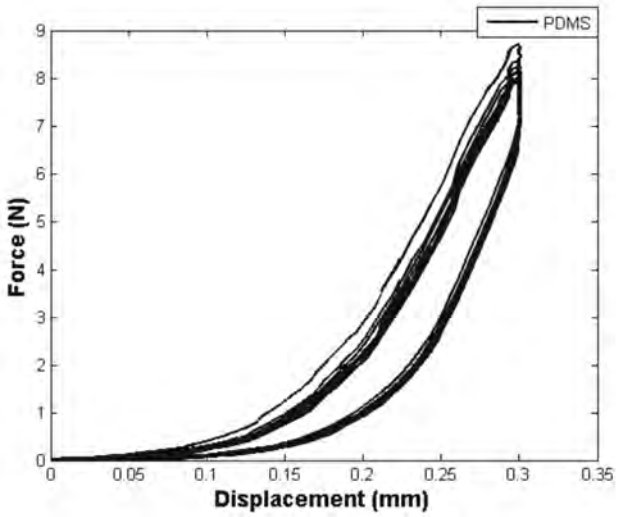

FIGURE 5.7: Characteristic force displacement curve obtained by applying controlled displacements of 0.3 mm to PDMS (10 loading cycles)

The variation in response of PDMS to an applied force of 5 N at different frequencies (or strain rates) is shown in Fig. 5.9. With increasing frequency, there is a decrease in the resultant maximum displacement and % of recovered displacement in the unloading phase. Results are summarised in Table 5.4.

TABLE 5.4: Frequency dependent behaviour of PDMS (Sylgard® 184)

Frequency (Hz)	Maximum displacement (mm)	% of recovered displacement
0.05	0.1	85
1	0.09	81
5	0.08	66

5.3.2 Tissue engineered skin

Tissue engineering is a field which adopts an interdisciplinary approach to develop biological substitutes for restoring, maintaining or replacing biological tissues or organs. It allows the development of a skin-like matrix with mechanical characteristics comparable with that

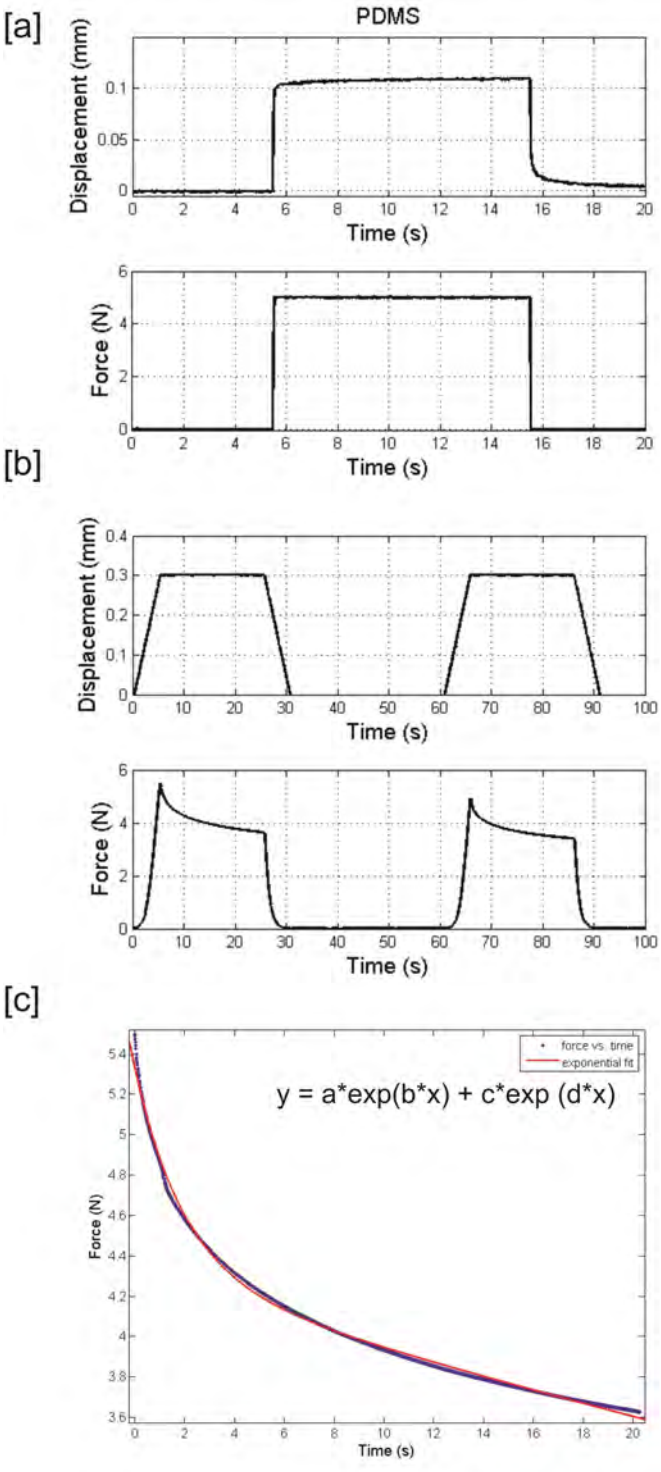

FIGURE 5.8: [a] Creep of PDMS under an applied step load of 5 N for 10 s [b] Stress relaxation of PDMS under constant displacement of 0.3 mm [b] Exponential curve fit of relaxation data a = 1.03, b = -0.51, c = 4.31, d = -0.009

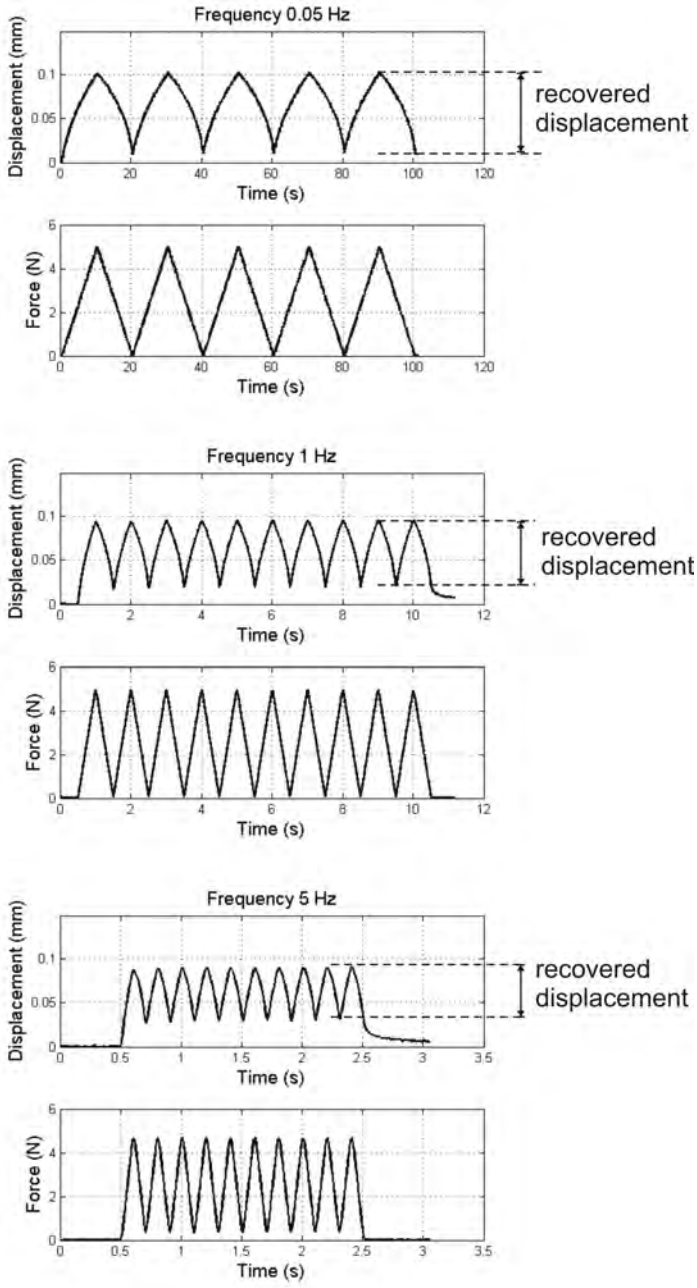

FIGURE 5.9: Change in response of PDMS for applied loading of 5 N under varying applied frequencies of 0.05, 1 and 5 Hz

of the human skin. Although significant progress has been made in tissue engineering skin for treatment of wounds and burns, successful nerve regeneration allowing tactile sensation remains a challenge [149]. With current reports on functional tissue engineered organs, future visions of a fully functional tissue engineered hand are not far fetched. In the meantime, significant efforts are being made in neuroprosthetic devices. These are systems that harness biological neural signals and interface them with prosthetic devices. Implantable neuroprosthetic systems in the visual and auditory domains have already been demonstrated [166]. An example of biohybrid visual prosthesis is shown in Fig. 5.10 [167].

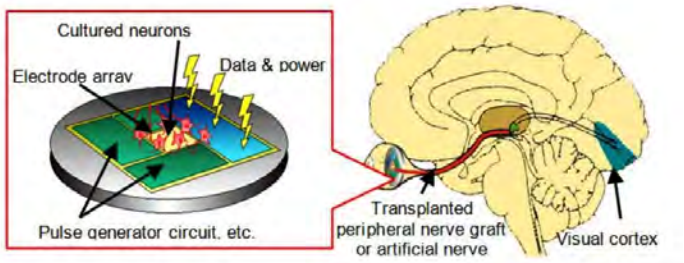

FIGURE 5.10: Biohybrid visual prosthesis [167]

In the touch sensing domain, recently, the CyberHand was reported, which is a prosthetic device designed to interface with the peripheral nervous system and aims to replicate the sensory-motor capabilities of the human hand. The device is controlled by processing efferent nerve (nerves that carry information from the central nervous system to the muscles) signals from nerve endings in the residual stump of an amputee, and sensory feedback from artificial sensors is delivered to the user through the stimulation of specific afferent nerves. Fuelled by such motivation for the development of more natural, human like prosthetics, the concept of combining tactile sensing technology with tissue engineered skin emerges [168]. The development of tissue engineered skin enables the opportunity to provide a substitute

material that closely mimics the properties of natural human skin, however device encapsulation and biocompatibility are issues for consideration.

A general approach for generating tissue engineered products is shown in Fig. 5.11 [169]. Here, isolated cells are cultured and then seeded onto a scaffold which provides mechanical support and promotes structural formation. The cell constructs are further cultivated in bioreactors to provide optimal conditions for organization into a functioning tissue. Once a functioning tissue has been successfully engineered, it is transplanted to restore function [169].

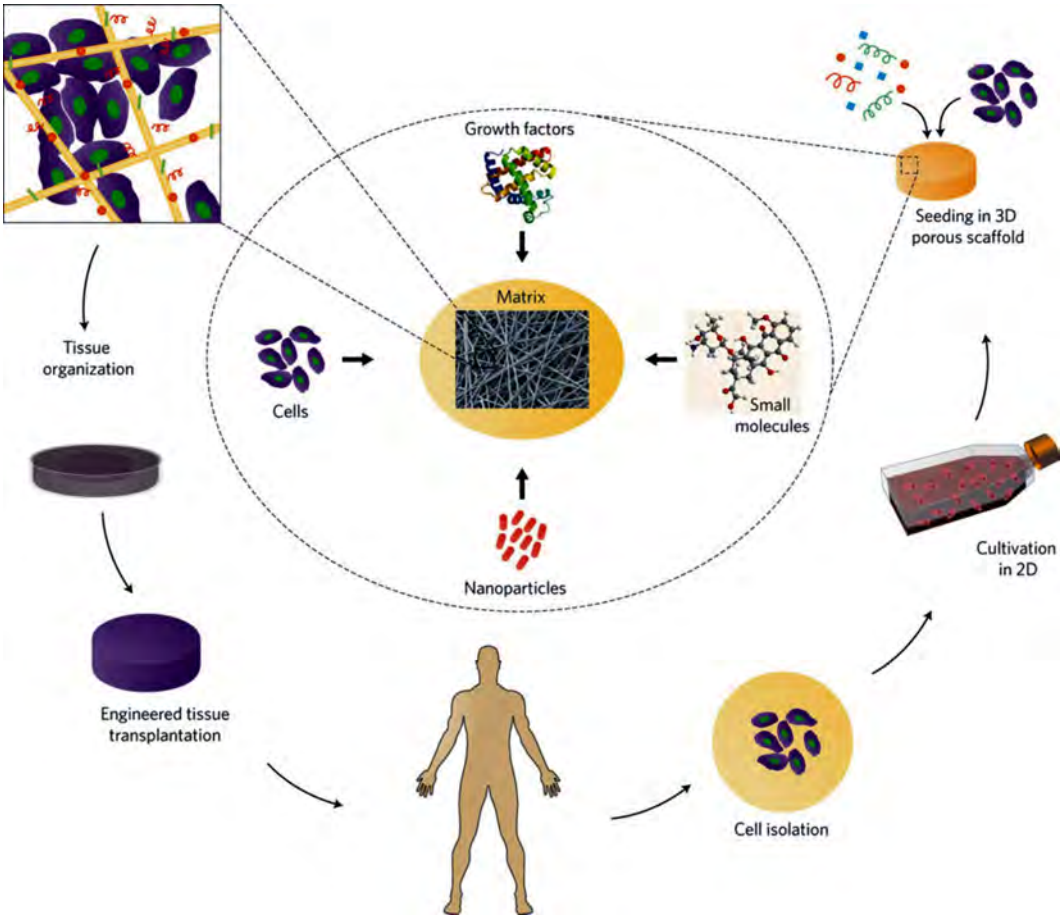

FIGURE 5.11: Typical method for fabricating tissue engineered products [169]

Mechanical testing

To assess its mechanical properties, tissue engineered skin was fabricated (by Nicola Hunt, Biochemical Engineering, University of Birmingham) using the following materials [136, 143]:

- Fibroblasts: These form the dermal layer of skin. They are responsible for producing extracellular matrix and collagen which form the structural framework of animal tissues and provide strength and resilience.

- Keratinocytes: These are the predominant cells of the epidermis which form the impervious surface of skin and primarily function as a barrier against environmental damage, water loss etc. The keratinocytes were obtained from a neonatal rat.

- Alginate (a polysaccharide isolated from brown algae) scaffold: This provides the structural framework for three dimensional tissue formation and nutrients for the cultured cells.

Fig. 5.12 [a] shows a characteristic force displacement response obtained when a triangular waveform with ten cycles of indentations to a depth of 0.3 mm are applied to the skin a rate of 0.6 mm/s. Non-linear curves with a pronounced hysteresis are obtained, which are attributed to a decrease in energy loss in each subsequent cycle.

Stress relaxation of TE skin is shown in Fig. 5.12 [b]. Here the sample was subjected to indentations of 0.3 mm applied at a speed of 0.06 mm/s, held for a period of 30 s and then removed. Fig. 5.12 [c] shows an exponential curve fit (using Matlab Curve Fitting toolbox) applied to the data corresponding to the relaxation period.

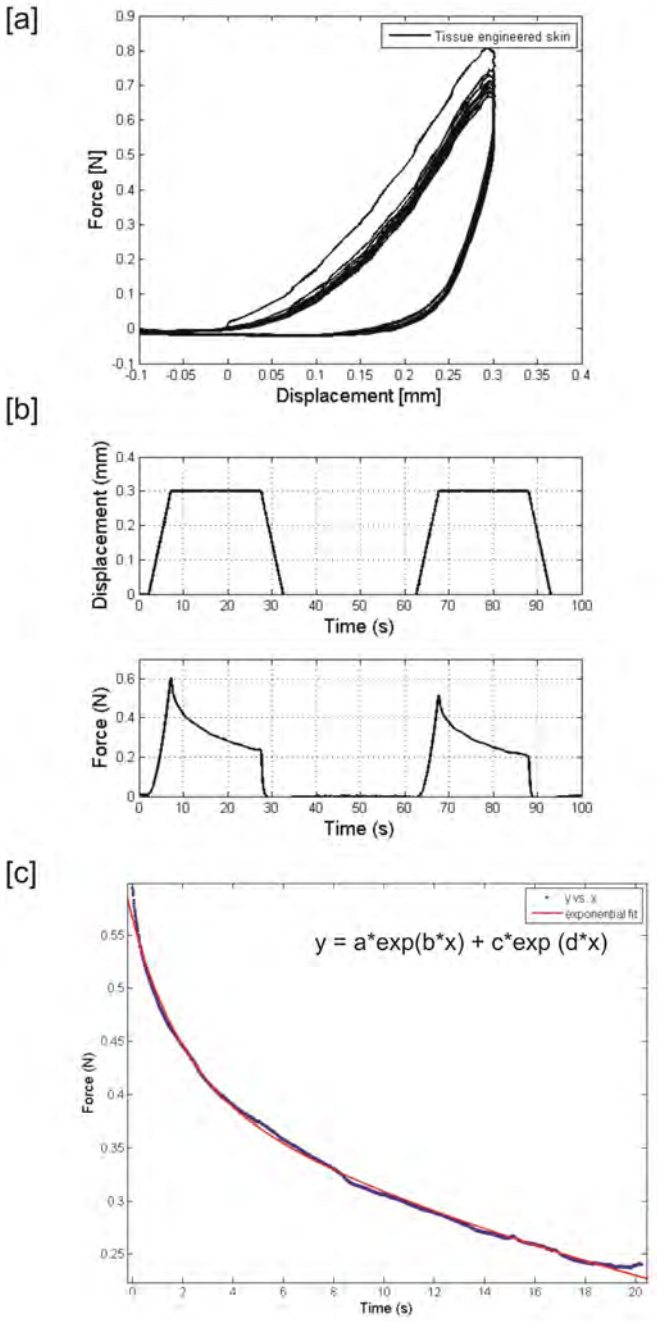

FIGURE 5.12: [a] Characteristic force displacement curve obtained by applying controlled displacements of 0.3 mm onto the surface of the tissue engineered skin (10 cycles) [b] Stress relaxation of TE skin under constant displacement of 0.3 mm [c] Exponential curve fit of relaxation data a = 0.15, b = -0.49, c = 0.41, d = -0.02

5.4 Discussion on materials tested

In the previous section, material testing of biological skin (rat skin), silicone elastomer (PDMS) and tissue engineered skin was conducted. The purpose of the material testing was not to quantify or extract quantitative material parameters but rather to study the patterns of responses of biological and artificial materials when subjected to mechanical stimuli in the range encountered by the human fingerpad during manipulation.

Like human skin, all the material samples tested, demonstrated viscoelastic, time dependent responses. TE skin showed greatest compliance followed by rat skin and PDMS. The stress relaxation data for materials were shown to fit the double exponential function:

$$F(t) = a * exp(b * x) + c * exp(d * x) \tag{5.2}$$

where a, b, c and d are characteristic constants of each material.

This is in agreement with results from a study conducted by Williams et al. where data from indentation experiments on biological skin showed that both indenter tip force and corresponding instantaneous firing rates of SA I afferent neurons in response to ramp and hold indentations of skin fit a double exponential function [170]. The receptors thus fire electrical impulses on the application of stress, the frequency of which subsides during the hold phase of the loading cycle (Fig. 5.13) along with stress relaxation of skin thereby conserving energy [26].

In dynamic testing, the effect of strain rate on stiffness of the materials was assessed. This parameter is important as it determines the highest frequency at which an applied stimulus can be detected by tactile sensors located below the materials. PDMS demonstrated an

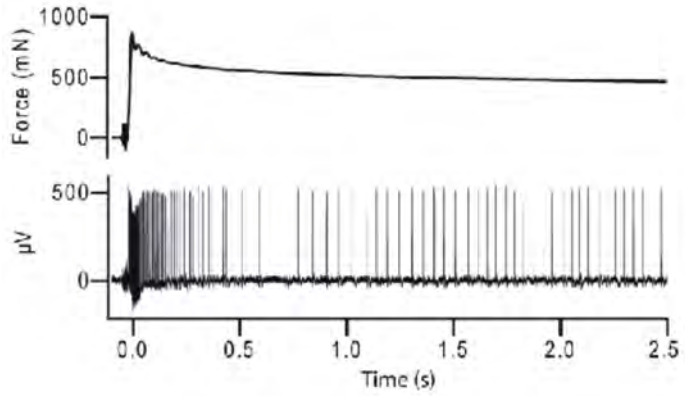

FIGURE 5.13: Experimental results from Williams et al. showing SA I firing rates to ramp and hold indentation of fingerpad [170]

increase in material stiffness with an increasing strain rate with a 20% reduction in maximum displacement when the strain rate was increased from 0.05 Hz to 5 Hz. However, the effect was found to be lower than that seen in the biological skin sample which showed a 60% loss in maximum displacement for the same increase in strain rate.

The % of recovered displacement, which represents the return of the sample to its original state on removal of the load, was also seen to decrease with an increase in strain rate (Table 5.4 and 5.1). However, in PDMS the effect was far less pronounced. This feature impacts on the performance of the tactile sensor as at higher frequencies, the displacement due to the applied mechanical stimulus may not be transferred to the embedded sensors. In this way, the frequency dependent behaviour of the packaging material effects the operational bandwidth of the sensor in dynamic loading. PDMS was found to show more favourable characteristics in this regard in comparison to the tested biological sample.

5.5 Tactile sensor packaging methods

5.5.1 Smooth packaging with Silicone elastomers

To package the MEMS tactile sensors developed in this work Sylgard® 184 (Dow Corning Corporation), a commercially available brand of PDMS Silicone Elastomer was used. To enable a comparison, a single chip was also packaged with Dragon Skin®, the other candidate elastomer. The process used to process both these materials is given in the following.

PDMS was prepared by mixing the two supplied parts A and B in a 10:1 ratio by weight. The mixture was then degassed using vacuum (29 inches of mercury) until the bubbling of the liquid subsided. 105 mg of the PDMS mixture was dispensed into the cavity within the dual in-line package (DIP) onto which the MEMS die was attached. Thus a thin film was formed over the device. It was then cured in an oven at 100^o C for 45 minutes. During the curing process, the chip was mounted upside down to prevent the PDMS from flowing into the 10 μm diameter etch holes of the device. An average packaging thickness of 0.3 mm (measured by using a micrometer) was achieved. A photograph of the packaged sensor is shown in Fig. 5.14.

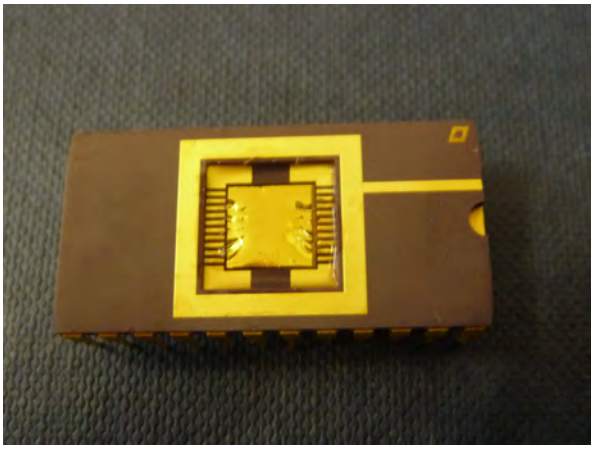

FIGURE 5.14: Packaged sensor

As previously mentioned, a sensing chip was also packaged with Dragon Skin®. The two supplied parts A and B which were mixed in a 1:1 ratio by weight and then degassed using vacuum (29 inches of mercury) for 2-3 minutes. The solution was poured into the cavity within the dual in-line package (DIP) onto which the MEMS die was attached. It was then cured at room temperature for 24 h (as recommended by the supplier). A packaging thickness of 1.7 mm was achieved.

As PDMS has a lower viscosity of 3900 cps [1] compared to Dragon Skin® which has a viscosity of 23000 cps [2], it was easier to produce thin layers of packaging using this material. During the packaging process, a thinner layer is desirable as the thickness of the packaging is proportional to a loss in spatial resolution of the sensors [171].

5.5.2 Fingerprint like packaging

To explore the effects of a fingerprint like topography on the packaging of the tactile sensor (as discussed in Section 5.2.3), a second sensor array was packaged with PDMS that was patterned with parallel ridges. To incorporate the pattern, a silicon mould with rectangular gratings was used. This was fabricated using deep reactive ion etching (described in Chapter 4). The mould was designed to have dimensions equal to that of the cavity of the DIP package used (6.3 mm $\times$ 6.3 mm). This was done to enable easier alignment of the mould during the patterning process. The fabricated grating, shown in Fig. 5.15 had the following features:

- Ridge width of 200 μm
- Groove width of 200 μm

[1] Datasheet from Dow Corning (http://www.dowcorning.com/)
[2] Datasheet from Smooth-On (http://www.smooth-on.com/)

- Groove height of 50 μm

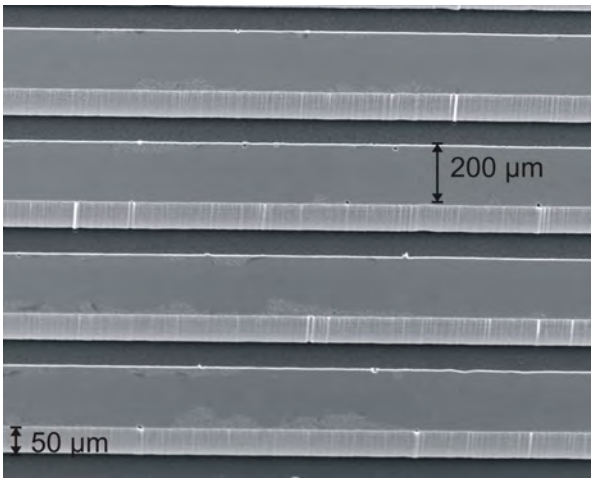

FIGURE 5.15: SEM image of silicon grating used as a mould to pattern the PDMS

The feature sizes were chosen to be of the order of dimensions of the individual sensors. To transfer the above features from the mould to the PDMS packaging, the PDMS solution was first poured onto cavity of the DIP socket housing the sensor. The device was then placed in an oven at 100^o C for 5 minutes to allow partial curing of the PDMS. The silicon mould which was coated with silicone release agent spray was then aligned over the cavity of the DIP socket. The device was then put back in the oven for a further 40 minutes to cure. Following this period, the device was left to cool and the silicon mould gently removed from the packaging.

Using this method, the sensor package was successfully patterned with ridges mimicking fingerprints. Fig. 5.16 shows a photograph of the sensor incorporating a ridged topography packaging.

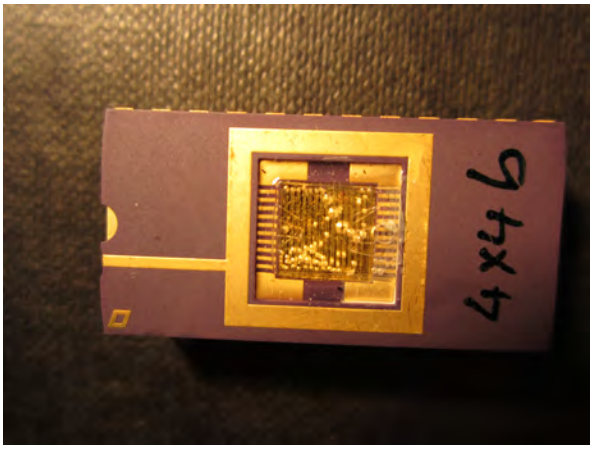

FIGURE 5.16: Sensor packaged with fingerprint like ridges

5.5.3 Tissue engineered skin

For testing the response of MEMS sensors embedded within tissue engineered skin, the sensors were first coated with a 200 nm layer of parylene (poly-para-xylylenes) through a chemical vapour deposition process. This forms a biocompatible barrier which also protects the chip from moisture and corrosive effects of the biological environment. The tissue engineered skin was then directly placed over the sensors for testing as shown in Fig. 5.17. The skin was held in place by surface tension and no adhesive layer was applied. A chip packaged with the tissue engineered skin is shown in Fig. 5.18.

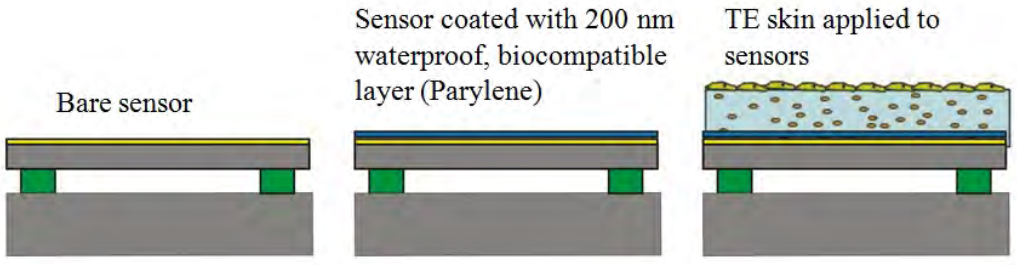

FIGURE 5.17: Process of applying Tissue engineered skin onto sensor surface

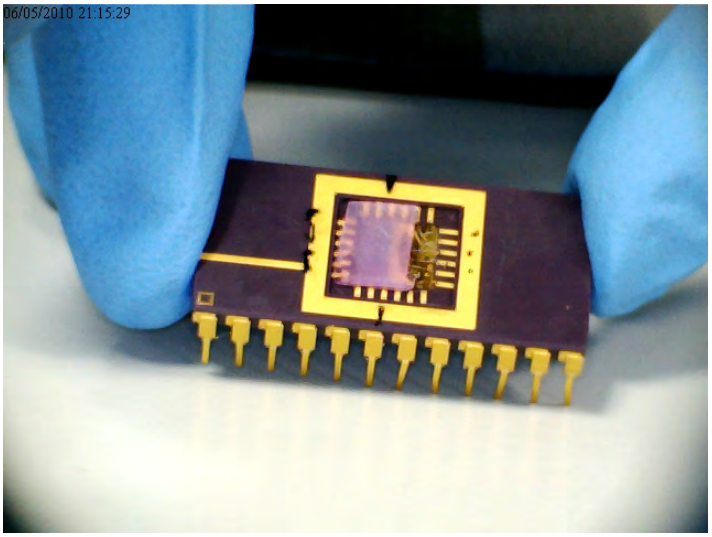

FIGURE 5.18: Tissue engineered skin applied onto sensor surface

5.6 Conclusions

In this chapter, the objectives of artificial skin within which the MEMS sensors can be embedded were given. Following a review of human skin characteristics, the use of skin equivalent materials such as silicone elastomers and tissue engineered skin was discussed. Finally the processes for packaging the fabricated MEMS based sensor array was described. The following three materials were used to form an artificial skin layer within which the sensors were embedded.

1. PDMS was chosen as the most suitable packaging material for the MEMS sensors due to its versatility with regards to its mechanical properties, easier implementation into thin layers as well as the ease of texture patterning. Both, a smooth packaging layer as well as a 'fingerprint' like packaging layer was developed.

2. A single chip was also packaged with Dragon Skin® to enable a comparison to be made between the two elastomers.

3. Because tissue engineered skin is close to human skin in terms of its structural and biological characteristics, a method for successfully incorporating the sensors within tissue engineered skin was described.

6

Characterisation of sensor performance

Contents

Summary This chapter provides a description of the experiments that were conducted to characterise the performance of the fabricated MEMS based sensing device. The demonstrated experimental protocols mimic those conducted in fingertip mechanoreceptor characterisation experiments. A discussion of the results of sensor characterisation is finally presented.

6.1 Introduction

The experiments conducted to characterise the performance of the fabricated MEMS based sensing devices were inspired by methods that have been used to assess the performance of biological tactile sensory afferents [45]. Neurophysiological and psychophysical studies have contributed vastly to an understanding of the functions of mechanoreceptors and mechanisms behind texture perception. Neurophysiological methods involve the use of microneurography techniques (described in Chapter 2) where action potentials emitted by selected nerve fibres in response to applied stimuli are recorded. On the other hand, psychophysical assessments examine the perceptions of human subjects to the applied stimulus.

To characterise individual mechanoreceptor responses, a commonly employed method involves the application of controlled indentations to the fingerpad while simultaneously measuring the associated mechanoreceptive afferent firing rates by microneurography. This allows an assesment of the relationships between parameters of a mechanical stimulus (such as force and displacement) and afferent firing rates. By indenting different locations on the fingerpad, the area of response associated with a single sensory afferent (known as the receptive field of the mechanoreceptor) can also be determined.

Texture perception involves the experience of a number of surface qualities such as microspatial geometry patterns, roughness, smoothness, stickiness, coarseness and graininess [172]. In humans, in addition to cutaneous input, kinesthetic, auditory and visual cues are used in the perception of textures. Currently there is no consolidated agreement in the literature regarding the neural mechanisms underlying tactile texture perception in humans. As early as 1925, David Katz proposed the 'Duplex theory of texture perception' [56]. He hypothesised that tactile texture perception is mediated by spatial cues in the case of coarse

textures and vibrotactile cues in the case of fine textures. In other words, the perception of fine textures was attributed to vibrations generated by the relative movement of skin and the stimulus, whereas coarse textures are perceived on the basis of their geometrical features such as size, shape and distribution of surface elements [57].

In 2000, Hollins and Risner provided experimental data in support of Katz's hypothesis by comparing subject's perceptions of texture with and without movement of the finger across the surface. It was found that fine surfaces that were easily discriminated when moved across the skin became indistinguishable in the absence of movement. On the other hand, coarse surfaces were equally discriminable in both static and dynamic conditions. Thus they concluded that movement significantly enhanced the accuracy of subject predictions. Yoshioka et al. contradictively suggested that the same neural mechanism underlines the perceived roughness of both fine and coarse surfaces; ie. a unified paradigm via the spatiotemporal modulation of the neural activity of SA I afferents [58]. They examined the variation in firing rates of the SA I, RA and PC afferents to varying textures and concluded that variations in the firing rates of SA I afferents accounted for the perception of both, fine or coarse textures. Thus, despite conflicts in the understanding of the actual neurological mechanisms behind texture perception, an established finding is the enhanced discrimination sensitivity obtained as a consequence of relative motion between the finger and the surface. This is substantiated by the fact that during exploratory tasks when detecting textures, humans tend to drag their finger over the surface of interest.

Studies on texture perception to date tend to focus on the perception of roughness. This is the sensation that is induced when the skin passes over a surface that is not uniformly smooth [173]. Previous research conducted on roughness perception used sandpapers of varying grit

size to deliver a range of textures to the fingerpad. More recently, precisely controlled stimuli in the form of rigid linear rectangular gratings of alternating ridges and grooves have been used as moving stimuli to the fingerpad. Different textures are generated by varying the grating characteristics such as ridge width and groove width. While delivering such stimulus to the fingerpad, the responses of the mechanoreceptors and the subject's perceptions have been simultaneously recorded [174–176]. Results from such psychophysical studies have shown that the perception of roughness is directly related to an increase in the groove width [53, 58, 174].

The experimental methods as they are used to determine the characteristics of biological mechanoreceptors, can likewise form a reasonable basis for investigations on the general characteristics and texture discrimination capability of the fabricated MEMS tactile sensing devices. As the sensors were designed to possess properties similar to the ones of their natural counterparts, similar methods and dimensions for the characterisation were chosen. To this end, the following main categories of tests were performed to assess different aspects of sensor performance [177, 178]:

1. Indentation testing to determine general force-capacitance characteristics

2. Spatial mapping of sensor array to assess the spatial response characteristics

3. Surface texture discrimination via the use of periodic gratings and fabrics

6.2 Indentation testing

6.2.1 Experimental set-up and methods

The equipment used for indentation testing was designed by the ARTS Lab, SSSA, Pontedera, Italy. The set-up is shown in Fig. 6.1. It consisted of a loading system incorporating three orthogonal manual micrometric translation stages (A), which allowed the precise positioning of the loading probe. The loading probe consisted of a spherical head having a diameter of 2 mm (C) made of Delrin® (polyoxymethylene), which is an insulating (resistivity of 10^{12} Ohm-m) thermoplastic material exhibiting high stiffness (3 GPa) [1]. A spherical indenter was chosen as it is less likely to cause cracking during indentation and for small plastic deformations, and it has well defined stress fields below the area of contact [179].

The indentation experiments were carried out under displacement control (as allowed by the indentation device). Contact between the probe and the sensor was obtained by a servo-controlled micrometric translation stage (M-111.1, PI, Karlsruhe, Germany) (D), which allowed the position of the probe to be finely controlled in the normal direction. Two orthogonally located cameras were used to position the probe over the required sensing area. In order to measure the force applied to the sensor, a six-component load cell (ATI NANO 17 F/T, Apex, NC, USA) (E) was placed at the interface between the loading probe and the servo-controlled micrometric translation stage.

[1] Product datasheet (http://plastics.dupont.com/)

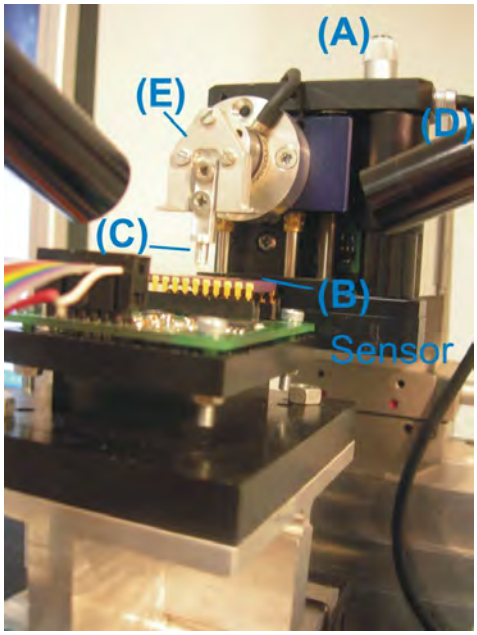

FIGURE 6.1: Experimental setup for indentation testing of the sensors. (A) manual micrometric translation stage (horizontal direction), (B) sensor, (C) rigid spherical probe, (D) servo-controlled micrometric translation stage (vertical direction), (E) ATI load cell

6.2.2 Performance of bare/unpackaged sensors

The indenter probe was aligned over the bare/unpackaged sensor diaphragm and advanced forwards towards the diaphragm until contact between the probe and sensor was achieved. Fig. 6.2 shows the alignment of the probe over an individual sensor. A trapezoidal displacement function was then applied to the probe which consisted of a loading indentation phase, followed by a steady state phase where the probe was held static for a defined period of time, and then an unloading phase at the same constant velocity. The maximum displacement applied to the probe varied between different experimental runs in order to span the working range, and to estimate the force resolution of the devices. Through preliminary tests where the change in capacitance with increasing displacement of the indenting probe was observed, the point of contact of the probe and sensor membrane were established.

In the following, the characterisation of the bare sensor with a clamped rectangular design

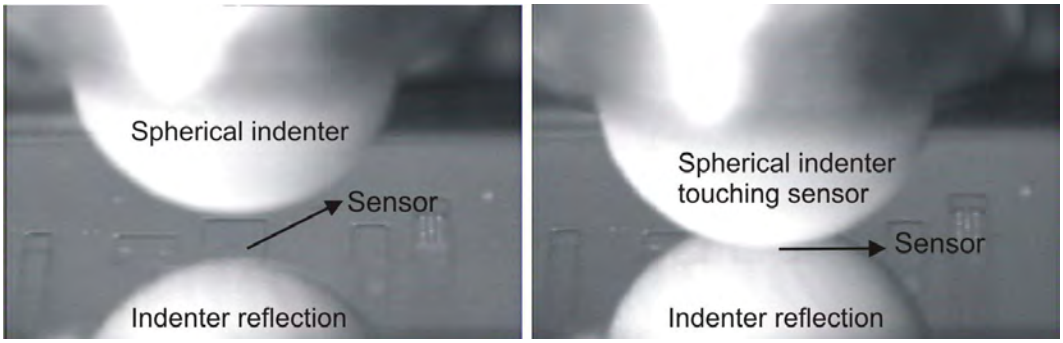

FIGURE 6.2: Photos demonstrating alignment of indenter probe over the bare sensor diaphragm

(Design 2, as introduced in Chapter 3) that was successful fabricated and showed improved yield compared to Design 1 sensors are presented.

Characteristic force vs. capacitance response

The response of the sensor to three cycles of indentations are shown in Figs. 6.3[a] and [b]. Here, the probe was advanced towards the sensor using a constant velocity of 0.34 μm/s for a time period of 5 s. It was then held stationary for a period of 5 s and then advanced away from the sensor at the same velocity. Load - unload indentation cycles were automated within each session using macros for commanding the servo-controlled translation stage in order to observe and demonstrate the repeatability of sensor response.

The upper subplot of Fig. 6.3[a] displays data obtained from the capacitance readout system and the lower subplot is the superimposition of the raw measurements by the load cell and data obtained by applying a Butterworth filter having a cut-off frequency at 1 Hz. The plotted change in capacitance, ΔC, is the result of a differential reading between sensor and reference capacitor. It is obtained by deducting the values of both initial sensor capacitance and reference capacitance from the current sensor capacitance at each time instance. Therewith, any parasitic effects due to capacitive coupling are eliminated. Results show that

the sensor output follows the patterns of the applied load. The devices were indented to generate a maximum force in the order of 25 mN above which the capacitance readout saturated. Fig. 6.3 [b] shows the non-linear relationship between applied force and capacitance change. During this test, the maximum displacement of the diaphragm was determined to be 1.7 μm (0.34 μm/s (velocity) $\times$ 5 s (time of loading).

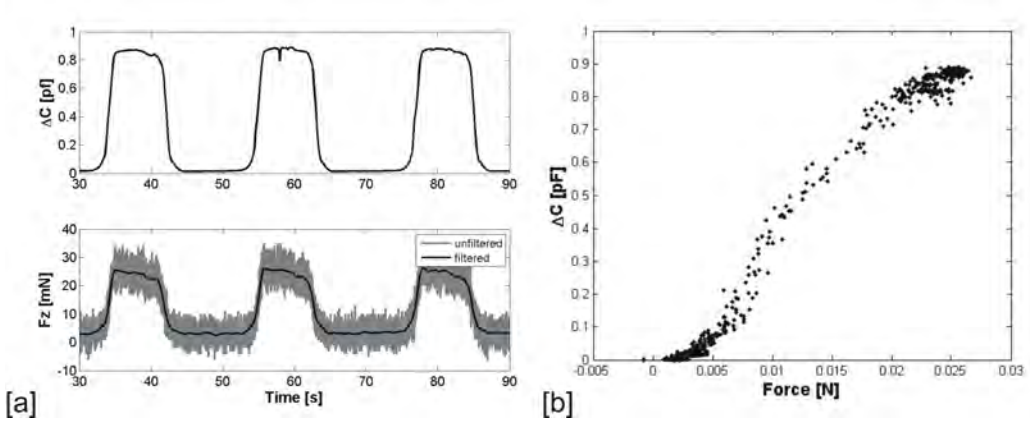

FIGURE 6.3: [a] Upper traces: Response of the bare sensor to three load-unload indentation cycles applied with a spherical probe under position control. Lower traces: unfiltered and filtered indentation force measurements by the used commercial load cell. [b] Change in capacitance vs force ΔC

Fig. 6.4 which was generated by overlapping replicated indentation cycles, shows good repeatability of data from the sensor.

Force resolution

To explore the lowest force that is detectable by the sensor, decreasingly smaller indentations were applied to the sensor, until a change in capacitance of approximately 10 fF was observed. The results are shown in Fig. 6.5.

The changes in the output signal of the sensor clearly followed the applied indentation pattern. However, it was not possible to view the profile of forces as the commercial load cell was unable to resolve forces applied at this scale and therefore did not represent the applied

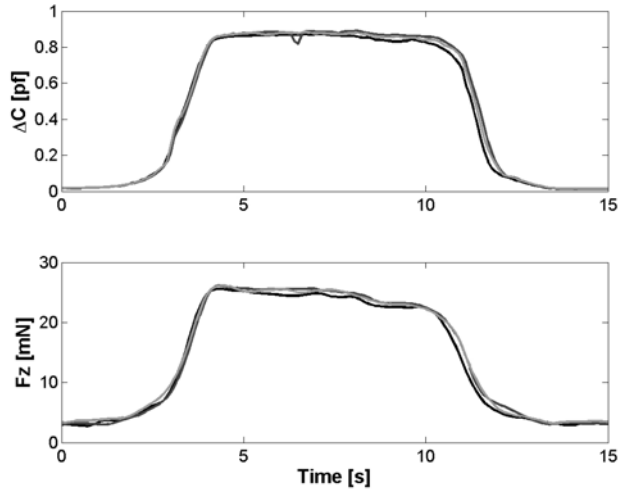

FIGURE 6.4: Upper traces: Response of the bare sensor to repeated and overlapped load-unload indentation cycles applied with a spherical probe under position control. Lower traces: repeated and overlapped filtered indentation force measurements by the used commercial load cell

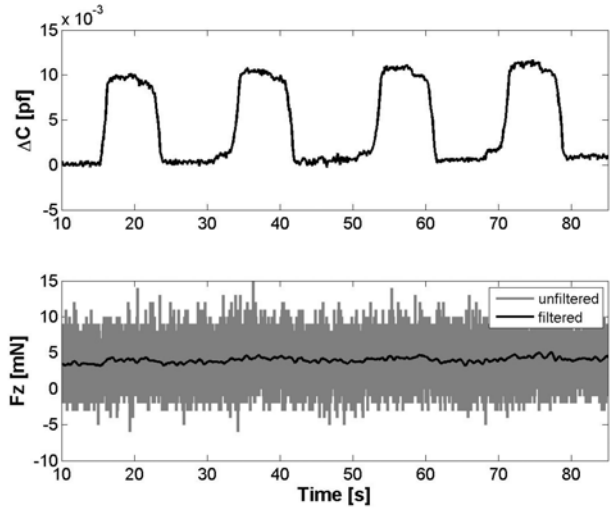

FIGURE 6.5: Experimental results on force-resolution correlation. Upper traces: response of a sensor to three subsequent load-unload cycles using small indentations. Lower traces: Indentation force which did not represent the indentation cycles

indentation profile. The sensor demonstrated a resolution in the sub mN scale.

Temporal resolution

To assess the sensor response to short impulses of mechanical stimuli, three subsequent stimuli, each having 0.2 s pulse width were applied to the sensor diaphragm via the indentation probe. Testing at shorter stimulus time periods was limited by the probe velocities attainable using the current instrumentation, and the sampling frequency of the signal acquisition electronics. Fig. 6.6 shows the sensor response to such stimuli with clear peaks in sensor output corresponding to the applied stimuli. For the given acquisition frequency, no significant response delay between the force stimulus and the change in capacitance ΔC is observed.

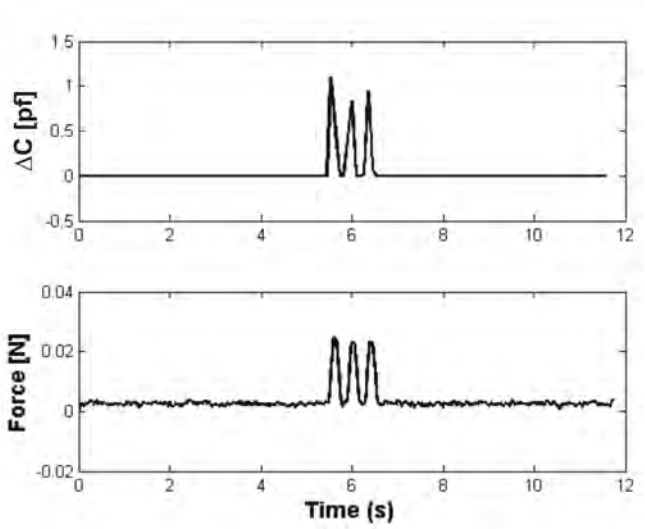

FIGURE 6.6: Upper traces: Response of a sensor to three fast load-unload indentation cycles. Lower traces: indentation force

Effect of diaphragm dimensions

In order to demonstrate the effect of variation in sensor diaphragm dimensions on device sensitivity, indentation testing (3 cycles) was conducted on a sensor incorporating a smaller

sensing diaphragm in comparison to the previously tested sensor. The smaller sensor had a clamped diaphragm with dimensions of 150 $\times$ 150 μm^2. In order to compare the responses of both sensors, indentation tests were carried out where each sensor was indented to a maximum force of approximately 7 mN. Testing results for the larger and smaller diaphragm sensors are shown in Fig. 6.7 [a] and [b] respectively.

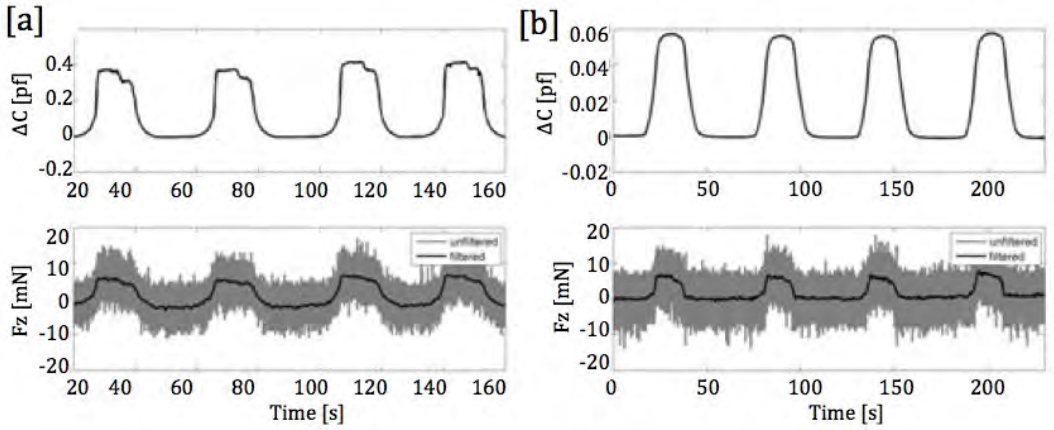

FIGURE 6.7: Effect of sensor diaphragm dimension on sensitivity [a] Response of sensor with dimensions of 300 $\times$ 200 μm^2 (larger diaphragm) to four indentation cycles, [b] Response of the sensor with dimensions 150 $\times$ 150 μm^2 (smaller diaphragm) to four indentation cycles. Upper traces show sensor outputs and lower traces show the unfiltered and filtered indentation force measurements by the used commercial load cell

The sensor with a smaller diaphragm showed an average sensitivity of 8.1 fF/mN for the experimented force range of 7 mN. In comparison, the sensor with larger diaphragm showed an average sensitivity of 53.3 fF/mN for the same experimented force range, which is about an order of magnitude higher.

6.2.3 Performance of packaged sensors

As described in Chapter 5, the sensors were packaged with materials whose function was to act as a protective and load transmitting skin-like layer. To characterise the packaged devices,

the indentation probe was aligned over a single sensor, and as previously described, indentation cycles were applied to the sensor. The position of the centre of the sensor diaphragm was located by conducting preliminary indentation experiments until the region corresponding to the highest magnitude of sensor output was identified.

PDMS packaged sensor

The response of the PDMS packaged sensor to three indentation cycles (each containing a load, a hold and an unload phase) are shown in Fig. 6.8. Here, the probe was advanced towards the sensor using a constant velocity of 20.6 μm/s for a time period of 5 s. It was then held stationary for a period of 20 s and then advanced away from the sensor at the same velocity. Load - unload indentation cycles were automated within each session using macros for commanding the servo-controlled translation stage in order to observe and demonstrate the repeatability of sensor response.

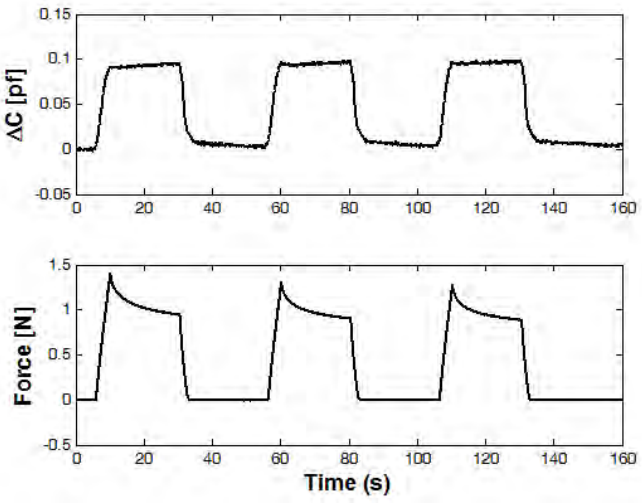

FIGURE 6.8: Upper traces: Response of the PDMS packaged sensor to three load-unload indentation cycles applied with a spherical probe under position control. Lower traces: Indentation force measurements by the used commercial load cell

Results show that the sensor output corresponds to patterns of applied load. During

the hold phase of the indentation cycle, the measurements from the commercial load cell demonstrated stress relaxation of the PDMS packaging material. The sensor outputs however, increased slightly (maximum of 4 fF i.e 4.1% of sensor output change). This effect is hypothesised to be as a result of the redistribution of PDMS material in the region surrounding the indenting probe as a result of compression of the material. An average sensitivity of 0.068 fF/mN over the tested force range of 1.4 N was experimentally determined.

To assess the range of the device, the indentation probe was advanced towards the sensor in steps of 6 μm until capacitance readout saturated. The range was determined to be 1.6 N (Fig. 6.9).

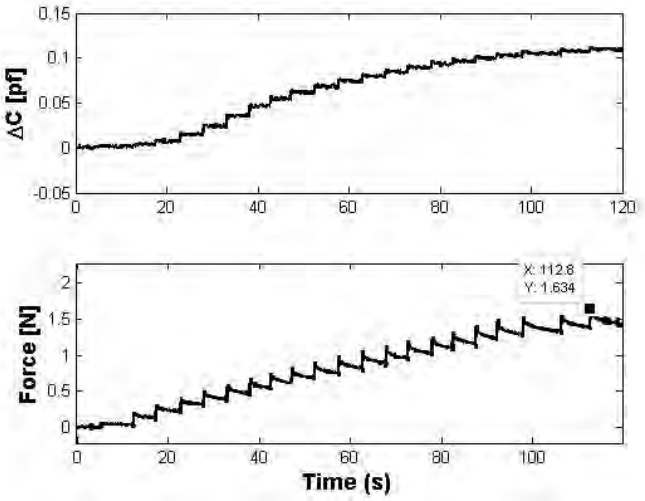

FIGURE 6.9: Force range experimental results for packaged sensor. Upper traces: response of a sensor to increasing applied indentation steps. Lower traces: indentation force

To determine the lowest applied force detectable by the packaged sensor, smaller indentations were applied to the sensor until a change in capacitance of ≈10 fF was observed. Results, shown in Fig. 6.10, demonstrate that the packaged sensor allows a force of ≈ 100 mN to be easily resolved. This test also demonstrated that the packaged device was able to respond to quick mechanical impulses of pulse width 0.5 s.

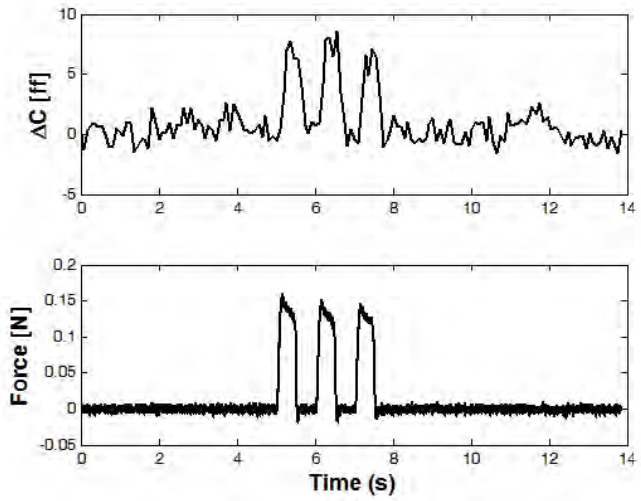

FIGURE 6.10: Force resolution experimental results for packaged sensor. Upper traces: response of a sensor to three subsequent indentation cycles using small indentations. Lower traces: indentation force

Dragon Skin® packaged sensor

The response of the sensor packaged with Dragon Skin® to three indentation cycles (each containing a load, a hold and an unload phase) are shown in Fig. 6.11[a]. As compared to the results for the PDMS packaged sensors, a significant different signal in capacitance change is obtained for a similar force stimulus. An average sensitivity of 0.010 fF/mN over a force range of 2 N was calculated. During the hold phase of the indentation cycle, significant creep was observed, where under the application of a constant force, the sensor output (ΔC) continued to increase. Further during the unloading phase, the sensor exhibited a time delay in returning to zero/steady state conditions. Response of these sensors to impulses with a 2.5 s period are shown in Fig. 6.11[b]. Here, the applied indentation cycles are well represented by the sensor output signal.

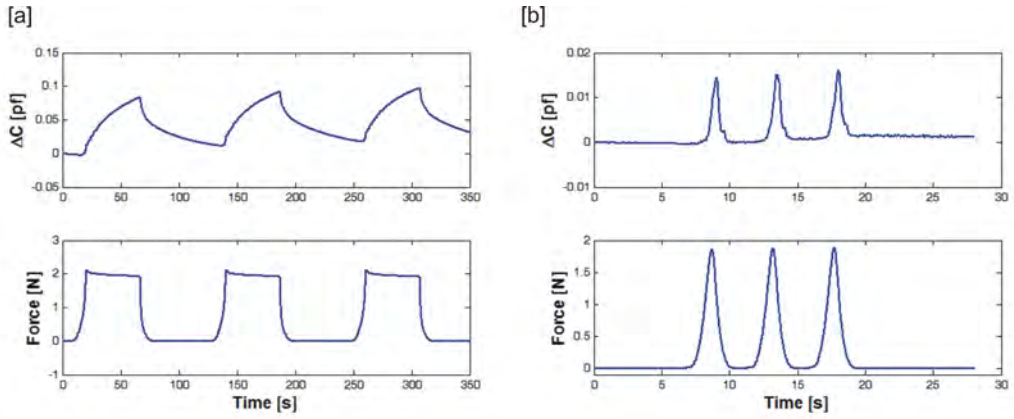

FIGURE 6.11: [a] Upper trace: Sensor response to three load-hold-unload indentation cycles, Lower trace: Applied load [b] Upper trace: Sensor response to three load-unload impulse indentation cycles, Lower trace: Applied load

Tissue Engineered Skin packaged sensor

The response of the sensor embedded underneath tissue engineered skin (2 cm thick) to three indentations with a 1 s period is shown in Fig. 6.12. Sensor output increases with increasing indentation force and vice versa. An average sensitivity of 0.09 fF/mN was calculated.

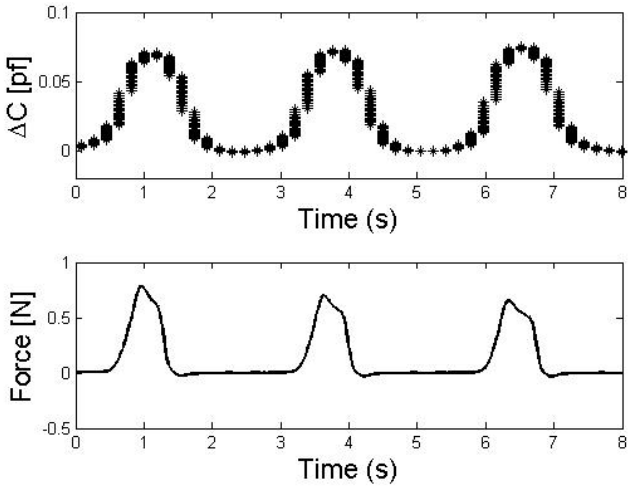

FIGURE 6.12: [a] Upper trace: Response of sensor embedded within TE skin to three load-hold-unload indentation cycles, Lower trace: applied load

6.3 Spatial mapping of sensor array

As discussed in Section 3.6, the implementation of an array of sensors enables the estimation of spatial characteristics of a contacting surface. By analysing the responses of all sensors in an array, information can be obtained on the applied stimulus intensity and its location with respect to the sensors. This is allowed by first conducting preliminary tests to measure the responses of the sensors in an array to known stimuli, and identifying the features of output response characteristics. In the following sections, two main experiments that were carried out to establish the responses of the sensors in an array are described. Firstly, the response of adjacent sensors in an array to local applied stimulus was examined to assess the area of influence of each sensor, and to establish the pattern of output responses due to stimuli applied at spatially varying locations with respect to the centre of each sensor. Secondly, the response to a lateral sliding stimulus applied across the sensors within the array was examined. Based on the improved performance of PDMS packaged sensors over Dragon skin® packaged sensors, the following experiments were all conducted on the sensors packaged with PDMS.

6.3.1 Normal loading at spatially varying locations

In order to map the spatial response field of the packaged sensors, indentations were applied at fixed positions (spaced 200 μm apart) along the horizontal axis of the sensing array. The response of three sensors (S1, S2 and S4) within an array to increasing forces (generated by indentation testing as described in Section 6.2) at each position is shown in Fig. 6.13.

The area over which a response from the sensor is elucidated, also known as the receptive field of each sensor, is seen to increase with the indentation depth. This is demonstrated by

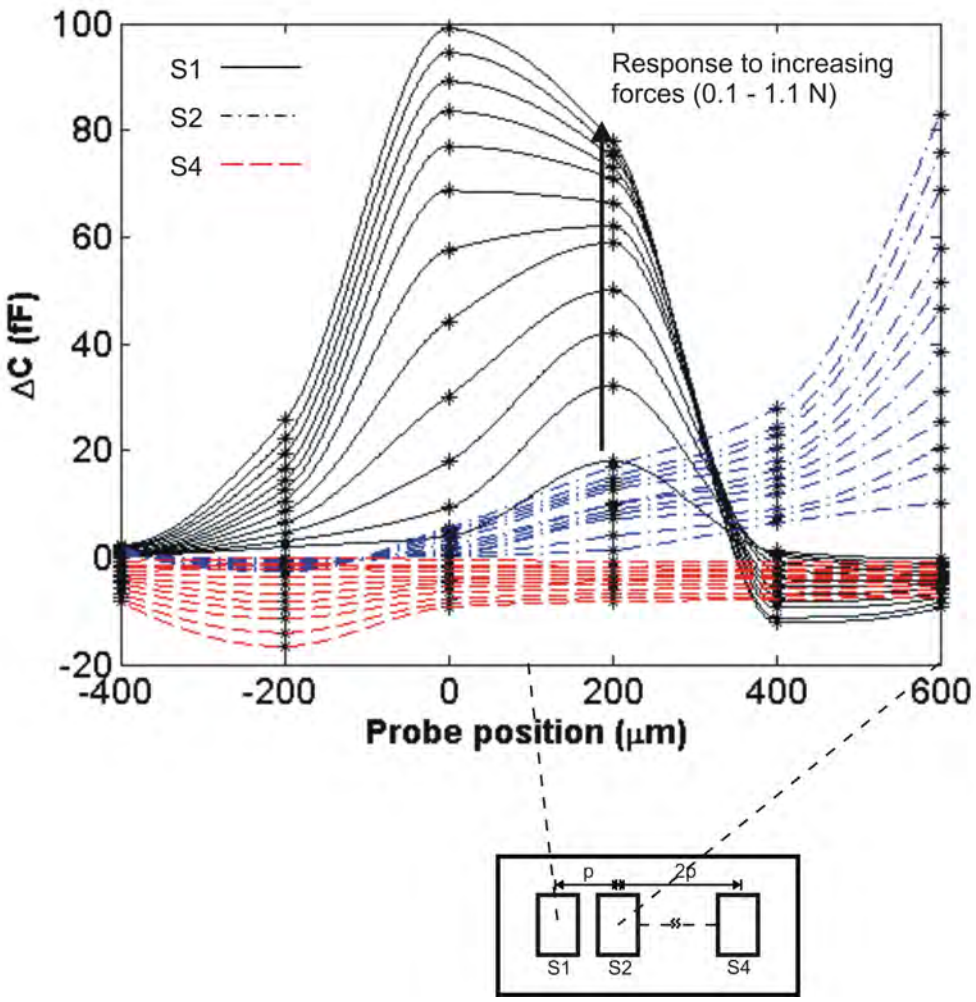

FIGURE 6.13: Response of sensors S1, S2 and S4 in an array to normal indentation via spherical probe at six positions located 200 μm apart. Centre-centre distance between S1 and S2 is 570 μm, which corresponds with experimentally deduced values

the widening of the response curve with increasing force (from 0.1 to 1.2 N) as seen in Fig. 6.13. The location where the greatest magnitude of change in capacitance (greatest force sensitivity) was obtained corresponds to the centre of the diaphragm. The distance between regions of maximum sensitivity for two adjacent sensors should correspond to the centre−to−centre distance between them (570 μm). Approximate locations of diaphragm centres of each sensor were deduced from the results as illustrated in Fig. 6.13. These were found to correlate with the expected distances based on the design of the array.

A negative response from a sensor was observed when applying indentations to locations at certain fixed distances (corresponding to the edges of the sensing diaphragm) away from the sensor itself. The effect was also observed in Dragon Skin packaged sensors (Appendix B). This effect is assumed to be related to local changes to the profile of PDMS that occur during indentation. When applying indentations to polymers constrained by a rigid substrate, it has been shown that the indenting probe causes movement of the polymer in the radial direction, perpendicular to the indenter axis [180]. The excess material, which is displaced from the region between the probe and the rigid silicon substrate, in turn pushes the surface of the polymer coating upwards in an annular region surrounding the probe tip, as there are no constraints to the free surface to restrict this movement. This upward displacement of material subsequently influences the forces imposed on the sensor, generating an inverse response. Due to the imposed assymetry in the signal, this inverse response is beneficial in identifying the position of the stimulus with respect to the sensing units.

6.3.2 Lateral sliding stimuli

To assess the response of the sensor array to a laterally moving stimulus, a nanotribometer (CSM Instruments) was employed. This device was used because of its ability to apply a precisely known force and to operate in linear mode where an indenting probe can scan along a linear track. Using the nanotribometer, a spherical probe with a diameter of 2 mm was indented into the surface of the sensor, generating a force in the order of 400 mN. It was then laterally displaced across the surface to span all sensor units within the device array. Experimental runs were carried out at three programmed probe scan velocities of 2 mm/s, 0.65 mm/s and 0.09 mm/s (as allowed by the nanotribometer).

Spatio-temporal plots of three sensor outputs (S1, S2 and S3) in response to the aforementioned stimuli are shown in Fig. 6.14. The strongest sensor response (peak output) corresponds to the time instance when the probe is directly over the centre of each sensor. Δt_1 represents the time period between peak output signals from two sensors S1 and S2 which are separated by a distance p apart. Similarly, Δt_2 represents the time period between peak output from sensors S2 and S3, which are separated by a distance of $2p$.

By multiplying the time period between the occurrences of peak outputs from each sensor (Δt_1 and Δt_2) with the probe velocity, the distances across which the peak outputs are generated can be estimated (Table 6.1). As expected, this was found to correlate with the centre-to-centre distance between individual sensing units (570 μm).

To estimate the region over which the applied stimulus generates a sensor response, the time interval for a single output signal (Δt_3) is multiplied with the probe scanning velocity. For the applied scan direction, an average receptive field of 1.3 mm was calculated (Table 6.1).

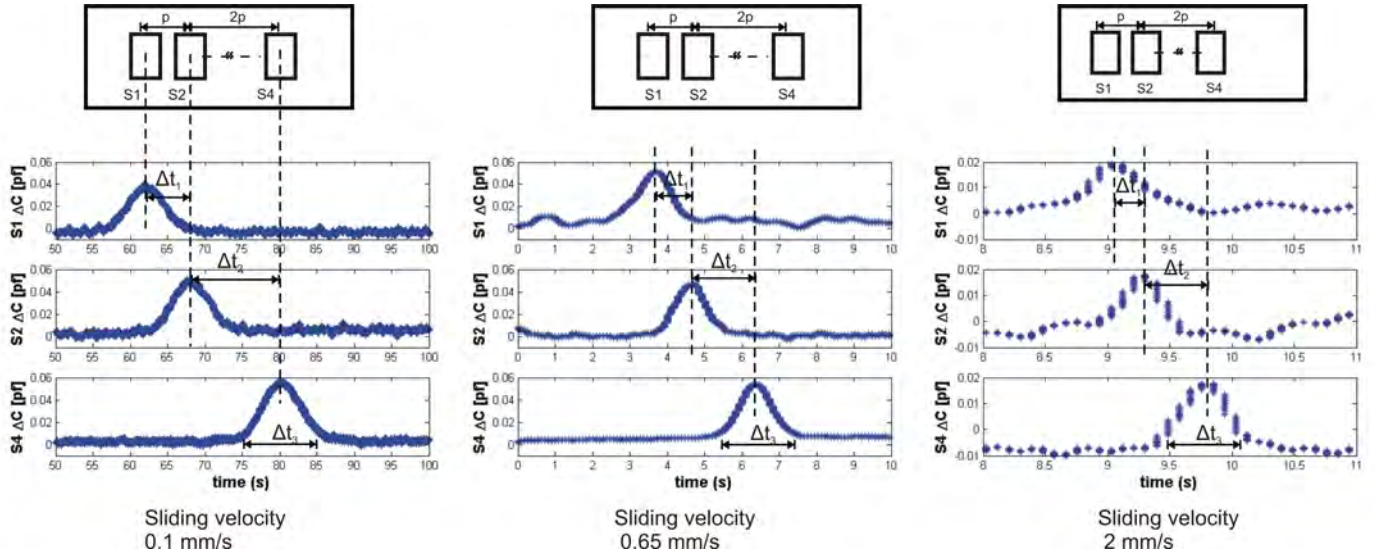

FIGURE 6.14: Spatio-temporal event plot showing response of sensors in an array located at distances p and 2p apart to lateral sliding stimulus via spherical probe displaced at velocities of 0.1 mm/s, 0.65 mm/s and 2 mm/s

TABLE 6.1: Summary of results from sliding tests

Velocity v (mm/s)	Δt_1 (s)	Δt_2 (s)	Δt_3 (s)	Pitch (S1-S2) (mm)	Pitch (S2-S4) (mm)	Receptive field (mm)
0.1	5.8	12	11	0.580	1.2	1
0.65	0.9	1.7	2	0.585	1.105	1.4
2	0.27	0.55	0.7	0.54	1.1	1.5

6.4 Texture recognition

To evaluate the capability of the sensors to differentiate between different types of textures, their responses to gratings of varying periodicity and fabrics varying in weave patterns were explored. Gratings of alternating ridges and grooves are often used in neurophysiological experiments to study humans perceptions of texture. Rectangular gratings (Fig. 6.15) of varying spatial periodicities were designed for this purpose and were manufactured (by Satoshi Endo at the Department of Psychology) using Multi Jet Modeling (MJM) technology [181]. The ridge height was maintained constant while the groove width was varied for each of the gratings.

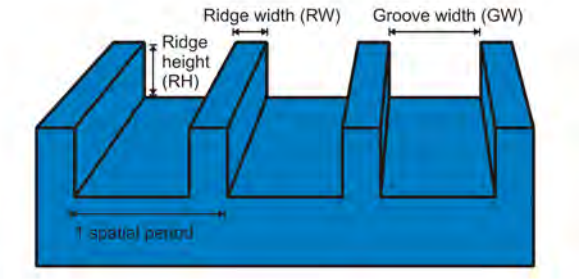

FIGURE 6.15: Schematic of a rectangular grating depicting its ridge width (RW), ridge height (RH), groove width (GW) and spatial periodicity (λ

6.4.1 Discrimination of gratings

To investigate the sensor's capability to discriminate between gratings, two main protocols were employed:

1. Administering textures statically to the tactile sensor surface

2. Lateral movement or dragging of textured surfaces across the tactile sensor surface

using controlled velocities and forces

Static indentation of gratings: Experimental set-up

Two gratings (fine and coarse) were individually indented onto the surface of the sensor to generate a force in the order of 400 mN. The experimental set-up is shown in Fig 6.16 and the geometrical specifications of each grating are given in Table 6.2.

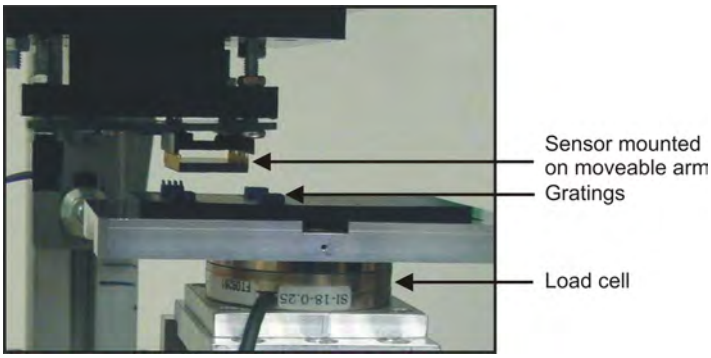

FIGURE 6.16: Experimental set-up showing sensor chip and gratings mounted on dynamic platform to allow tangential sliding of gratings across sensing surface

TABLE 6.2: Specification of gratings used for static indentation experiments

Property	Grating 1 (fine)	Grating 2 (coarse)
Ridge width (μm)	100	400
Groove width (μm)	380	1000
Spatial periodicity λ (μm)	480	1400
Ridge height (μm)	400	400

To deliver the stimulus to the sensors, a custom built mechatronic platform/dynamic platform (developed by ARTS Lab, SSSA, Pontedera, Italy), which allowed two degrees of freedom of movement was used. The gratings were mounted to the moving arm and applied forces were recorded via a commercial ATI load cell. The gratings were indented onto the sensor surface for a period of about 10 s and then removed.

Static indentation of gratings: Results

Results of the static indentation tests using Grating 1 (fine) and Grating 2 (coarse) are shown in Figs. 6.17 [a] and [b], respectively. Schematic figures of the sensor array and gratings are also shown, representing estimated locations of the grating ridges with respect to the individual sensors. Those estimates were based on the response of each of the four sensors in the array as given.

The output of the sensor array to Grating 1 (fine) (Fig. 6.17 [a]) show a maximum response by Sensor 3 (S3), followed by Sensor 2 (S2). The greater response by S3 is most likely due to its more central positioning of the indenting ridge with respect to the sensing diaphragm. Negative responses to the grating ridge indentation are shown by Sensors 1 and 4. This is attributed to the position of the ridge with respect to these sensor diaphragm and is consistent with the results in Section 6.3.1 (Fig. 6.13). There, a negative sensor output was obtained when a rigid probe indented the packaged sensor surface at locations corresponding to regions at the extremities of the sensing diaphragm.

Fig. 6.17[b] shows the output of the sensors to Grating 2 (coarse). Here, Sensor 3 (S3) shows a response to the indentation of the grating. Due to the larger ridge period, no significant variation in response is obtained from the remaining three sensors.

Dynamic/ lateral movement testing

To assess the discrimination of gratings using a dynamic protocol, Gratings 1 and 2 were tangentially displaced across the sensor array surface using the experimental set−up described in Section 6.4.1. The sensor array was brought into contact with the tactile stimulus (each grating) and a double ramp sliding movement (each having a distance of 5 mm) was applied

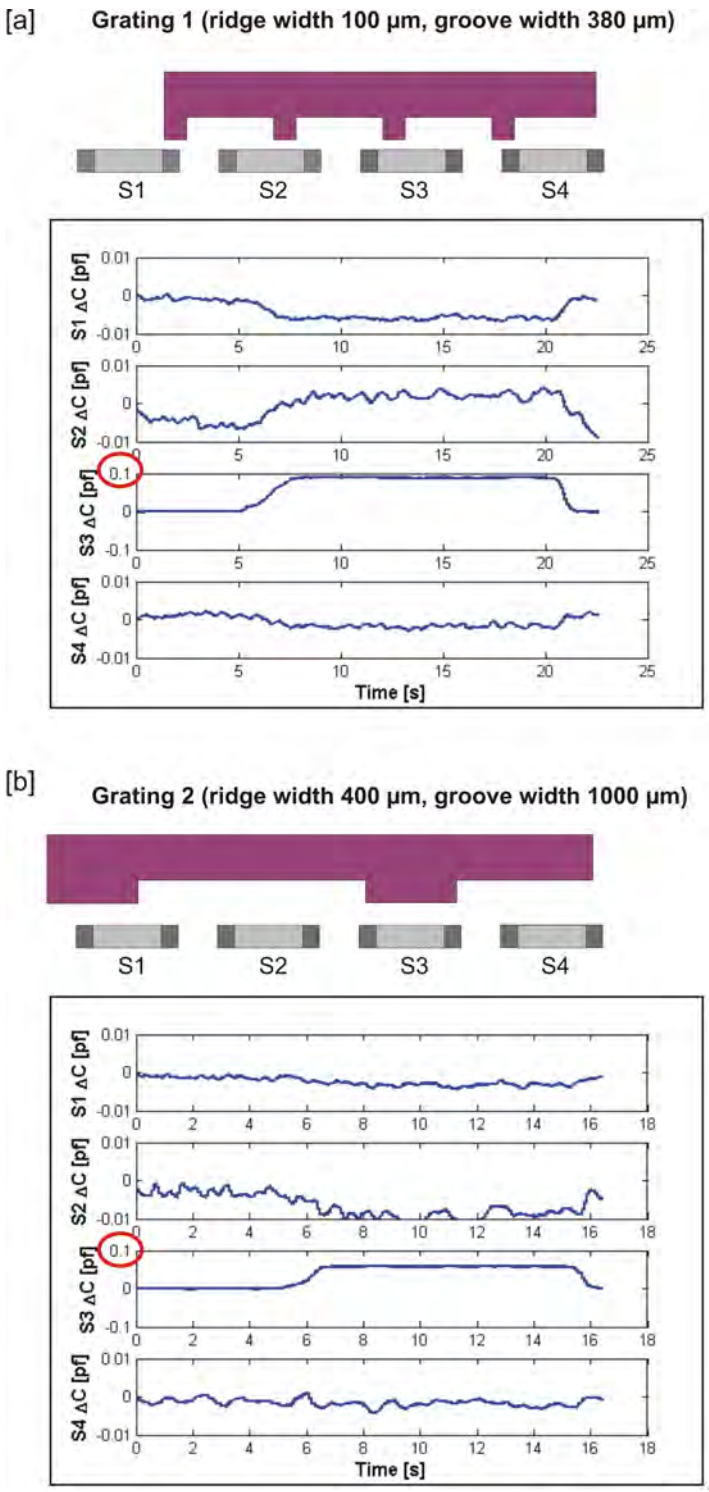

FIGURE 6.17: Typical result trace showing forces on sensor and change in capacitance (pF) recorded from 2 adjacent sensors S1 and S2 in response to static indentation using Grating 1 [a] and Grating 2 [b]

to the array. Multiple experimental runs were carried out varying the applied sensor-stimulus contact forces (10 mN, 100 mN and 200 mN); and sliding velocities (0.2 mm/s, 0.5 mm/s, 1 mm/s and 2 mm/s). Both force and sensor output data were recorded following loading of the sensors with the above mentioned contact forces in order to allow the minor fluctuations in contact forces (due to relative motion of the gratings) to be visualised. The maximum applied velocity was limited by the acquisition frequency of the electronic signal processing system. The protocol of these experiments imitate 'passive-touch' neurophysiological experiments, where textures are moved across human fingertips and tactile peripheral nerve responses and human perceptions of the stimulus are recorded.

Results showing the response of two sensors S2 and S4 within the array to stimuli applied through Gratings 1 and 2 are shown in Fig. 6.18 and Fig. 6.19 respectively. Additional plots obtained for each experimental run are given in Appendix C. Sensor outputs are seen to follow patterns of loading, applied through the gratings. The sensor signal outputs displayed peaks corresponding to peaks in forces which represented applied loading via ridges of the gratings. The plots also show force peaks for which there are no corresponding sensor output peaks. This is because at that given time instance, movement of the grating is beyond the sensing area of the device as depicted in Fig. 6.20.

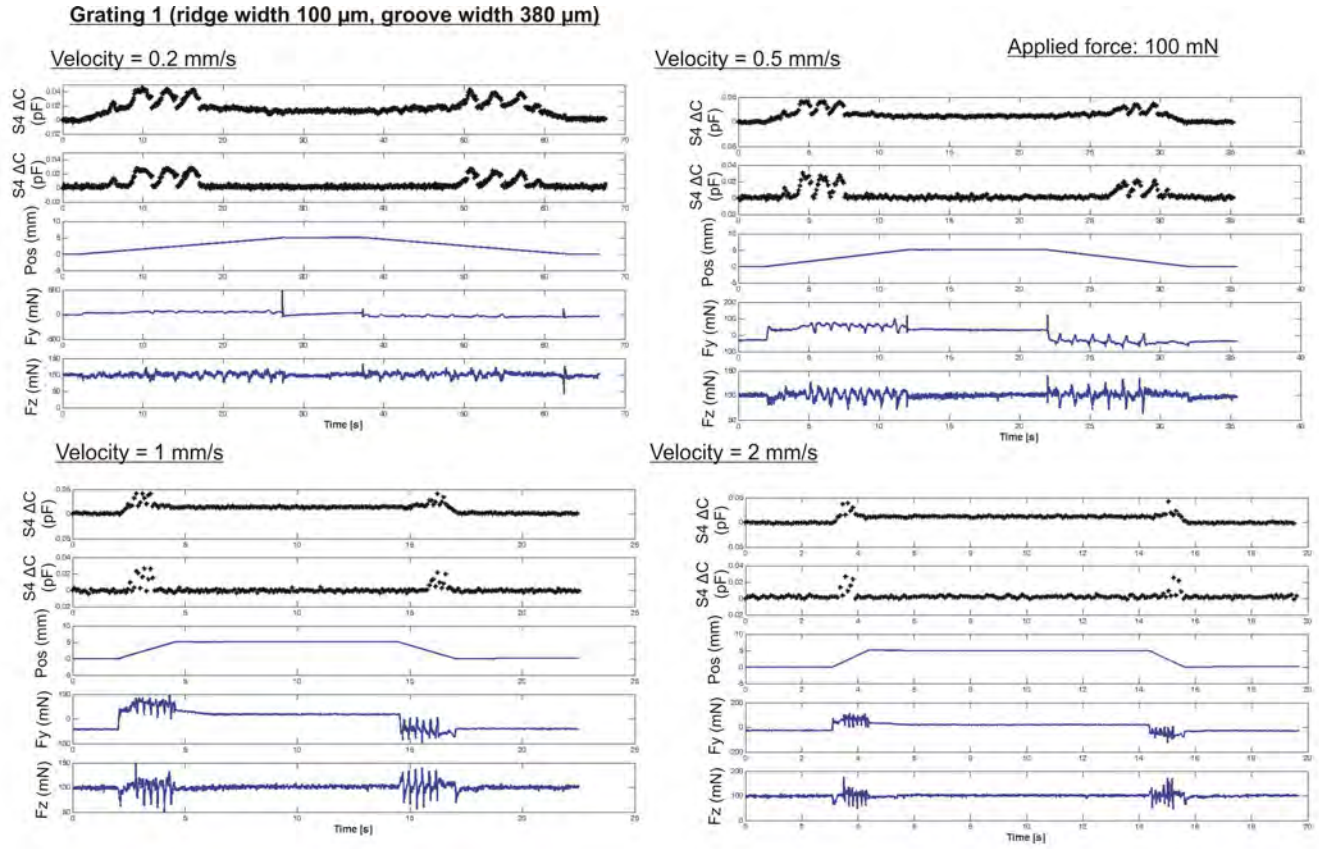

FIGURE 6.18: Typical response of two sensors S2 and S4 to Grating 1 (fine grating) at an applied contact force of 100 mN. Traces show the sensor outputs, position data and forces (F_y and F_z) applied through the grating

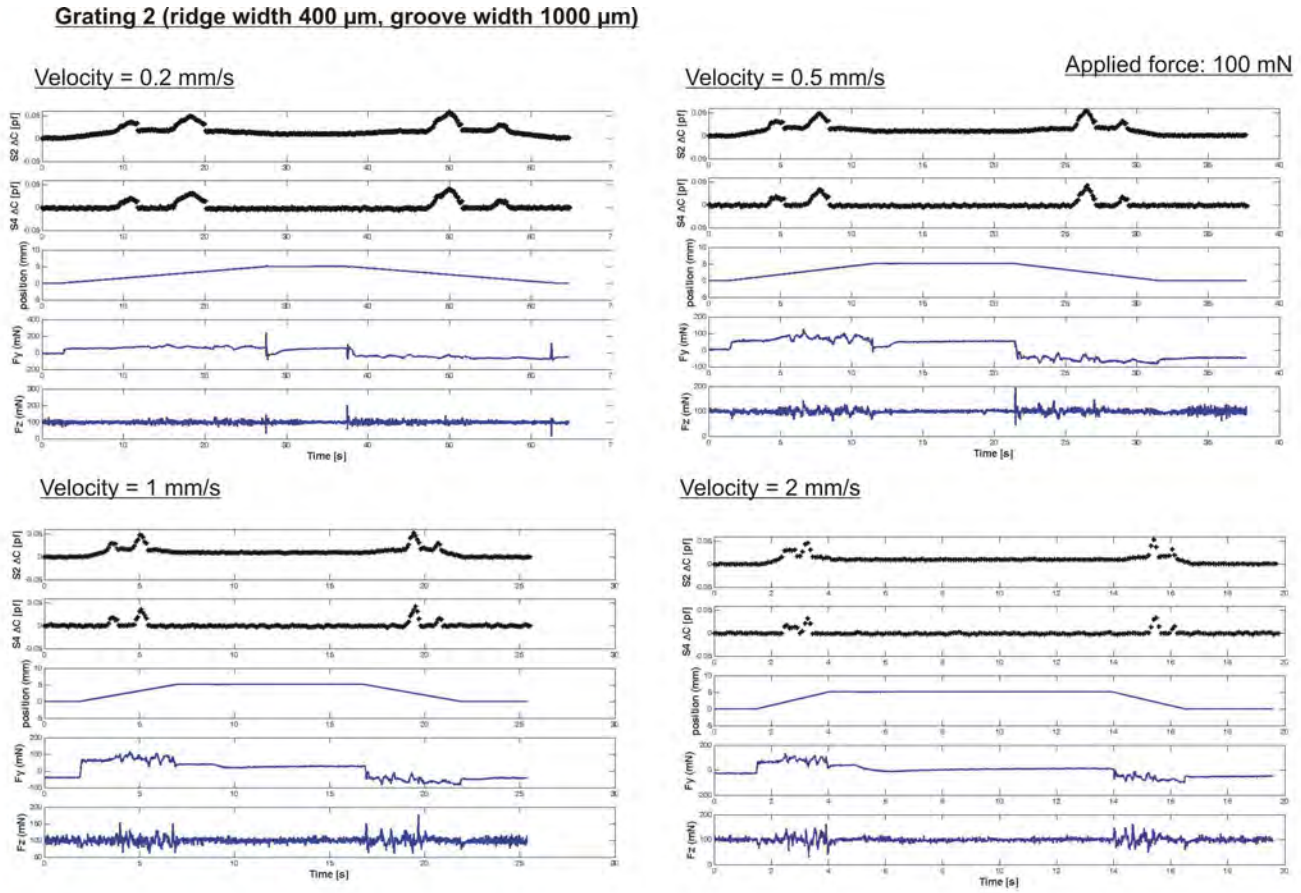

FIGURE 6.19: Typical response of two sensors S2 and S4 to Grating 2 (coarse grating) at an applied contact force of 100 mN. Traces show the sensor outputs, position data and forces (F_y and F_z) applied through the grating

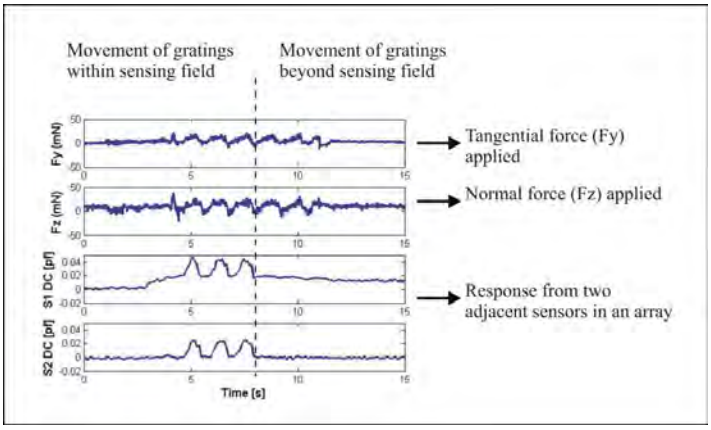

FIGURE 6.20: Response of a single sensor (Δ C) to an applied normal force of 10 mN via Grating 1. Signal output peaks correspond to the ridges of the grating within the sensing region of the device

Based on the implemented speeds and known spatial periodicity (λ) of the gratings, the expected peak frequency for each experimental run was predicted using

$$f_{peak} = \frac{v}{\lambda} \tag{6.1}$$

Further, for each experimental run, a Fast Fourier Transform (FFT) of the sensor signal output was calculated and the peak frequency was determined. Results for estimated and experimentally obtained values of peak frequency for each experimental run conducted at an applied contact force of 10 mN are shown in Fig. 6.21. Experimentally determined values of peak frequency were in correlation with the calculated values.

The above results demonstrated the capability of the sensor in discriminating between the fine and coarse grating. In order to conduct a more detailed analysis, further gratings were fabricated, specifications of which are given in (Table 6.3). Once again a 'passive-touch' protocol was implemented where the gratings were tangentially displaced over the sensor surface at velocities ranging from 0.05 mm/s to 4 mm/s, and with an applied average normal

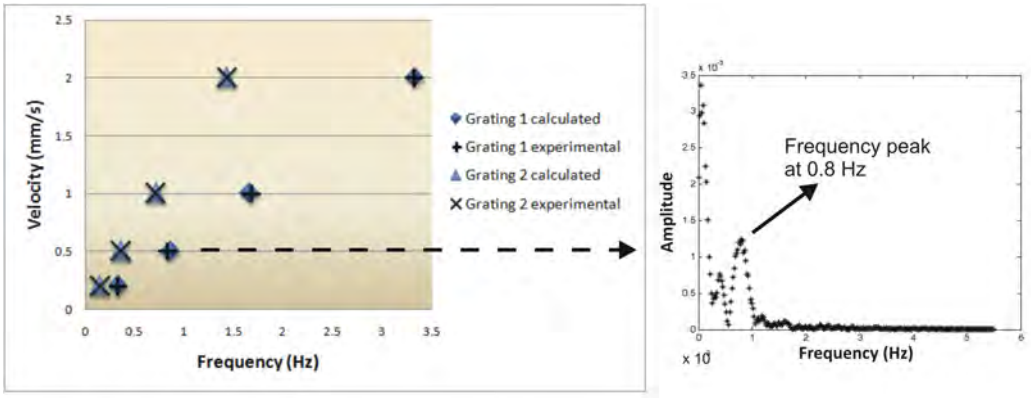

FIGURE 6.21: [left] Expected and experimentally determined values of peak frequency obtained following relative motion between the sensor array and Gratings 1 and 2 at the four implemented scan velocities, [right] An example of the calculated FFT spectrum for single sensor output showing the experimentally determined peak frequency ($fpeak$)

force Fz of 10 mN.

TABLE 6.3: Specification of gratings used for dynamic/lateral movement experiments

Grating	Ridge height (μm)	Ridge width (μm)	Groove width (μm)	Spatial periodicity λ (μm)
A	400	200	200	400
B	400	200	400	600
C	400	200	600	800
D	400	200	800	1000
E	400	200	1000	1200

The output of sensors in response to each of the applied gratings at different velocities was assessed. Fig. 6.22 shows the responses of a single sensor for each of the five applied gratings varying in spatial periodicity, when a scanning velocity of 0.1 mm/s was used.

As before, the FFT spectra of the signals from the sensors were calculated for each experimental run (i.e each grating at each velocity) and from this, the peak frequency was determined. The spatial periodicity λ was then calculated from the scanning velocity v and peak frequency f_{peak}, according to the following equation:

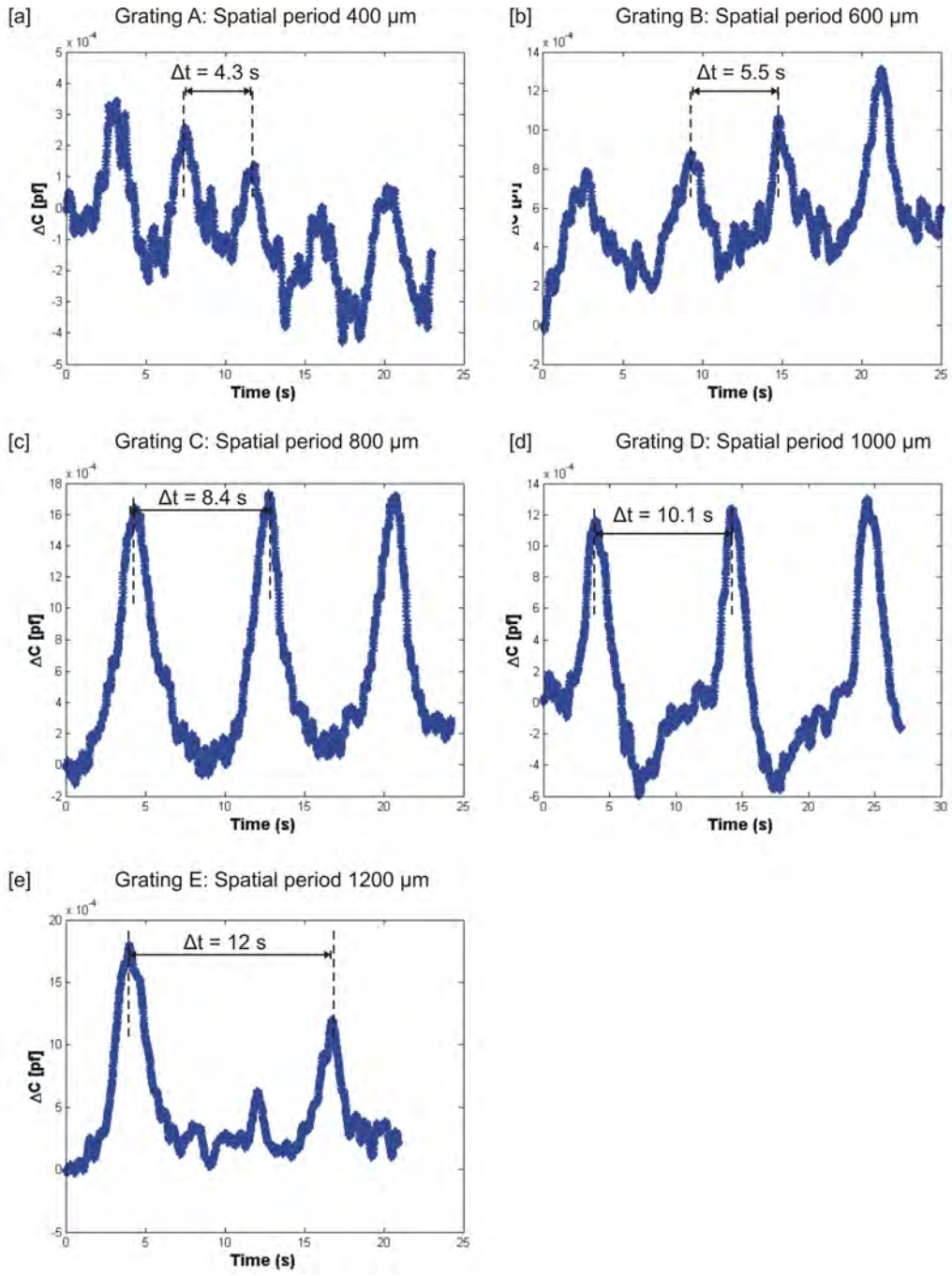

FIGURE 6.22: Single sensor time domain outputs in response to five applied gratings varying in spatial periodicity (using a velocity of 0.1 mm/s)

$$\lambda = \frac{v}{f_{peak}} \tag{6.2}$$

This allowed the capability of the sensors in detection of each grating to be established. Fig. 6.23 shows the determined periodicity of the gratings used for the measurements, each of which made at three different velocities. It can be seen that the sensor array was able to distinguish between all five gratings and good correlation was found between calculated and experimentally obtained values.

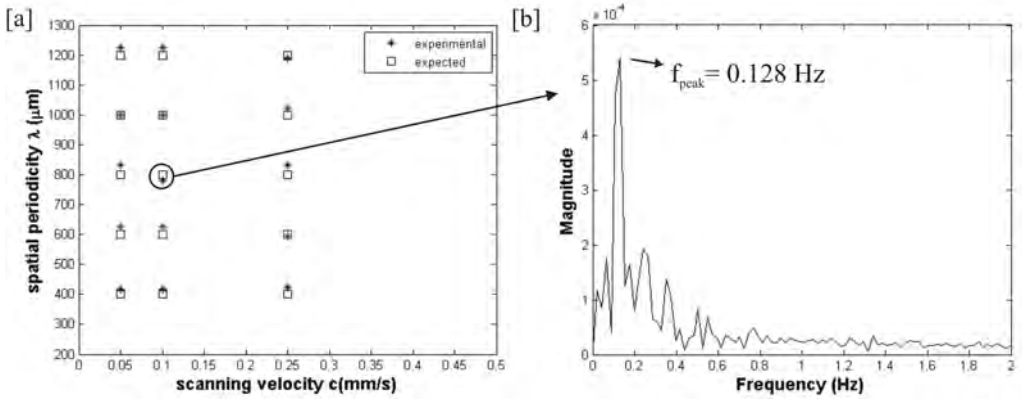

FIGURE 6.23: [a] Expected and experimentally determined grating spatial periodicity at three different scan velocities, [b] FFT spectrum for single measurement showing peak frequency ($fpeak$)

6.4.2 Discrimination of fabrics

After demonstrating the capability of the sensor array to discriminate between gratings of varying periodicity, the ability of the device to differentiate between fabrics was evaluated. Fabrics represent more realistic and complex surface texture in comparison to gratings. Three different fabrics were tested:

1. Polycotton (denim), having a thickness of 550 μm

2. Nylon, having a thickness of 360 μm

3. Cotton, having a thickness of 240 μm

The characteristic weave features of each material were visible under observation with a SEM (Fig. 6.24). Each fabric differed in terms of their weave size and patterns.

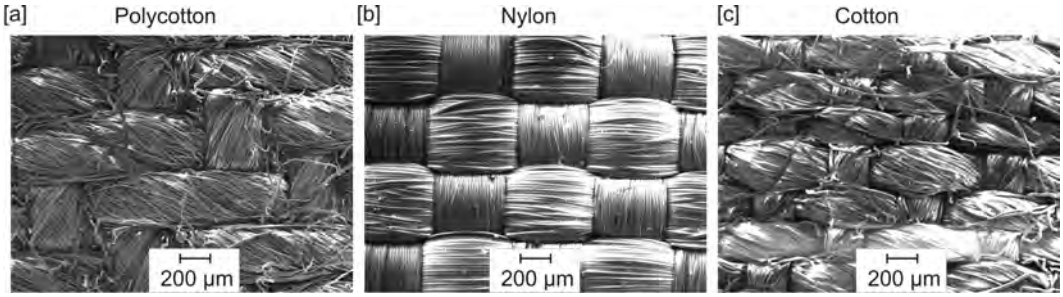

FIGURE 6.24: SEM images of fabrics tested [a] Polycotton, [b] Nylon, [c] Cotton

Experimental set-up

To enable movement of each of the fabrics relative to the sensor surface, a tribometer (Longshore Systems Engineering) was employed (Fig. 6.25).

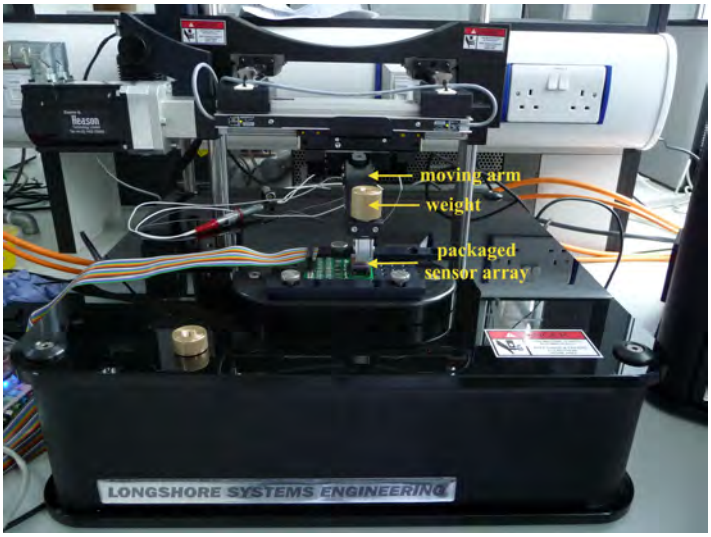

FIGURE 6.25: Tribometer used for investigating the ability of sensors to discriminate between different fabrics

The fabric sample was attached to the outer surface of a custom built cylindrical PDMS

probe, which was then mounted onto the moving arm of a tribometer as shown in Fig. 6.26. The sensor chip was mechanically secured to the base of the tribometer. The arm of the tribometer was adjusted to allow contact between the probe and the sensor. A weight of 40 g was applied to the loading arm of the tribometer which was then programmed to instigate three successive experimental runs of a double ramp lateral displacement relative to the sensor surface. Thus, three subsequent experimental runs were implemented, with each run comprising scanning the probe across the sensors in one direction, followed by a subsequent scan in the opposite direction. A probe movement velocity of 1 mm/s was used. In addition to the three fabrics tested, the above tests were also conducted using the PDMS probe directly (with no fabric attached).

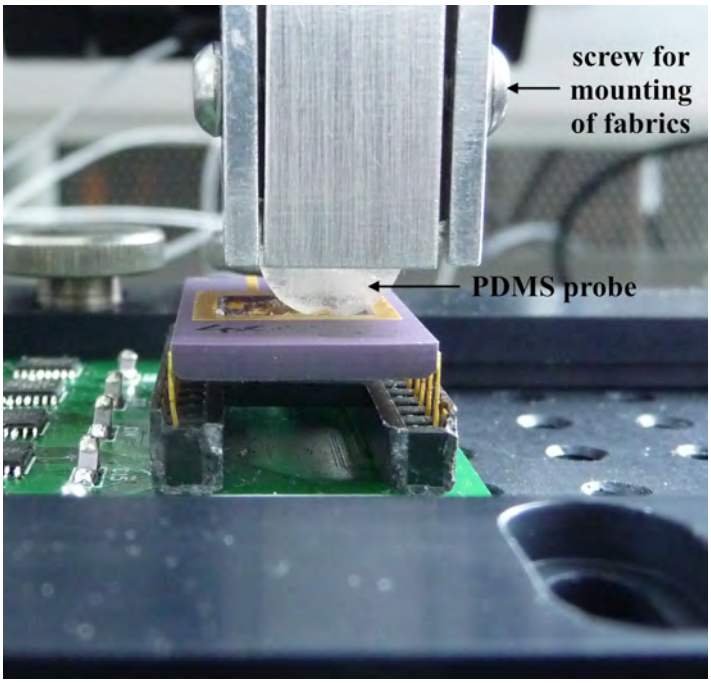

FIGURE 6.26: PDMS probe attached to moving arm of tribometer

Results

The signal outputs of the sensor array in response to stimuli applied through the PDMS probe and fabrics polycotton and nylon are shown in Fig. 6.27. The time domain sensor outputs reveal characteristic responses for each material. In particular, specific features were observed in peak density and in the spatial period. Fig. 6.28 shows a comparison between the outputs of a single sensor within an array to the scanning of the PDMS probe and the three fabrics which depict the output variations. The features in the sensor outputs are seen to be related to the spatial periodicity of the tested fabrics.

From Fig. 6.28, another noticeable feature in the sensor outputs is the directional response to applied tangential loading, apparent through an enhanced sensitivity in one scan direction. This can be attributed to factors such as non-uniform thickness of the packaging layer and an uneven surface topology, which can lead to differences in stress propagation through the material dependent on the scan direction.

6.4.3 Influence of 'fingerprint' like packaging

To conduct a preliminary assessment of the influence of incorporating fingerprint like ridges in the packaging of the tactile sensors, the experiments described in Section 6.4.2 were repeated on the fabricated sensor array packaged with patterned PDMS (as described in Chapter 5). A smooth PDMS probe and three fabrics (polycotton, nylon and cotton) were dragged over the surface of the sensor while simultaneously recording its output.

Results for the output of a single sensor to each of the textures are shown in Fig. 6.29.

As observed for the case of the unpatterned PDMS sensor packaging, the sensors packaged with textured PDMS showed differences in sensor outputs for each of the fabrics tested.

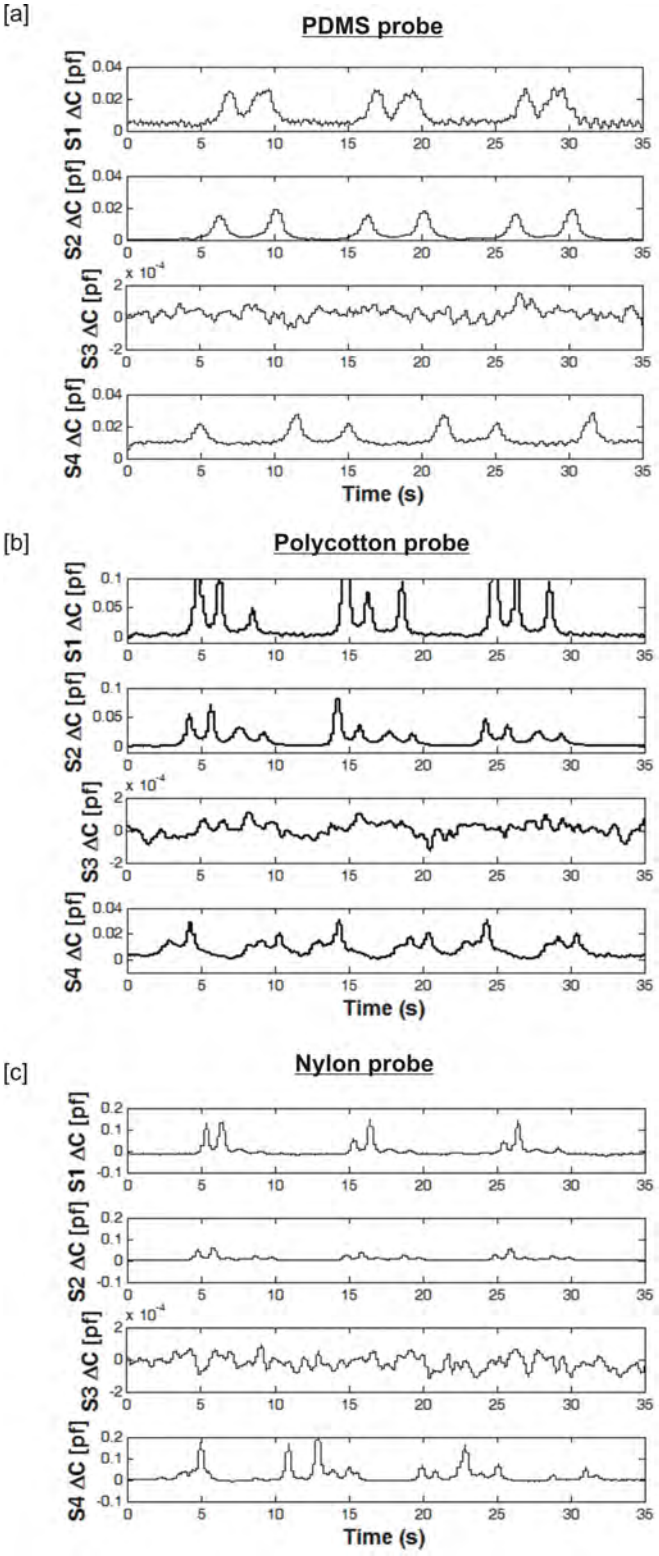

FIGURE 6.27: Results showing sensor array output *(ΔC)* with time in response to applied textures including smooth PDMS mould and fabrics: polycotton [a], nylon [b] and cotton [c]. No change in signal was obtained from sensor S3 due to mechanical damage

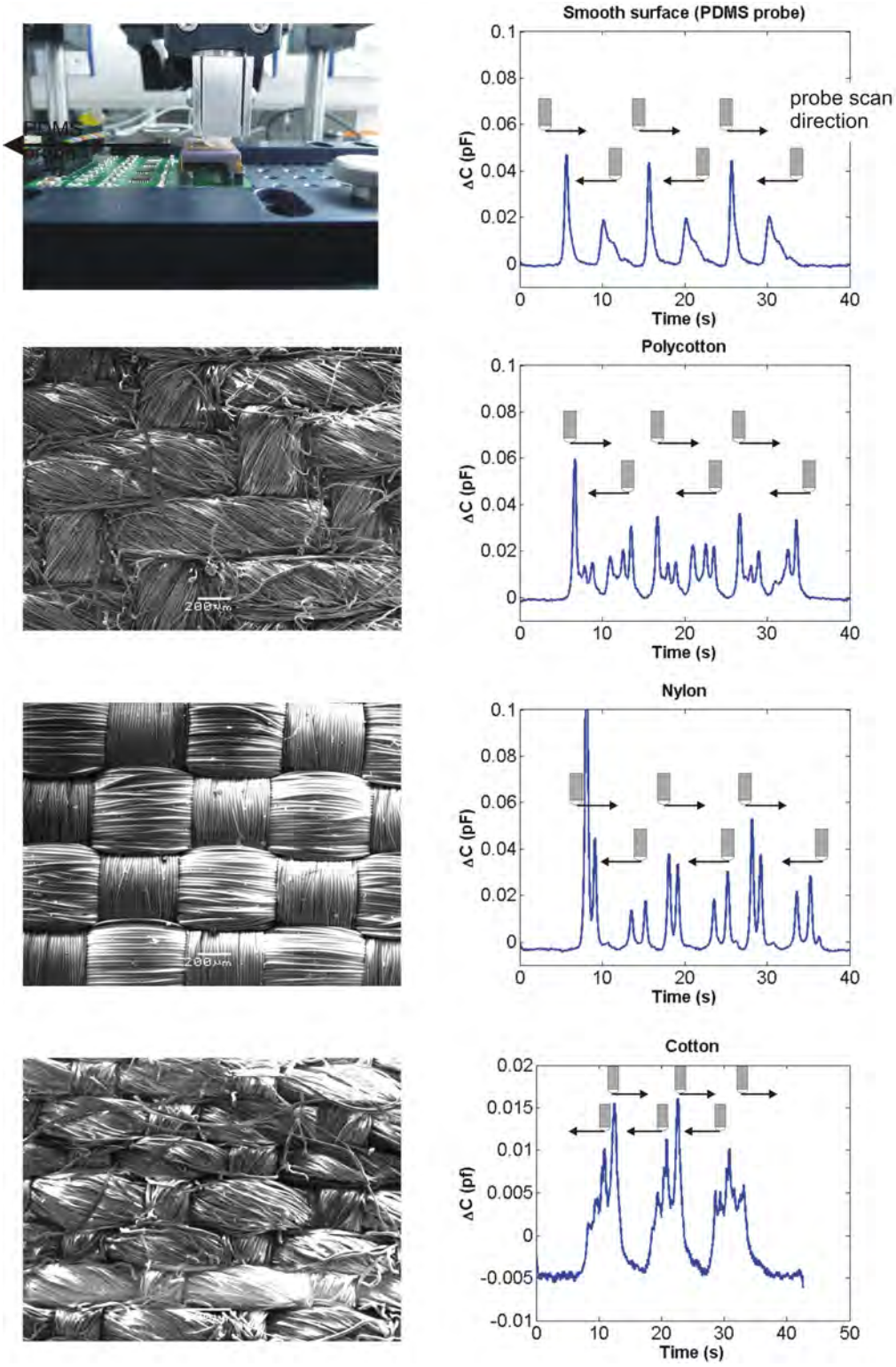

FIGURE 6.28: Results showing time domain output of a single sensor S2 *(ΔC)* in response to applied textures including smooth PDMS mould and fabrics: polycotton, nylon and cotton

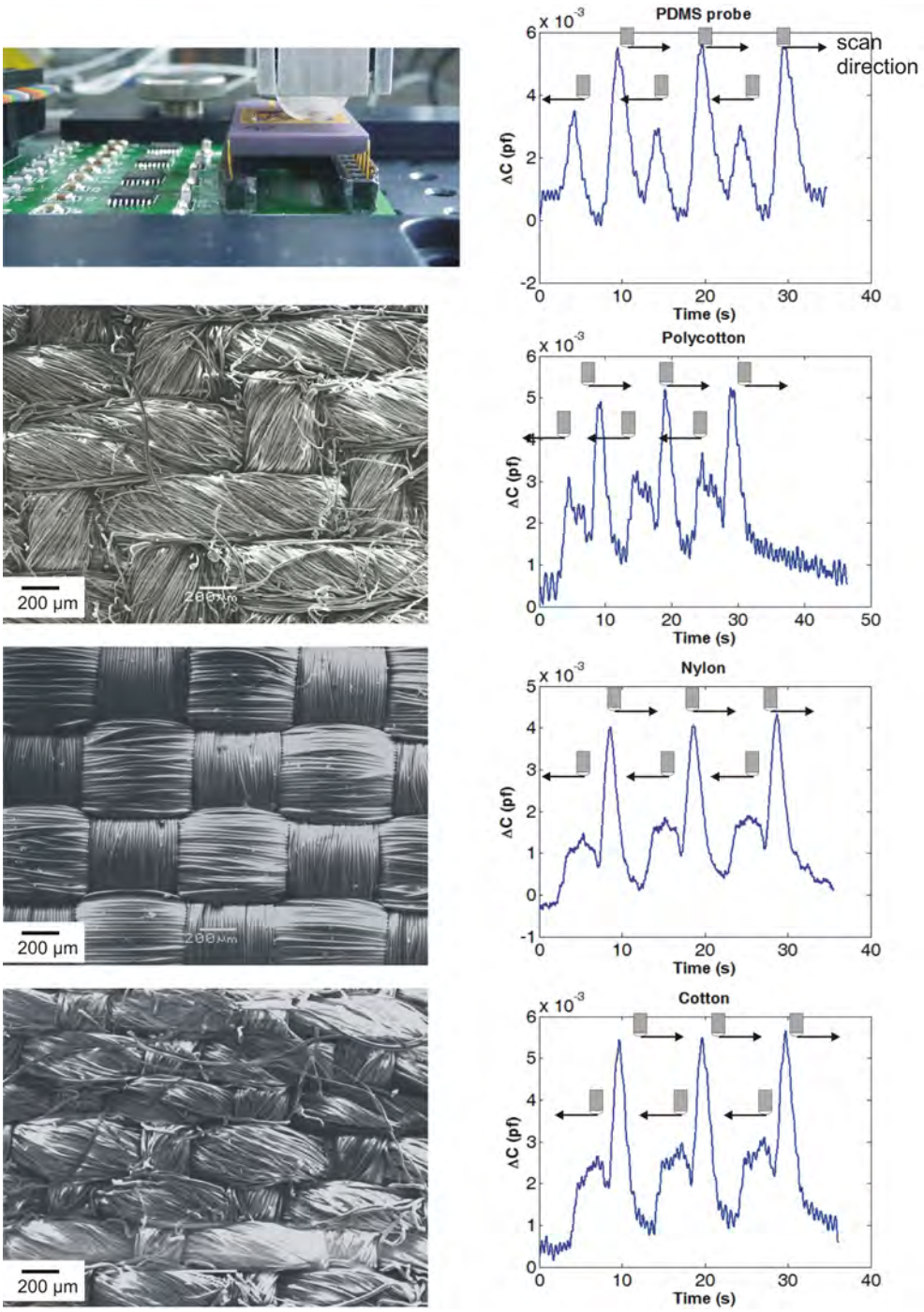

FIGURE 6.29: Results showing the time domain response of a sensor incorporating 'fingerprint' like topography on its packaging layer. The sensor outputs *(ΔC)* are for the case of the following textures dragged over the sensor surface: PDMS mould, polycotton, nylon and cotton

Further, for the sensors coated with the textured PDMS, the signal output showed a unique noticeable higher frequency component for each fabric tested. This can be attributed to the interaction between the ridges of the packaging and the characteristic periodic features of the fabric. Thus, these preliminary results show that the incorporation of fingerprint like ridges enhance the capability of the sensors for detecting fabrics with a higher precision in comparison to the unpatterned packaged sensors. Further data analysis is required to closely examine and identify periodic features so that a specific signature can be associated for various fabrics. To enable this, the use of neural network approaches can be employed, which is beyond the scope of this research.

6.4.4 Effect of fabric thickness

To investigate the effect of thickness of the fabric samples on the sensor response, the experimental set-up described in Section 6.3.2 was used. For each test, the fabric sample was placed over the sensor surface and a rigid cylindrical probe (2 mm in ϕ) was indented into the sensor with an applied force of 100 mN. The probe was then laterally displaced over the sensor surface. Two experimental runs were conducted, one at a probe scan velocity of 0.1 mm/s and the other at a scan velocity of 0.65 mm/s.

The signal outputs from a single sensor channel to the three applied fabrics are shown in Fig. 6.30. It can be seen that there is a definite variation in the profile of the sensor signal output for each of the fabrics. An decrease in the sharpness of the sensor response profile occurs with increasing fabric thickness. This corresponds to an increase in the area of response of the sensor which can be attributed to a increase in the area of stress distribution that is transferred to the sensor.

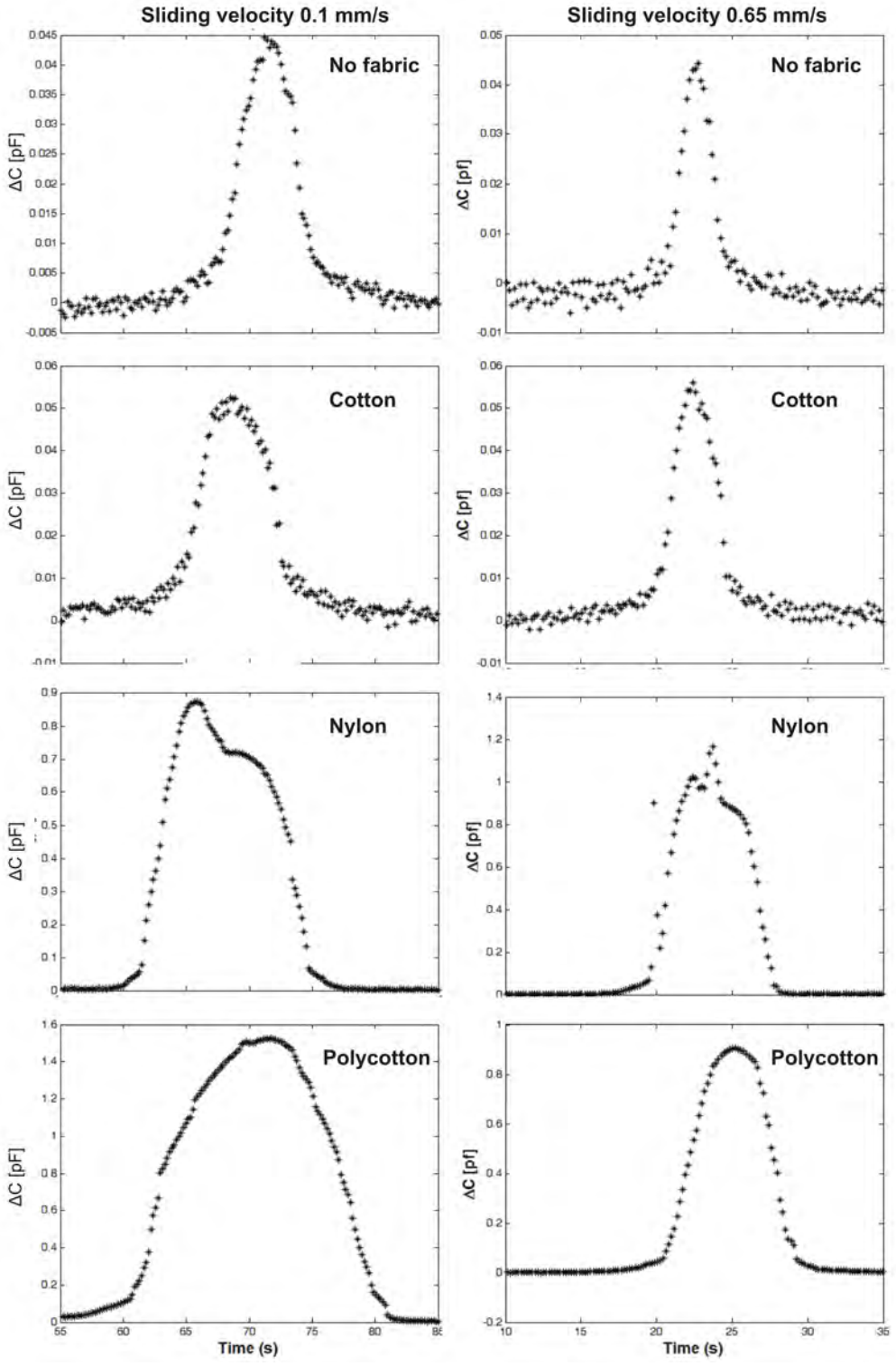

FIGURE 6.30: Results showing sensor output *(ΔC)* with time to tangentially applied stimulus via a smooth PDMS mould and fabrics varying in thickness: polycotton (550 μm), nylon (360 μm) and cotton (240 μm)

6.5 Discussion of results

6.5.1 Characterisation of single sensor response

The characteristic force - capacitance response of the sensors was evaluated by applying controlled displacements to the sensor diaphragm through a spherical probe and simultaneously recording the resulting change in capacitance. The method of applying indentations of controlled amplitudes via punctate probes has been previously used while analysing the performances of single tactile afferents in the human fingerpad [51].

As expected, the sensors fabricated in this work responded to an increase in probe indentation depth with an increase in capacitance change. This corresponds to the pattern of response of Slowly Adapting (SA I) mechanoreceptors (i.e. the Merkel cells) that respond to an increase in indentation depth of probes with an increase in nerve impulse firing rate [182].

Table 6.4 summarises the main characteristics of the evaluated sensors.

TABLE 6.4: Specification of gratings used for static indentation experiments

Sensor	Average sensitivity	Tested range of sensor
Bare sensor	53.3 fF/mN	25 mN
PDMS packaged	0.068 fF/mN	1.6 N
Dragon skin packaged	0.01 fF/mN	2 N
Tissue engineered skin packaged	0.09 fF/mN	0.7 N

The bare sensor demonstrated high force sensitivity (average of 0.035 pF/mN) and a dynamic range of 25 mN. The discrepancies in the experimentally determined characteristics of the bare sensors from those predicted using numerical methods (Chapter 3) can be attributed to deviations in actual dimensions of the sensors from designed dimensions. This was most likely due to tolerances of the substrate wafer used to fabricate the devices (Chapter 4).

Packaged sensors showed reduced force sensitivity but a greater dynamic range in comparison to their unpackaged counterparts. The packaging layer acts as a low-pass filter and the amount of cross talk between sensors depends on the thickness of this layer. Sensors that were packaged with PDMS demonstrated improved characteristics over sensors packaged with Dragon Skin®. As a thinner packaging thickness was achievable with PDMS, sensors packaged with this material demonstrated greater sensitivity compared with sensors packaged with Dragon Skin®. The latter also demonstrated significant creep, where a increase in capacitance change occurred even during the steady phase of indentation. This behaviour is contradictory to the manner of response by biological tactile sensors which tend to adapt to a constant stimulus by decreasing their firing rates [170].

PDMS packaged sensors followed patterns of applied indentation with no observed creep and time delay in their responses. They displayed an average sensitivity of 0.068 fF/mN and a dynamic range of approximately 1.7 N. Previous studies on human perception of touch have shown that the finger contact forces used for discriminating roughness ranged from 0.8 - 1.6 N with an average of 1 N [50]. Thus, the packaged sensors are able to cope with forces within this range.

Bare and packaged sensors were tested to indentation impulses of less than 0.2 s and 0.4 s respectively. For the packaged devices, testing at shorter time impulses was limited by the probe speed attainable using the current instrumentation. As the devices are silicon based, they inherently possess a high bandwidth as confirmed by the FEM simulation. The bandwidth of the tactile system as a whole is defined by two main factors: The acquisition frequency of the capacitance detection electronics system, which with the currently implemented system is 11.25 Hz per channel of the 4 sensors array, and the response of the PDMS

layer.

A key design feature in the presented sensing array is the inclusion of reference capacitors that were implemented in close proximity to each sensing element. This eliminated the effects of stray capacitance; a commonly reported problem in capacitive sensors.

6.5.2 Texture detection

The ability of the sensors to successfully discriminate between textures presented in the form of gratings varying in spatial periodicity and fabrics of different weave patterns was demonstrated [178]. Humans tend to detect the roughness of a surface by dragging their finger across it. Mimicking this, a dynamic protocol was employed when using the sensors to discriminate between textures.

Studies that have been conducted to investigate the neural code behind roughness perception showed that when stimulating the finger with varying textures, the spatial variation in SA I impulse rate could be closely correlated with perceived roughness over the whole applied stimulus range. In biological tactile sensing, the multiple parameters of objects being manipulated by the human hand, such as shape, orientation, position on skin cannot be represented by a single tactile afferent but requires responses by a population of fibres. In analogy, the sensing device developed in this work implemented an array of tactile sensors. An assessment of the variation in responses of sensors within an array to an applied surface can provide information on the spatial features of a surface. A static protocol may be sufficient when assessing coarse textures. However, such an approach could lack in accuracy when exploring surfaces with spatial features finer than the spacing between neighbouring sensors. With this in consideration a dynamic touch protocol was adopted for discriminating

finer textures. This involved introducing relative motion between the tactile array and the surface, and analysing the vibrational patterns arising in sensor outputs. In principle such an approach may be effective with a single sensor, but the availability of an array offers several advantages such as a wider sensorised contact area and the possibility of identifying irregular texture patterns differing along the specimen. The adoption of a dynamic touch protocol in assessment of fine textures is in consensus with human perception of fine textures where movement is suggested to be essential [60, 172].

The availability of an array of tactile sensors allows a combined spatio-temporal approach for the discrimination of textures, by considering the spectral content of each single sensor output and the variation in responses of spatially located sensors.

6.5.3 Analogy with biological mechanoreceptors

Signals from the mechanoreceptors provide information regarding the location and timing of contact between an object and skin. Additionally, they convey information regarding surface form and texture which can assist in object manipulation and recognition.

The sensors developed in this work can be compared to biological mechanoreceptors of the human fingerpad. In the nature of their response, they particularly imitate the slowly adapting (SA I) mechanoreceptive units i.e. the Merkel cells. These receptors generate responses to mechanical stimuli for as long as a stimulus is present and are hypothesised to be responsible for conveying information regarding surface form and texture [37].

SA I afferent units have small, well defined receptive fields and are responsible for the high spatial acuity and resolution of the human fingertip which is approximately 1 mm [24]. In the presented sensing device, spatial resolution is determined by the distance between

sensing elements in an array; the sensors were spaced 150 μm apart (centre-to-centre distance of 570 μm), allowing high resolution. In human fingertips, the density of SA I units is 70 per cm^2 [49]. As demonstrated in this work, the use of microtechnology in the design of the sensor array allowed a density of 95 channels per cm^2 to be achieved.

The receptive field of each sensor was experimentally assessed analogous to receptive fields of biological mechanoreceptors. Similarities were demonstrated between the receptive field characteristics of mechanoreceptors and sensors. The receptive fields of mechanoreceptors exhibit points of maximum sensitivity known as hot spots [42]. Fig. 6.31 shows the responses of 13 SA I units in the monkey fingerpad to an applied stimulus as a function of distance from the receptive field centre [24]. The response, depicted by the number of action potentials emitted (in impulses/sec) in the first second of indentation is seen to decrease with increasing distance from the receptive field centre. Variation in sensitivities of the different SA I units to the same applied stimulus is also observed.

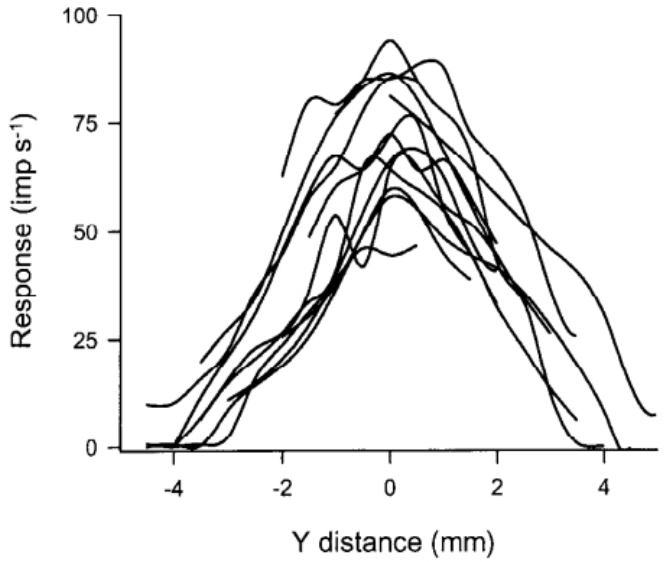

FIGURE 6.31: Response of 13 SA I afferents to an applied stimulus as a function of distance from the receptive field centre [24]

As in the case of mechanoreceptors, the developed sensors demonstrate a point of maximum sensitivity, when the stimulus is applied to the centre of the sensor's receptive field (see Fig. 6.13) [177]. The response was shown to progressively decrease as the probe is indented at locations away from this region. Similar to the patterns of response found in SA I mechanoreceptive afferents [42], the receptive field size tends to increase with an increase in indentation amplitude or stimulus intensity. Studies conducted on receptive fields of mechanoreceptive afferents have shown that nearly half of the mechanoreceptor afferents exhibit elliptical receptive fields [182]. The sensing membranes of the designed sensors were rectangular; due to this asymmetrical design it is expected that the response field would be elliptical rather than circular. Additionally, by varying diaphragm dimensions it was possible to realise sensors with varying sensitivities as was shown in Figs. 6.3 and 6.7.

SA I afferent units possess directional sensitivity with the discharge of afferents increasing with stimuli applied in particular directions, but decreasing in others [45]. Similarly, the sensing device developed in this work demonstrated directional sensitivity as shown in Fig. 6.28.

6.6 Conclusions

In this chapter, the characterisation of the MEMS based tactile sensors was described. In the following, a summary of the main tests conducted and their results are given.

- Bare/unpackaged sensors were characterised by using indentation testing, which is also commonly used in the characterisation of individual biological tactile afferents. As predicted from analytical models, the sensors showed a non-linear dependence on

applied load. The sensors demonstrated a high force sensitivity and were able to resolve forces in the sub mN range, a scale that the commercial load cell was unable to resolve.

- Sensors packaged with two different silicone elastomers, PDMS and Dragon Skin were characterised using indentation tests (as conducted on bare sensors). In comparison, sensors packaged with PDMS showed better performance characteristics.

- Lateral sliding tests were conducted using a rigid spherical probe to scan across all sensors in the array. Based on the response of each sensor, the spatial location of stimulus with respect to the sensors was established.

- To examine the receptive field of the sensors, indentations were applied at spatially varying locations and responses of neighboring sensors were recorded. Thus the receptive field of each sensor for a particular stimulus could be established.

- The ability of the sensors to discriminate between various textures was evaluated and demonstrated using gratings and fabrics as applied stimulus to the sensors.

- The potential benefits of introducing a 'fingerprint' like topography on the artificial skin coating of the sensor was demonstrated through the presence of superimposed high frequency components in the signal output of the sensor that could be associated with micro-patterns specific to each texture (fabric) tested.

7

Conclusions and Future Work

Contents

7.1 Summary and Conclusions

The aim of the work carried out in this thesis was to develop a bioinspired tactile sensing system suitable for incorporation into the fingerpad of an artificial finger.

To achieve this goal, a scientific understanding of mechanoreceptors and the process of neural coding of mechanical events at the biological skin surface was initially established. The behavior of mechanoreceptors is a cornerstone in the understanding of such a complex system as the sensation of touch, and the derived design of a technical imitation. The slowly adapting type I afferent tactile units (SA I/ merkel cell complexes) were identified in the literature as being mainly responsible for the recognition of surface form and texture. Hence,

their performance was used as a benchmark in the development of the artificial tactile sensors.

The use of MEMS technology in implementing a bio-inspired tactile sensing device was explored in this thesis. Such an approach has numerous advantages, such as the possibility for batch fabrication, high performance, small size, low cost and the potential for integration of sensors and associated electronics on a single chip. Through a survey of the literature, it was identified that currently there are no known devices that demonstrate functional capability on par with that of the fingertip tactile sensors.

Based on the biological model, a number of requirements for the sensing device arise, which have been addressed in this thesis. These requirements include the recognition of surface form and texture and the possession of a combination of mechanoreceptor-like attributes, such as high spatial and force resolution, high density, directional sensitivity and range. Rather than focussing on developing a device with linear output characteristics, the work in this thesis was geared towards developing a tactile device with the performance capability analogous to the fingertip sensors that also do not demonstrate linear output characteristics and have varied ranges and sensitivities. Additionally, the goal was to utilise a minimum number of process steps in the fabrication of the sensors in order to enhance the overall yield.

The resulting tactile sensor prototypes that have been developed in this work consisted of a linear array of 4 sensors. The sensors were designed to work on the principles of capacitive sensing because of its performance capabilities in terms of increased sensitivity, robustness, low power consumption and high stability. The principle sensing structure is a monocrystalline silicon based rectangular diaphragm, which deflects on the application of a mechanical

pressure causing a change in capacitance that can be measured. Two different designs were investigated: a fixed-fixed plate (Design 1) and a clamped rectangular plate (Design 2). The devices were fabricated using a silicon-on-oxide substrate using simple process steps compatible with low cost, high volume production. In comparison with other reported MEMS tactile sensors to date, the fabrication methods adopted in this work utilised fewer process steps.

During the fabrication process, it was found that sensors with the clamped rectangular sensing diaphragm (Design 2) showed higher yield. The fixed-fixed sensing diaphragms were more susceptible to snap-down or stiction during the wet etch stage of the fabrication process. Based on the higher fabrication yield of Design 2 type devices, these were further packaged and characterised.

To provide a skin-like, protective layer for the bare sensor surface, the use of various materials has been investigated such as silicone elastomers, namely poly dimethyl siloxane (PDMS) and Dragon Skin. In comparison to Dragon Skin, PDMS demonstrated more favourable characteristics because of its following features:

- Lower viscosity allowing formation of thin packaging layers
- Ease of surface patterning using moulds fabricated by dry etching of silicon
- Higher dynamic range allowed because of their higher temporal response characteristics

A method for successfully introducing a fingerprint like topography in the form of parallel ridges into the tactile sensor packaging material (PDMS) was demonstrated. Results of preliminary tests showed this to be a promising approach for improved texture recognition,

through superposition of additional frequency components in the signal output of the sensor, corresponding to the the characteristic periodic patterns of fabrics.

As one of the project goals was to develop a human-like or anthropomorphic system, the performance of the sensors embedded within tissue engineered skin was also investigated. Although the long-term sustainability of such a system was beyond the scope of the work in this project, preliminary tests showed feasibility of implementing an artificial sensing system within tissue engineered skin.

Finally, the sensors developed in this work were characterised using tests mimicking those conducted in the characterisation of responses of SAI mechanoreceptors in the fingertip. This involved investigating their response patterns to applied mechanical stimulus through indentations applied with a rigid probe. Additionally, stimuli in the form of gratings of alternating ridges and grooves, that are commonly used to stimulate the fingerpad in neurophysiological experiments, were also used to assess the capability of the sensors for texture recognition. A dynamic scanning protocol similar to the finger scanning process used by humans in the detection of textures, was shown to be beneficial when using the sensing devices to examine surfaces, particularly when discriminating fine textures.

The sensitivity of the designed sensors was found to be sufficient so as to allow the decoding of textures at stimulus magnitudes (force and indentation) similar to that applied by the human fingertip during surface exploration. The bare sensor was able to resolve forces in the sub mN range and the packaged sensors were able to detect forces as small as 10 mN (Fig 6.20), which is the force resolution capability of the human fingertips [31]. Previous research has shown that the biological mechanoreceptive afferents exhibit non-linearities in their responses to indentations and variations in their sensitivities and ranges [22]. In

this work it was demonstrated that by varying the dimensions of sensing diaphragms, it is possible to realise a sensing device on a single chip with sensors varying in sensitivity. Thus a wider and controllable dynamic range is achievable.

To conclude, the key outcomes of this thesis are summarised below:

- A MEMS based tactile sensing array was developed with individual sensors shown to imitate the SA I mechanoreceptors of the human fingerpad, that fire impulses for as long as a mechanical stimulus is present.

- The receptive field characteristics of sensors were evaluated and similarities in their features with that of the biological mechanoreceptors was demonstrated.

- The ability of the sensors to discriminate between various textures (periodic gratings and fabrics) was demonstrated.

- The successful embedding of the MEMS based sensors within skin like packaging material was demonstrated. Further, emulating the human finger, fingerprint like surface ridges were introduced into the packaging material. A successful method for incorporating such topography into the skin packaging material PDMS was described.

- A combined spatio-temporal approach as adopted by humans during surface exploration tasks was shown to be suitable for evaluating characteristics of a texture.

7.2 Future work

Although a linear array of 4 sensors has been developed in this work to demonstrate a proof of concept, using the same processes outlined in this thesis, a two dimensional array can easily

be implemented. This would allow the acquisition of a greater amount of tactile data at a single contact instance between the sensing device and the surface. Further, as demonstrated, by varying the geometrical dimensions of sensing diaphragms, sensors varying in sensitivity can be implemented. Thus, by incorporating sensors of different diaphragm dimensions on a single chip, a sensing device with a wider dynamic range can be achieved. The fabrication process adopted in this work allows the realisation of such a device by simply incorporating various designs on the lithography mask used for patterning the substrate wafers.

The temporal sensitivity of the sensing device in this work was limited by the sampling frequency of the developed signal acquisition electronics. This can be improved by incorporating faster capacitance to digital converter chips in the signal acquisition electronics system.

The use of artificial neural networks in processing data from the tactile sensors can be explored in further works. As they have the ability to learn, a large volume of data such as that obtained from the output of the tactile sensor array can be processed to allow pattern recognition. The use of artificial neural networks for such a function represents a further step towards emulating the biological sense of touch.

The mechanical analysis of the multilayer structure including the sensor and skin-like packaging layer is a complex on-going research issue. Optimisation of the packaging layer through incorporation of features such as fingerprint like topography can be explored further.

The electric output signal of the sensors presented in this thesis can further be processed, in order to activate particular mechanoreceptor afferent units through the use of appropriate neural interfaces. This will enable a form of sensory feedback to be provided to a prosthetic user and ultimately, the perception of touch.

References

[1] M. H. Lee and H. R. Nicholls. *Review article tactile sensing for mechatronics–a state of the art survey*. Mechatronics **9**(1), 1 (1999).

[2] J. Dargahi and S. Najarian. *Human tactile perception as a standard for artificial tactile sensing - a review*. International Journal of Medical Robotics and Computer Assisted Surgery **1**(1), 23 (2004).

[3] M. E. H. Eltaib and J. R. Hewit. *Tactile sensing technology for minimal access surgery–a review*. Mechatronics **13**(10), 1163 (2003).

[4] P. Puangmali, K. Althoefer, L. D. Seneviratne, D. Murphy, and P. Dasgupta. *State-of-the-art in force and tactile sensing for minimally invasive surgery*. IEEE Sensors Journal **8**(3-4), 371 (2008).

[5] O. Tohyama, M. Kohashi, M. Fukui, and H. Itoh. *A fiber-optic pressure microsensor for biomedical applications*. In *Solid State Sensors and Actuators, 1997. TRANSDUCERS '97 Chicago., 1997 International Conference on*, vol. 2, pp. 1489–1492 vol.2 (1997).

[6] C. Hierold, B. Clasbrummel, D. Behrend, T. Scheiter, M. Steger, K. Oppermann, H. Kapels, E. Landgraf, D. Wenzel, and D. Etzrodt. *Low power integrated pressure sensor system for medical applications*. Sensors and Actuators A: Physical **73**(1-2), 58 (1999).

[7] E. Cibula and D. Donlagic. *Miniature fiber-optic pressure sensor with a polymer diaphragm*. Appl. Opt. **44**(14), 2736 (2005).

[8] A. Eklund, A. Bergh, and O. Lindahl. *A catheter tactile sensor for measuring hardness of soft tissue: measurement in a silicone model and in an in vitro human prostate model*. Medical and Biological Engineering and Computing **37**(5), 618 (1999).

[9] G. S. Dhillon and K. W. Horch. *Direct neural sensory feedback and control of a prosthetic arm*. Neural Systems and Rehabilitation Engineering, IEEE Transactions on **13**(4), 468 (2005).

[10] L. Beccai, S. Roccella, A. Arena, F. Valvo, P. Valdastri, A. Menciassi, M. C. Carrozza, and P. Dario. *Design and fabrication of a hybrid silicon three-axial force sensor for biomechanical applications*. Sensors and Actuators A: Physical **120**(2), 370 (2005).

[11] B. B. Edin, L. Beccai, L. Ascari, S. Roccella, J. J. Cabibihan, M. C. Carrozza, and Ieee. *A bio-inspired approach for the design and characterization of a tactile sensory system for a cybernetic prosthetic hand*. In *2006 Ieee International Conference on Robotics and Automation*, Ieee International Conference on Robotics and Automation, pp. 1354–1358 (2006).

[12] L. D. Harmon. *Automated tactile sensing*. The International Journal of Robotics Research **1**(2), 3 (1982).

[13] S. Ramkumar, D. Wood, K. Fox, and S. Harlock. *Developing a polymeric human finger sensor to study the frictional properties of textiles*. Textile Research Journal **73**(7), 606 (2003).

[14] R. D. Howe. *Tactile sensing and control of robotic manipulation*. Advanced Robotics **8**(3), 245 (1994).

[15] J. Tegin and J. Wikander. *Tactile sensing in intelligent robotic manipulation - a review*. Industrial Robot-an International Journal **32**(1), 64 (2005).

[16] A. Dargahi and S. Najarian. *Advances in tactile sensors design/manufacturing and its impact on robotics applications - a review*. Industrial Robot-an International Journal **32**(3), 268 (2005).

[17] H. Kawasaki, T. Komatsu, and K. Uchiyama. *Dexterous anthropomorphic robot hand with distributed tactile sensor: Gifu hand ii*. Mechatronics, IEEE/ASME Transactions on **7**(3), 296 (2002).

[18] M. C. Carrozza, P. Dario, F. Vecchi, S. Roccella, M. Zecca, and F. Sebastiani. *The cyberhand: on the design of a cybernetic prosthetic hand intended to be interfaced to the peripheral nervous system*. In *Intelligent Robots and Systems, 2003. (IROS 2003). Proceedings. 2003 IEEE/RSJ International Conference on*, vol. 3, pp. 2642–2647 vol.3 (2003).

[19] G. Shannon. *A comparison of alternative means of providing sensory feedback on upper limb prostheses*. Medical and Biological Engineering and Computing **14**(3), 289 (1976).

[20] P. E. Patterson and J. A. Katz. *Design and evaluation of a sensory feedback-system that provides grasping pressure in a myoelectric hand*. Journal of Rehabilitation Research and Development **29**(1), 1 (1992).

[21] C. Pylatiuk, A. Kargov, and S. Schulz. *Design and evaluation of a low-cost force feedback system for myoelectric prosthetic hands*. JPO: Journal of Prosthetics and Orthotics **18**(2), 57 (2006).

[22] K. Sung Soo, A. P. Sripati, R. J. Vogelstein, R. S. Armiger, A. F. Russell, and S. J. Bensmaia. *Conveying tactile feedback in sensorized hand neuroprostheses using a biofidelic model of mechanotransduction*. Biomedical Circuits and Systems, IEEE Transactions on **3**(6), 398 (2009).

[23] E. K. Kim, G. J. Gerling, S. A. Wellnitz, and E. A. Lumpkin. *Using force sensors and neural models to encode tactile stimuli as spike-based responses*. In *Haptics Symposium, 2010 IEEE*, pp. 195–198 (2010).

[24] A. W. Goodwin and H. E. Wheat. *Sensory signals in neural populations underlying tactile perception and manipulation*. Annual Review of Neuroscience **27**(1), 53 (2004).

[25] R. S. Dahiya, G. Metta, M. Valle, and G. Sandini. *Tactile sensing: From humans to humanoids*. Robotics, IEEE Transactions on **26**(1), 1 (2010).

[26] R. S. Vivek Maheshwari. *Tactile devices to sense touch on a par with a human finger*. Angewandte Chemie International Edition **47**(41), 7808 (2008).

[27] G. J. Gerling and G. W. Thomas. *Fingerprint lines may not directly affect sa-i mechanoreceptor response*. Somatosensory and Motor Research **25**(1), 61 (2008).

[28] R. S. Johansson and A. B. Vallbo. *Tactile sensibility in the human hand: relative and absolute densities of four types of mechanoreceptive units in glabrous skin*. J Physiol **286**(1), 283 (1979).

[29] D. Purves, G. J. Augustine, D. Fitzpatrick, L. C. Katz, A. S. LaMantia, J. O. McNamara, and S. M. Williams. *Neuroscience* (Sinauer Associates, Sunderland (MA), 2004), 3 ed.

[30] K. O. Johnson, T. Yoshioka, and F. Vega-Bermudez. *Tactile functions of mechanoreceptive afferents innervating the hand*. Journal of Clinical Neurophysiology **17**(6), 539 (2000).

[31] S. J. Lederman and R. A. Browse. *The physiology and psychophysics of touch*. Proceedings of a NATO Advanced Research Workshop on Sensors and sensory systems for advanced robots pp. 71–91 (1988).

[32] K. O. Johnson. *The roles and functions of cutaneous mechanoreceptors*. Current Opinion in Neurobiology **11**(4), 455 (2001).

[33] Ã. B. Vallbo and K. E. Hagbarth. *Activity from skin mechanoreceptors recorded percutaneously in awake human subjects*. Experimental Neurology **21**(3), 270 (1968).

[34] M. F. Bear, B. W. Connors, and M. A. Paradiso. *Neuroscience: exploring the brain* (Lippincott Williams and Wilkins, 2007), 3 ed.

[35] K. Dandekar. *Role of mechanics in tactile sensing of shape*. Ph.D. thesis, Massachusetts Institute of Technology (1995).

[36] V. B. Mountcastle, R. H. LaMotte, and G. Carli. *Detection thresholds for stimuli in humans and monkeys: Comparison with threshold events in mechanoreceptive afferent nerve fibres innervating the monkey hand.* Journal of Neurophysiology **35**, 122 (1972).

[37] D. T. Blake, S. S. Hsiao, and K. O. Johnson. *Neural coding mechanisms in tactile pattern recognition: The relative contributions of slowly and rapidly adapting mechanoreceptors to perceived roughness*. J. Neurosci. **17**(19), 7480 (1997).

[38] S. Polakoviscova, H. Seidenberg, R. Mikusova, S. Polak, and V. Pospisilova. *Merkel cells - review on developmental, functional and clinical aspects*. Bratisl Lek Listy **112**(2), 80 (2011).

[39] Z. Halata, M. Grim, and K. I. Bauman. *Friedrich sigmund merkel and his merkel cell, morphology, development, and physiology: Review and new results*. The Anatomical Record Part A: Discoveries in Molecular, Cellular, and Evolutionary Biology **271A**(1), 225 (2003).

[40] J. Phillips, R. Johansson, and K. Johnson. *Representation of braille characters in human nerve fibres*. Experimental Brain Research **81**(3), 589 (1990).

[41] Srinivasan, M. A., Dandekar, and K. *An investigation of the mechanics of tactile sense using two-dimensional models of the primate fingertip*, vol. 118 (American Society of Mechanical Engineers, New York, NY, 1996).

[42] F. Vega-Bermudez and K. O. Johnson. *Sa1 and ra receptive fields, response variability, and population responses mapped with a probe array*. Journal of Neurophysiology **81**(6), 2701 (1999).

[43] J. Z. Wu, K. Krajnak, D. E. Welcome, and R. G. Dong. *Analysis of the dynamic strains in a fingertip exposed to vibrations: Correlation to the mechanical stimuli on mechanoreceptors*. Journal of Biomechanics **39**(13), 2445 (2006).

[44] W. Loewenstein and M. Mendelso. *Components of receptor adaptaton in a pacinian corpuscle*. Journal of Physiology **177**(3), 377 (1965).

[45] M. Knibestol. *Stimulus-response functions of rapidly adapting mechanoreceptors in the human glabrous skin area*. The Journal of Physiology **232**(3), 427 (1973).

[46] J. R. Phillips and K. O. Johnson. *Tactile spatial resolution. iii. a continuum mechanics model of skin predicting mechanoreceptor responses to bars, edges, and gratings*. J Neurophysiol **46**(6), 1204 (1981).

[47] D. De Rossi and E. P. Scilingo. *Skin-like sensor arrays*. In *Encyclopedia of Sensors*, pp. 535–556 (American Scientific Publishers, 2006).

[48] A. R. Moller. *Sensory Systems: anatomy and physiology* (Academic press, Dallas, Texas, 2003).

[49] A. B. Vallbo and R. S. Johansson. *Properties of cutaneous mechanoreceptors in the human hand related to touch sensation*. Human Neurobiology **3**(1), 3 (1984).

[50] S. A. Jones and S. J. Lederman. *Human Hand Function* (Oxford University Press, 2006).

[51] A. W. Goodwin and H. E. Wheat. *Physiological responses of sensory afferents in glabrous and hairy skin of humans and monkeys*. In I. B. Allan, K. Akimichi, M. S. Gordon, W. Gerald, D. A. Thomas, H. M. Richard, D. Peter, O. Donata, F. Stuart, K. B. Gary, M. C. Bushnell, H. K. Jon, and G. Esther, eds., *The Senses: A Comprehensive Reference*, pp. 39–54 (Academic Press, New York, 2008).

[52] R. D. Howe and M. R. Cutkosky. *Sensing skin acceleration for slip and texture perception*. In *IEEE International Conference on Robotics and Automation*, vol. 1, pp. 145–150 (1989).

[53] C. J. Cascio and K. Sathian. *Temporal cues contribute to tactile perception of roughness*. J. Neurosci. **21**(14), 5289 (2001).

[54] S. Lederman. *Tactile roughness of grooved surfaces: The touching process and effects of macro- and microsurface structure*. Perception and Psychophysics **16**(2), 385 (1974).

[55] D. G. Caldwell, N. Tsagarakis, and C. Giesler. *An integrated tactile/shear feedback array for stimulation of finger mechanoreceptor*. In *Robotics and Automation, 1999. Proceedings. 1999 IEEE International Conference on*, vol. 1, pp. 287–292 vol.1 (1999).

[56] D. Katz. *The World of Touch* (Lawrence Erlbaum Associates, 1989).

[57] M. Hollins and S. R. Risner. *Evidence for the duplex theory of tactile texture perception*. Perception and Psychophysics **62**(4), 695 (2000).

[58] T. Yoshioka, B. Gibb, A. K. Dorsch, S. S. Hsiao, and K. O. Johnson. *Neural coding mechanisms underlying perceived roughness of finely textured surfaces*. J. Neurosci. **21**(17), 6905 (2001).

[59] M. A. Srinivasan, J. M. Whitehouse, and R. H. LaMotte. *Tactile detection of slip: surface microgeometry and peripheral neural codes*. J Neurophysiol **63**(6), 1323 (1990).

[60] B. Hughes and G. Jansson. *Texture perception via active touch*. Human Movement Science **13**(3-4), 301 (1994).

[61] B. V. Jayawant. *Tactile sensing in robotics*. Journal of Physics E: Scientific Instruments **22**(9), 684 (1989).

[62] D. J. Beebe, A. S. Hsieh, D. D. Denton, and R. G. Radwin. *A silicon force sensor for robotics and medicine*. Sensors and Actuators a-Physical **50**(1-2), 55 (1995).

[63] D. De Rossi, G. Canepa, G. Magenes, F. Germagnoli, A. Caiti, and T. Parisini. *Skin-like tactile sensor arrays for contact stress field extraction*. Materials Science and Engineering: C **1**(1), 23 (1993).

[64] P. H. Chappell and J. A. Elliott. *Contact force sensor for artificial hands with a digital interface for a controller*. Measurement Science and Technology **14**(8), 1275 (2003).

[65] C. S. Smith. *Piezoresistance effect in germanium and silicon*. Physical Review **94**(1), 42 (1954).

[66] H. E. Elgamel. *Closed-form expressions for the relationships between stress, diaphragm deflection, and resistance change with pressure in silicon piezoresistive pressure sensors*. Sensors and Actuators A: Physical **50**(1-2), 17 (1995).

[67] A. Wisitsoraat, V. Patthanasetakul, T. Lomas, and A. Tuantranont. *Low cost thin film based piezoresistive mems tactile sensor*. Sensors and Actuators A: Physical **139**(1-2), 17 (2007).

[68] P. Dario, D. De Rossi, C. Domenici, and R. Francesconi. *Ferroelectric polymer tactile sensors with anthropomorphic features*. In *IEEE International Conference on Robotics and Automation*, vol. 1, pp. 332–340 (1984).

[69] D. G. Pirolo and E. S. Kolesar. *Piezoelectric polymer tactile sensor arrays for robotics*. In *Aerospace and Electronics Conference, 1989. NAECON 1989., Proceedings of the IEEE 1989 National*, pp. 1130–1135 vol.3 (1989).

[70] P. Dario, M. Bergamasco, A. Fiorillo, and R. Leonardo. *Geometrical optimization criteria for the design of tactile sensing patterns*. In *Robotics and Automation. Proceedings. 1986 IEEE International Conference on*, vol. 3, pp. 1268–1273 (1986).

[71] F. He, Q.-A. Huang, and M. Qin. *A silicon directly bonded capacitive absolute pressure sensor*. Sensors and Actuators A: Physical **135**(2), 507 (2007).

[72] D. Yamada, T. Maeno, and Y. Yamada. *Artificial finger skin having ridges and distributed tactile sensors used for grasp force control*. In T. Maeno, ed., *Intelligent Robots and Systems, 2001. Proceedings. 2001 IEEE/RSJ International Conference on*, vol. 2, pp. 686–691 vol.2 (2001).

[73] T. Maeno, T. Kawai, and K. Kobayashi. *Analysis and design of a tactile sensor detecting strain distribution inside an elastic finger*. In *IEEE/RSJ International Conference on Intelligent Robots and Systems*, vol. 3, pp. 1658–1663 (1998).

[74] Y. Mukaibo, H. Shirado, M. Konyo, and T. Maeno. *Development of a texture sensor emulating the tissue structure and perceptual mechanism of human fingers*. In *Robotics and Automation, 2005. ICRA 2005. Proceedings of the 2005 IEEE International Conference on*, pp. 2565–2570 (2005).

[75] K. Hosoda, Y. Tada, and M. Asada. *Anthropomorphic robotic soft fingertip with randomly distributed receptors*. Robotics and Autonomous Systems **54**(2), 104 (2006).

[76] N. Wettels, V. J. Santos, R. S. Johansson, and G. E. Loeb. *Biomimetic tactile sensor array*. Advanced Robotics **22**(8), 829 (2008).

[77] M. Gad-el Hak. *MEMS Introduction and Fundamentals* (Taylor and Francis Group, 2006).

[78] M. J. Madou. *Fundamentals of microfabrication* (CRC press, 1997).

[79] J. W. Gardner and V. K. Varadan. *Microsensors, MEMS and Smart Devices* (John Wiley and Sons, 2001).

[80] S. Beeby, g. Ensell, M. Kraft, and N. White. *MEMS Mechanical Sensors* (Artech House, Inc., 2004).

[81] S. M. Spearing. *Materials issues in microelectromechanical systems (mems)*. Acta Materialia **48**(1), 179 (2000).

[82] Y. P. Zhao, L. S. Wang, and T. X. Yu. *Mechanics of adhesion in mems - a review*. Journal of Adhesion Science and Technology **17**, 519 (2003).

[83] R. Maboudian, W. R. Ashurst, and C. Carraro. *Self-assembled monolayers as anti-stiction coatings for mems: characteristics and recent developments*. Sensors and Actuators A: Physical **82**(1-3), 219 (2000).

[84] L. L. Faulkner. *Microengineering, MEMS and Interfacing: A practical guide* (Taylor and Francis group, 2006).

[85] C. Kukjin and K. D. Wise. *A high-performance silicon tactile imager based on a capacitive cell*. Electron Devices, IEEE Transactions on **32**(7), 1196 (1985).

[86] K. Suzuki, K. Najafi, and K. D. Wise. *A 1024-element high-performance silicon tactile imager*. Electron Devices, IEEE Transactions on **37**(8), 1852 (1990).

[87] Z. Chu, P. M. Sarro, and S. Middelhoek. *Silicon three-axial tactile sensor*. Sensors and Actuators A: Physical **54**(1-3), 505 (1996).

[88] B. L. Gray, R. S. Fearing, R. Ieee, and S. O. C. Automat. *A surface micromachined microtactile sensor array*. In *1996 Ieee International Conference on Robotics and Automation, Proceedings, Vols 1-4*, Ieee International Conference on Robotics and Automation, pp. 1–6 (I E E E, New York, 1996).

[89] T. Mei, W. J. Li, Y. Ge, Y. Chen, L. Ni, and M. H. Chan. *An integrated mems three-dimensional tactile sensor with large force range*. Sensors and Actuators A: Physical **80**(2), 155 (2000).

[90] M. Leineweber, G. Pelz, M. Schmidt, H. Kappert, and G. Zimmer. *New tactile sensor chip with silicone rubber cover*. Sensors and Actuators A: Physical **84**(3), 236 (2000).

[91] Y. S. Lee and K. D. Wise. *A batch-fabricated silicon capacitive pressure transducer with low temperature sensitivity*. Electron Devices, IEEE Transactions on **29**(1), 42 (1982).

[92] E. Ruiz-Hitzky, M. Darder, P. Aranda, and K. Ariga. *Advances in biomimetic and nanostructured biohybrid materials*. Advanced Materials **22**(3), 323 (2010).

[93] V. G. Macefield. *Physiological characteristics of low-threshold mechanoreceptors in joints, muscle and skin in human subjects*. Clinical and Experimental Pharmacology and Physiology **32**(1-2), 135 (2005).

[94] C. M. Light and P. H. Chappell. *Development of a lightweight and adaptable multiple-axis hand prosthesis*. Medical Engineering and Physics **22**(10), 679 (2000).

[95] H. E. Wheat, L. M. Salo, and A. W. Goodwin. *Human ability to scale and discriminate forces typical of those occurring during grasp and manipulation*. Journal of Neuroscience **24**(13), 3394 (2004).

[96] W. H. Ko. *Solid-state capacitive pressure transducers*. Sensors and Actuators **10**(3-4), 303 (1986).

[97] J. C. Greenwood. *Silicon in mechanical sensors*. J. Phys. E: Sci. Instrum. **21**(12), 1114 (1988).

[98] F. Zhu and J. W. Spronck. *A capacitive tactile sensor for shear and normal force measurements*. Sensors and Actuators A: Physical **31**(1-3), 115 (1992).

[99] D. C. Catling. *High-sensitivity silicon capacitive sensors for measuring medium-vacuum gas pressures*. Sensors and Actuators A: Physical **64**(2), 157 (1998).

[100] O. Akar, T. Akin, and K. Najafi. *A wireless batch sealed absolute capacitive pressure sensor*. Sensors and Actuators A: Physical **95**, 29 (2001).

[101] M. A. Hopcroft, W. D. Nix, and T. W. Kenny. *What is the young's modulus of silicon?* Microelectromechanical Systems, Journal of **19**(2), 229 (2010).

[102] K. E. Petersen. *Silicon as a mechanical material*. Proceedings of the IEEE **70**(5), 420 (1982).

[103] J. A. Voorthuyzen and P. Bergveld. *The influence of tensile forces on the deflection of circular diaphragms in pressure sensors*. Sensors and Actuators **6**(3), 201 (1984).

[104] S. P. Timoshenko and S. Woinowsky-Krieger. *Theory of Plates and Shells (2nd Edition)* (McGraw-Hill, New York, 1959).

[105] W. H. Ko and Q. Wang. *Touch mode capacitive pressure sensors*. Sensors and Actuators A: Physical **75**(3), 242 (1999).

[106] M. Bao. *Analysis and design principles of MEMS devices* (Elsevier, 2005), 1 ed.

[107] I. Etchart, H. Chen, P. Dryden, J. Jundt, C. Harrison, K. Hsu, F. Marty, and B. Mercier. *Mems sensors for density-viscosity sensing in a low-flow microfluidic environment*. Sensors and Actuators A: Physical **141**(2), 266 (2008).

[108] J. Lucas, S. Hole, and C. Batis. *Analytical capacitive sensor sensitivity distribution and applications*. Measurement Science and Technology **17**(9), 2467 (2006).

[109] R. Puers and D. Lapadatu. *Electrostatic forces and their effects on capacitive mechanical sensors*. Sensors and Actuators A: Physical **56**(3), 203 (1996).

[110] W. Eaton, F. Bitsie, D. Plummer, and J. Smith. *A New Analytical Solution for Diaphragm Deflection and its Application to a Surface-Micromachined Pressure Sensor* (1999).

[111] T.-R. Hsu. *MEMS and Microsystems: Design, Manufacture and Nanoscale Engineering* (John Wiley and Sons, 2008), 2 ed.

[112] G. J. Gerling and G. W. Thomas. *The effect of fingertip microstructures on tactile edge perception*. World Haptics Conference: First Joint Eurohaptics Conference and Symposium on Haptic Interfaces for Virutual Environment and Teleoperator Systems, Proceedings (Ieee Computer Soc, Los Alamitos, 2005).

[113] J. Hu, D. Xin, and R. Wang. *Dependence of tactile sensation on deformations within soft tissues of fingertip*. World Journal of Modelling and Simulation **3**(1), 73 (2007).

[114] R. Simonton. *Special report soi wafer technology for cmos ics* (2002).

[115] A. J. Auberton-Herve. *Soi: materials to systems*. In *Electron Devices Meeting, 1996. IEDM '96., International*, pp. 3–10 (1996).

[116] C. Burrer, J. Esteve, and E. Lora-Tamayo. *Resonant silicon accelerometers in bulk micromachining technology-an approach*. Microelectromechanical Systems, Journal of **5**(2), 122 (1996).

[117] A. Merlos, J. Santander, M. D. Alvarez, and F. Campabadal. *Optimized technology for the fabrication of piezoresistive pressure sensors*. Journal of Micromechanics and Microengineering **10**(2), 204 (2000).

[118] A. Benitez, J. Esteve, and J. Bausells. *Bulk silicon microelectromechanical devices fabricated from commercial bonded and etched-back silicon-on-insulator substrates*. Sensors and Actuators a-Physical **50**(1-2), 99 (1995).

[119] K. Suzuki and B. W. Smith. *Microlithography: Science and Technology* (CRC press, 2007), 2 ed.

[120] S. Franssila. *Introduction to Microfabrication* (Wiley-Blackwell, 2004).

[121] G. T. A. Kovacs, N. I. Maluf, and K. E. Petersen. *Bulk micromachining of silicon*. Proceedings of the IEEE **86**(8), 1536 (1998).

[122] G. T. A. Kovacs. *Micromachined transducers sourcebook* (McGraw-Hill, 1998).

[123] A. A. AyÃŻn and L. Massachusetts Institute of Technology. Microsystems Technology. *Etching characteristics and profile control in a time multiplexed inductively coupled plasma etcher* (Microsystems Technology Laboratories, Massachusetts Institute of Technology, Cambridge, Mass., 1998).

[124] D. A. Hook, J. A. Olhausen, J. Krim, and M. T. Dugger. *Evaluation of oxygen plasma and uv ozone methods for cleaning of occluded areas in mems devices*. Microelectromechanical Systems, Journal of **19**(6), 1292 (2010).

[125] J. Buhler, F. P. Steiner, and H. Baltes. *Silicon dioxide sacrificial layer etching in surface micromachining*. Journal of Micromechanics and Microengineering **7**(1), R1 (1997).

[126] J. M. Bustillo, R. T. Howe, and R. S. Muller. *Surface micromachining for microelectromechanical systems*. Proceedings of the IEEE **86**(8), 1552 (1998).

[127] N. Tas, T. Sonnenberg, H. Jansen, R. Legtenberg, and M. Elwenspoek. *Stiction in surface micromachining*. Journal of Micromechanics and Microengineering **6**(4), 385 (1996).

[128] M. A. Rosa, S. Dimitrijev, and H. B. Harrison. *Avoidance of stiction in the release of highly boron doped micro-actuators fabricated using besoi substrates*. Microelectronics Reliability **39**(1), 139 (1999).

[129] P. Jianbiao, R. M. Pafchek, F. F. Judd, and J. B. Baxter. *Effect of chromium-gold and titanium-titanium nitride-platinum-gold metallization on wire/ribbon bondability*. Advanced Packaging, IEEE Transactions on **29**(4), 707 (2006).

[130] R. Puers. *Capacitive sensors: When and how to use them*. Sensors and Actuators A: Physical **37-38**, 93 (1993).

[131] H. Yu, G. Zhou, and F. S. Chau. *Yield improvement for anodic bonding with suspending structure*. Sensors and Actuators A: Physical **143**(2), 462 (2008).

[132] I. Sadaba, C. H. J. Fox, and S. McWilliam. *An investigation of residual stress effects due to the anodic bonding of glass and silicon in mems fabrication*. In P. S. Keogh, ed., *Modern Practice in Stress and Vibration Analysis VI, Proceedings*, vol. 5-6 of *Applied Mechanics and Materials*, pp. 501–508 (Trans Tech Publications Ltd, Stafa-Zurich, 2006).

[133] M. Carrozza, G. Cappiello, S. Micera, B. Edin, L. Beccai, and C. Cipriani. *Design of a cybernetic hand for perception and action*. Biological Cybernetics **95**(6), 629 (2006).

[134] M. Cutkosky, J. Jourdain, and P. Wright. *Skin materials for robotic fingers*. In *Robotics and Automation. Proceedings. 1987 IEEE International Conference on*, vol. 4, pp. 1649–1654 (1987).

[135] R. Gulati and M. A. Srinivasan. *Determination of mechanical properties of the human fingerpad, in vivo, using a tactile stimulator*. Ph.D. thesis, Massachusetts Institute of Technology (1997).

[136] S. MacNeil. *Progress and opportunities for tissue-engineered skin*. Nature **445**(7130), 874 (2007).

[137] F. Shao, T. H. C. Childs, and B. Henson. *Developing an artificial fingertip with human friction properties*. Tribology International **42**(11-12), 1575 (2009).

[138] N. Pavselj, M. Mitar, F. Hart, and D. Miklavcic. *Characterization of the mechanical behavior of human skin by means of impedance spectroscopy*. Journal of Physics: Conference series **224**(1) (2010).

[139] J. F. M. Manschot and A. J. M. Brakkee. *The measurement and modelling of the mechanical properties of human skin in vivo–ii. the model*. Journal of Biomechanics **19**(7), 517 (1986).

[140] M. A. Meyers, P.-Y. Chen, A. Y.-M. Lin, and Y. Seki. *Biological materials: Structure and mechanical properties*. Progress in Materials Science **53**(1), 1 (2008).

[141] F. M. Hendriks. *Mechanical behaviour of human epidermal and dermal layers in vivo*. Ph.D. thesis, Technische Universiteit Eindhoven (2005).

[142] S. MacNeil. *Biomaterials for tissue engineering of skin*. Materials Today **11**(5), 26 (2008).

[143] N. Hunt. *An alginate hydrogel matrix for the localised delivery of a fibroblast/ keratinocyte co-culture to expedite wound healing*. Ph.D. thesis, University of Birmigham (2010).

[144] N. Cauna. *Nature and functions of the papillary ridges of the digital skin*. Anatomical record **119**(4), 449 (1954).

[145] J. Scheibert, S. Leurent, A. Prevost, and G. Debregeas. *The role of fingerprints in the coding of tactile information probed with a biomimetic sensor*. Science **323**(5920), 1503 (2009).

[146] T. C. Pataky, M. L. Latash, and V. M. Zatsiorsky. *Viscoelastic response of the finger pad to incremental tangential displacements*. Journal of Biomechanics **38**(7), 1441 (2005).

[147] E. R. Serina, C. D. Mote, and D. Rempel. *Force response of the fingertip pulp to repeated compression–effects of loading rate, loading angle and anthropometry*. Journal of Biomechanics **30**(10), 1035 (1997).

[148] F. H. Silver, J. W. Freeman, and D. DeVore. *Viscoelastic properties of human skin and processed dermis*. Skin Research and Technology **7**(1), 18 (2001).

[149] R. V. Shevchenko, S. L. James, and S. E. James. *A review of tissue-engineered skin bioconstructs available for skin reconstruction*. Journal of The Royal Society Interface **7**(43), 229 (2010).

[150] F. M. Hendriks, D. Brokken, J. T. W. M. Van Eemeren, C. W. J. Oomens, F. P. T. Baaijens, and J. B. A. M. Horsten. *A numerical-experimental method to characterize the non-linear mechanical behaviour of human skin*. Skin Research and Technology **9**(3), 274 (2003).

[151] Y. P. Zheng and A. F. T. Mak. *Extraction of effective young's modulus of skin and subcutaneous tissues from manual indentation data*. In *Engineering in Medicine and Biology Society, 1997. Proceedings of the 19th Annual International Conference of the IEEE*, vol. 5, pp. 2246–2249 vol.5 (1997).

[152] K. Dandekar, B. I. Raju, and M. A. Srinivasan. *3-d finite-element models of human and monkey fingertips to investigate the mechanics of tactile sense*. Journal of Biomechanical Engineering **125**(5), 682 (2003).

[153] F. P. Schmook, J. G. Meingassner, and A. Billich. *Comparison of human skin or epidermis models with human and animal skin in in-vitro percutaneous absorption*. International Journal of Pharmaceutics **215**(1-2), 51 (2001).

[154] A. Sardo, P. Tiezzi, and G. Vassura. *A methodological approach to design of soft fingertips for humanoid robot hands*. In *Humanoid Robots, 2006 6th IEEE-RAS International Conference on*, pp. 370–375 (2006).

[155] S. Derler, U. Schrade, and L. C. Gerhardt. *Tribology of human skin and mechanical skin equivalents in contact with textiles*. Wear **263**(7-12), 1112 (2007).

[156] F. Campabadal, J. L. Carreras, and E. Cabruja. *Flip-chip packaging of piezoresistive pressure sensors*. Sensors and Actuators A: Physical **132**(1), 415 (2006).

[157] H. Shirado, Y. Nonomura, and T. Maeno. *Realization of human skin-like texture by emulating surface shape pattern and elastic structure*. In *Haptic Interfaces for Virtual Environment and Teleoperator Systems, 2006 14th Symposium on*, pp. 295–296 (2006).

[158] A. Bratov, J. Munoz, C. Dominguez, and J. BartroliÂt'. *Photocurable polymers applied as encapsulating materials for isfet production*. Sensors and Actuators B: Chemical **25**(1-3), 823 (1995).

[159] J. J. Cabibihan, M. C. Carrozza, P. Dario, S. Pattofatto, M. Jomaa, and A. Benallal. *The uncanny valley and the search for human skin-like materials for a prosthetic fingertip*. In *Humanoid Robots, 2006 6th IEEE-RAS International Conference on*, pp. 474–477 (2006).

[160] A. Mahomed. *Properties of elastomers for small joint replacements*. Ph.D. thesis, University of Birmingham (2008).

[161] F. Schneider, J. Draheim, R. Kamberger, and U. Wallrabe. *Process and material properties of polydimethylsiloxane (pdms) for optical mems*. Sensors and Actuators A: Physical **151**(2), 95 (2009).

[162] M. I. Tiwana, A. Shashank, S. J. Redmond, and N. H. Lovell. *Characterization of a capacitive tactile shear sensor for application in robotic and upper limb prostheses*. Sensors and Actuators A: Physical **165**(2), 164 (2011).

[163] K. Noda, K. Hoshino, K. Matsumoto, and I. Shimoyama. *A shear stress sensor for tactile sensing with the piezoresistive cantilever standing in elastic material*. Sensors and Actuators A: Physical **127**(2), 295 (2006).

[164] A. Mata, A. Fleischman, and S. Roy. *Characterization of polydimethylsiloxane (pdms) properties for biomedical micro/nanosystems*. Biomedical Microdevices **7**(4), 281 (2005).

[165] F. Schneider, T. Fellner, J. Wilde, and U. Wallrabe. *Mechanical properties of silicones for mems*. Journal of Micromechanics and Microengineering **18**(6) (2008).

[166] R. A. Normann. *Visual neuroprosthetics-functional vision for the blind*. Engineering in Medicine and Biology Magazine, IEEE **14**(1), 77 (1995).

[167] T. Yagi. *Biohybrid visual prosthesis for restoring blindness*. International Journal of Applied Biomedical Engineering **2**(1), 1 (2009).

[168] H. B. Muhammad, N. C. Hunt, R. M. Shelton, L. M. Grover, M. C. L. Ward, C. M. Oddo, C. T. Recchiuto, and L. Beccai. *Incorporation of novel mems tactile sensors into tissue engineered skin*. In *Bioinformatics and Biomedical Engineering (iCBBE), 2010 4th International Conference on*, pp. 1–4 (2010).

[169] T. Dvir, B. P. Timko, D. S. Kohane, and R. Langer. *Nanotechnological strategies for engineering complex tissues*. Nat Nano **6**(1), 13 (2011).

[170] A. L. Williams, G. J. Gerling, S. A. Wellnitz, S. M. Bourdon, and E. A. Lumpkin. *Skin relaxation predicts neural firing rate adaptation in sai touch receptors*. In *Engineering in Medicine and Biology Society (EMBC), 2010 Annual International Conference of the IEEE*, pp. 6678–6681 (2010).

[171] M. Shimojo. *Mechanical filtering effect of elastic cover for tactile sensor*. Robotics and Automation, IEEE Transactions on **13**(1), 128 (1997).

[172] S. J. Lederman. *The perception of texture by touch*. Tactual perception: A sourcebook (England: Cambridge University Press, Cambridge, 1982).

[173] M. Lawrence, R. Kitada, R. Klatzky, and S. Lederman. *Haptic roughness perception of linear gratings via bare finger or rigid probe*. Perception **36**(4), 547 (2007).

[174] S. Lederman. *The perception of surface roughness by active and passive touch*. Bulletin of the Psychonomic Society **18**(5), 253 (1981).

[175] J. W. Morley, A. W. Goodwin, and I. Darian-Smith. *Tactile discrimination of gratings*. Experimental Brain Research **49**(2), 291 (1983).

[176] R. J. Sinclair and H. Burton. *Tactile discrimination of gratings: Psychophysical and neural correlates in human and monkey*. Somatosensory and Motor Research **8**(3), 241 (1991).

[177] H. B. Muhammad, C. M. Oddo, L. Beccai, C. Recchiuto, C. J. Anthony, M. J. Adams, M. C. Carrozza, D. W. L. Hukins, and M. C. L. Ward. *Development of a bioinspired mems based capacitive tactile sensor for a robotic finger*. Sensors and Actuators A: Physical **165**(2), 221 (2011).

[178] H. B. Muhammad, C. Recchiuto, C. M. Oddo, L. Beccai, C. J. Anthony, M. J. Adams, M. C. Carrozza, and M. C. L. Ward. *A capacitive tactile sensor array for surface texture discrimination*. Microelectronic Engineering **88**(8), 1811 (2011).

[179] J. F. E.R. Weppelmann and M. Swain. *Observation, analysis, and simulation of the hysteresis of silicon using ultra-micro-indentation with spherical indenters*. Journal of Materials Research **8**, 830 (1993).

[180] Y. C. Lu and D. M. Shinozaki. *Effects of substrate constraint on micro-indentation testing of polymer coatings*. Materials Science and Engineering A **396**(1-2), 77 (2005).

[181] S. Upcraft. *The rapid prototyping technologies*. Assembly Automation **23**(4), 318 (2003).

[182] A. P. Sripati, S. J. Bensmaia, and K. O. Johnson. *A continuum mechanical model of mechanoreceptive afferent responses to indented spatial patterns*. J Neurophysiol **95**(6), 3852 (2006).

Appendix A: Circuit Layout of Signal Acquisition Electronics

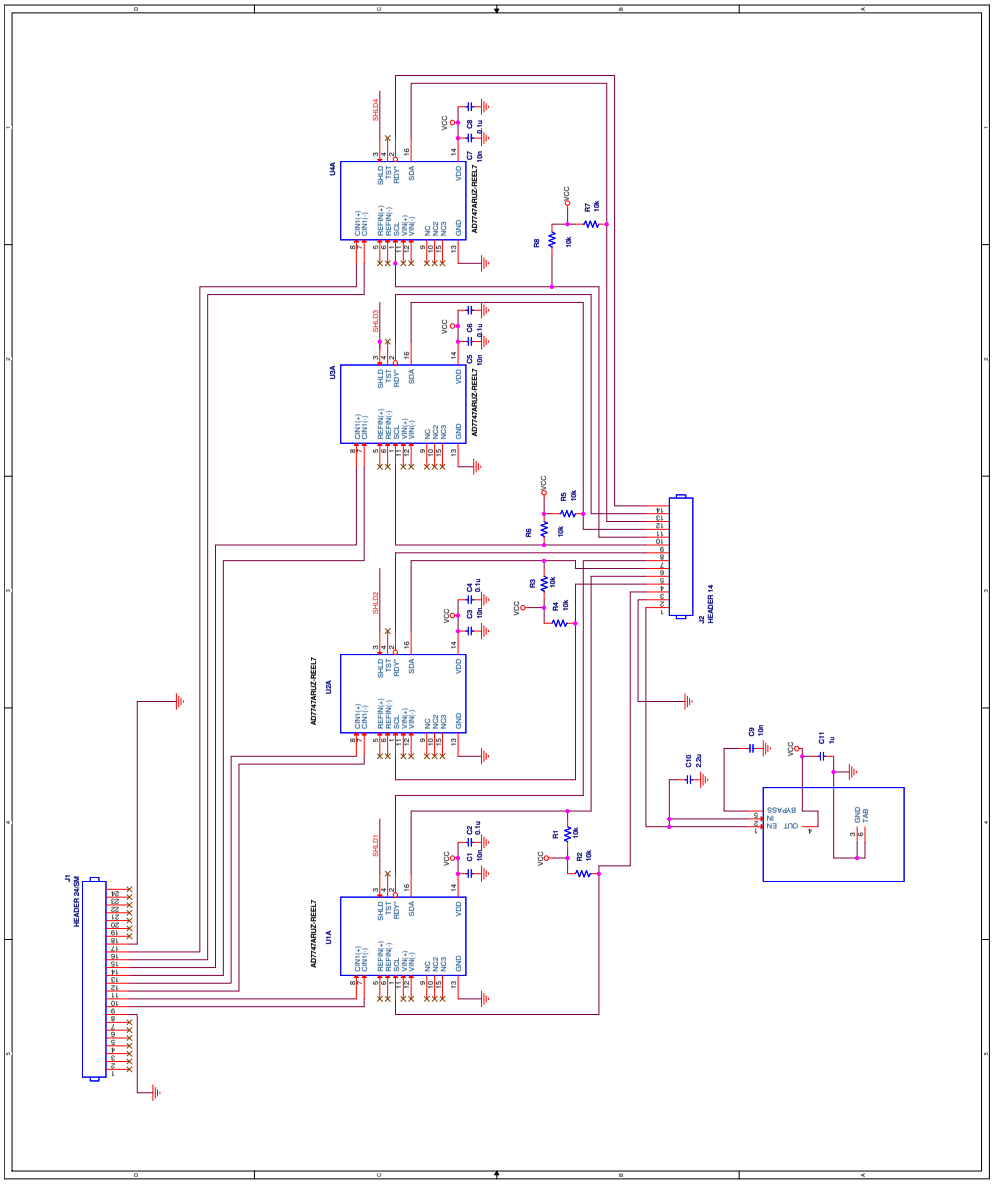
U4A
U3A
U2A
U1A
AD7747ARUZ-REEL7
J1
HEADER 24/2M
J2
HEADER 14
VCC
R1
10k
R2
10k
R3
10k
R4
10k
R5
10k
R6
10k
R7
10k
R8
10k
C1
10n
0.1u
C2
10n
0.1u
C3
10n
0.1u
C4
10n
0.1u
C5
10n
0.1u
C6
10n
0.1u
C7
10n
0.1u
C8
10n
0.1u
C9
10n
C10
2.2u
C11
1u
BYPASS
OUT
GND
TAB

Appendix B: Spatial mapping of a sensor packaged with Dragon Skin

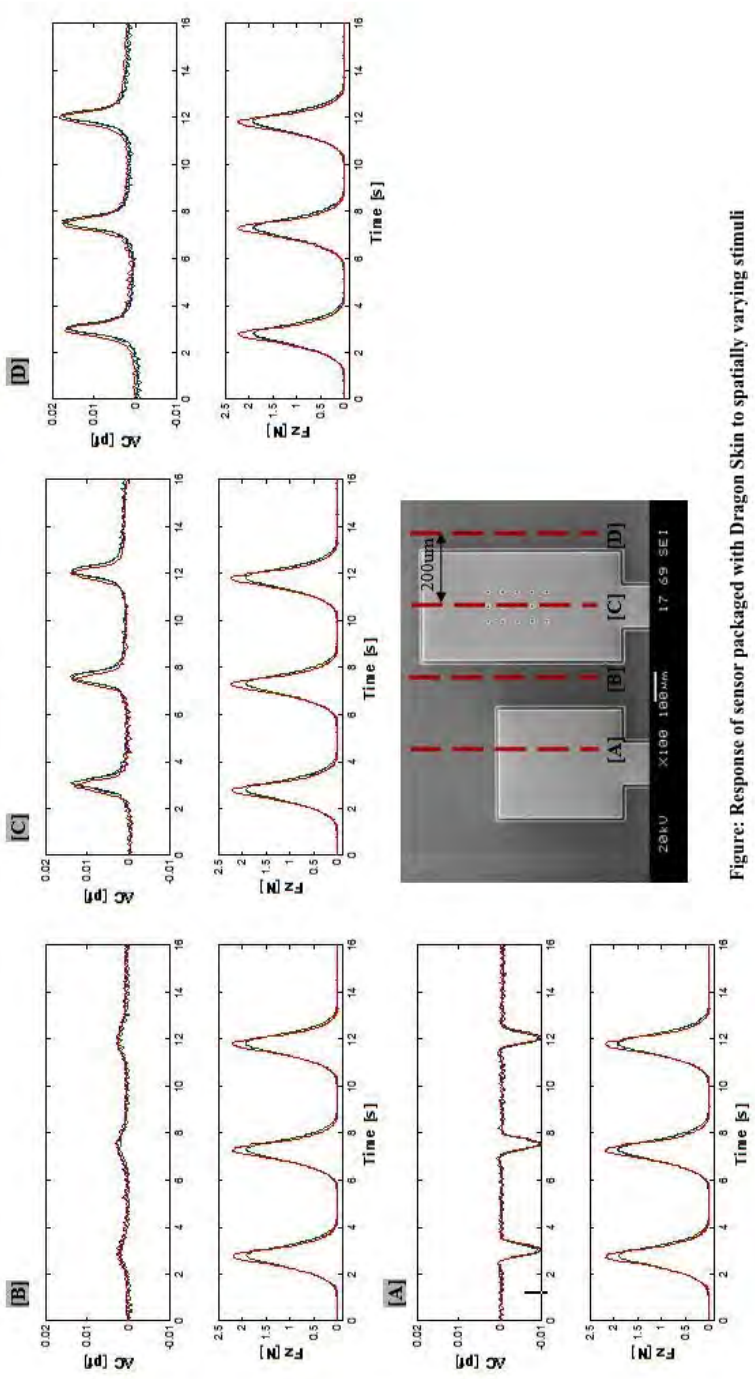

Figure: Response of sensor packaged with Dragon Skin to spatially varying stimuli

Appendix C: Response of sensors to fine and coarse gratings

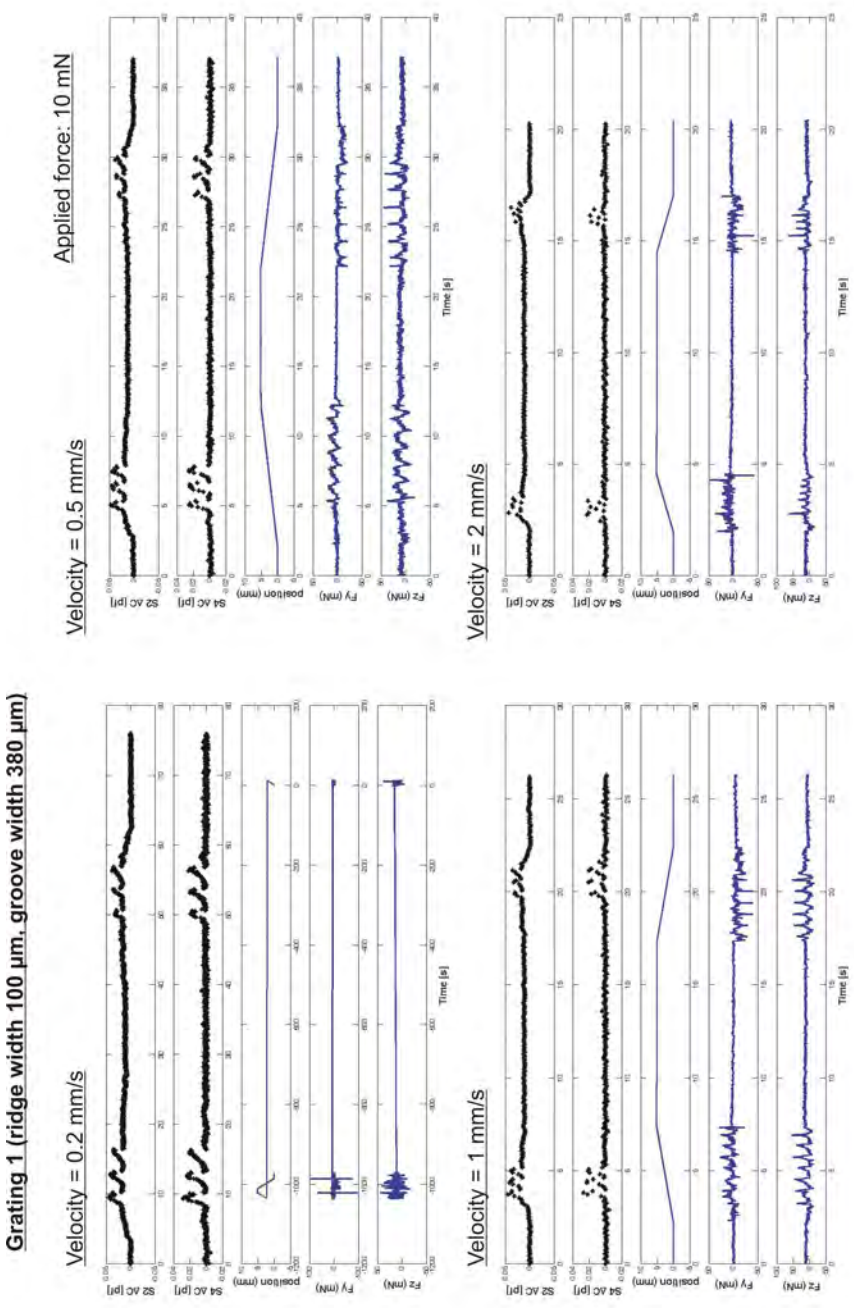
Grating 1 (ridge width 100 µm, groove width 380 µm)
Velocity = 0.2 mm/s
Velocity = 0.5 mm/s
Velocity = 1 mm/s
Velocity = 2 mm/s
Applied force: 10 mN
S2 AC [pf]
S4 AC [pf]
position (mm)
Fy (mN)
Fz (mN)
Time [s]

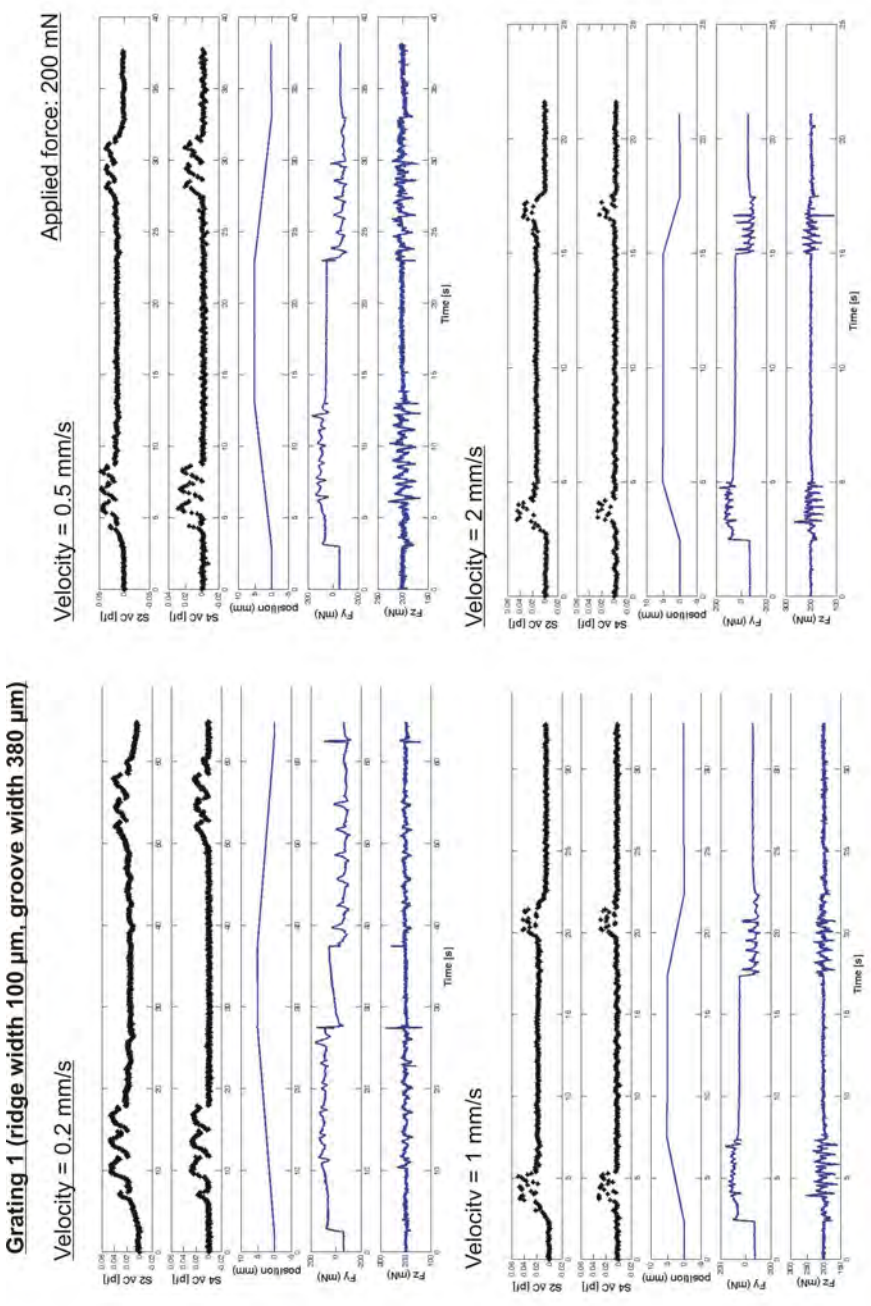
Grating 1 (ridge width 100 µm, groove width 380 µm)
Velocity = 0.2 mm/s
Velocity = 0.5 mm/s
Velocitv = 1 mm/s
Velocity = 2 mm/s
Applied force: 200 mN
S2 ΔC [pf]
S4 ΔC [pf]
position (mm)
Fy (mN)
Fz (mN)
Time [s]

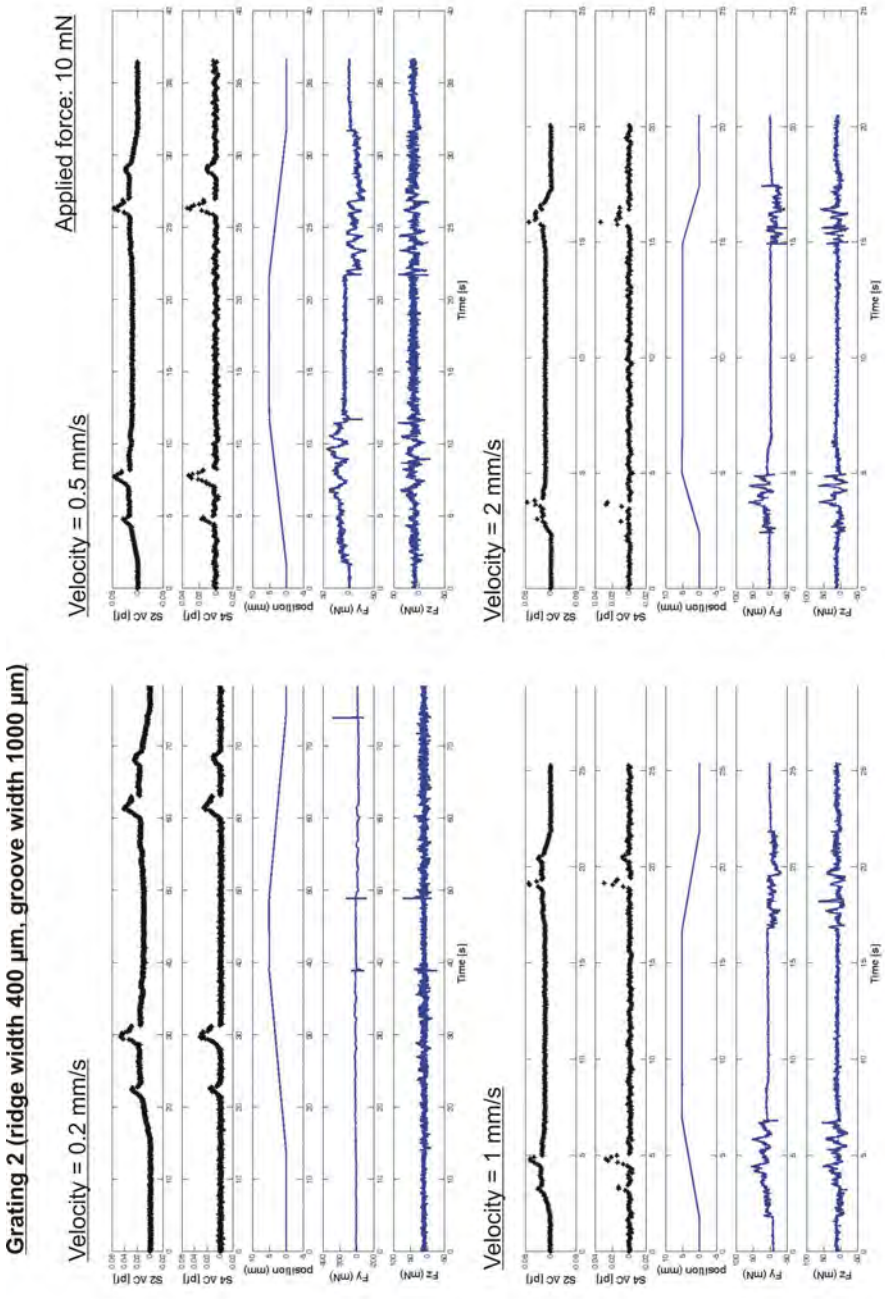
Grating 2 (ridge width 400 µm, groove width 1000 µm)
Velocity = 0.2 mm/s
Velocity = 0.5 mm/s
Velocity = 1 mm/s
Velocity = 2 mm/s
Applied force: 10 mN
S2 AC [pf]
S4 AC [pf]
position (mm)
Fy (mN)
Fz (mN)
Time [s]

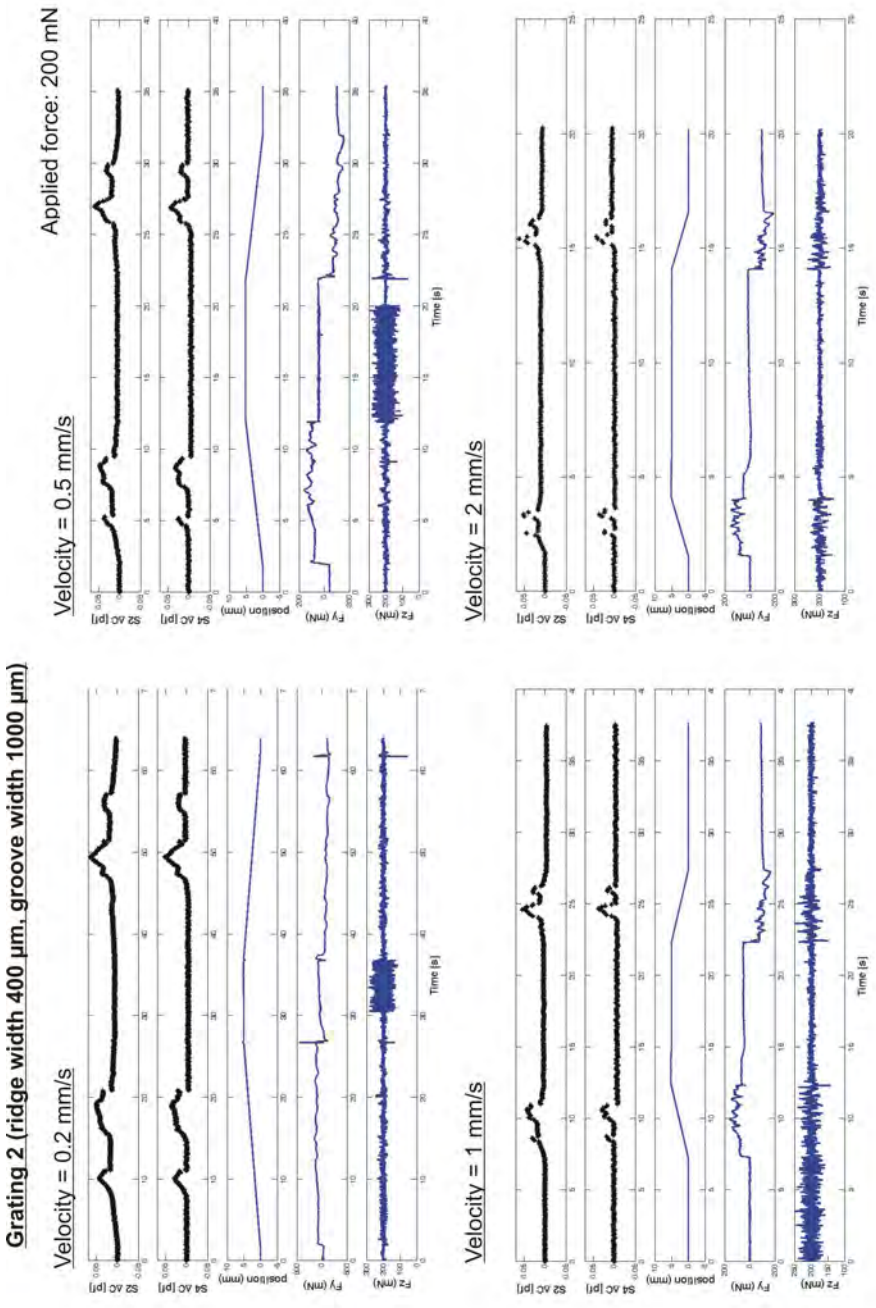
Grating 2 (ridge width 400 µm, groove width 1000 µm)
Applied force: 200 mN
Velocity = 0.2 mm/s
Velocity = 0.5 mm/s
Velocity = 1 mm/s
Velocity = 2 mm/s
S2 AC [pF]
S4 AC [pF]
position (mm)
Fy (mN)
Fz (mN)
Time [s]